AN ABSTRACT OF THE THESIS OF

Kyle A. Krawl for the degree of Master of Science in Ocean, Earth and Atmospheric Sciences presented on September 8, 2014.

Title: A Petrogenetic Model for the Caribbean Large Igneous Province

Abstract approved:

_____

Robert A. Duncan Adam J. R. Kent

The Caribbean Plateau is an oceanic large igneous province (CLIP). A widely accepted model for LIP petrogenesis proposes that these large bodies of igneous rock are formed by decompression melting associated with upwelling mantle plume heads during the initiation of hotspot activity. According to this classical model, petrogenesis occurs over a relatively short timeframe (i.e. a few million years). Recently published $^{40}Ar/^{39}Ar$ ages for the CLIP, however, suggest a much larger age range (~30 m.y.) despite relatively limited geochemical variation. This raises questions about the applicability of the "mantle plume impact" model to the Caribbean Plateau. Although previous research has examined the processes and mantle sources involved in the construction of the CLIP, there is currently not a petrogenetic model that attempts to reconcile the geochemistry of the CLIP with this extended age range.

The research presented in this thesis utilizes major element, trace element, and isotopic chemistry of intrusive and extrusive basaltic samples from three localities—

the Curaçao Lava Formation (CLF), Dumisseau Formation (DF) and Beata Ridge (BR)—in order to develop a petrogenetic model for the CLIP capable of accounting for the relatively limited variation in geochemistry over ~30 m.y. of volcanic activity. This model integrates the results of MELTS and rare earth element (REE) modeling to provide constraints on the nature of the parental magmas, melting processes, and mantle source(s) of the CLIP.

The results of the MELTS modeling demonstrate that nearly the full range of major element compositions observed in the CLIP samples can be generated by fractional crystallization of magmas with similar major element compositions with a range of water contents (0-1 wt%), and crystallizing over a range of pressures (1-2.5 kbar). This suggests a magma storage system with multiple shallow crustal magma chambers in which efficient mixing resulted in a relatively restricted range of compositions.

Despite the large age range observed for the CLIP lavas, the geochemistry of the samples is not inconsistent with a plume-related origin, and isotopic compositions show significant overlap with those of the Galápagos plume. Age-corrected ε_{Nd} for the CLIP samples ranges from ~5.1 to 9.4, suggesting a mantle source that has components of depleted (MORB) and plume mantle. Indeed, batch melting and fractional crystallization models using REEs suggest that the geochemistry of the CLIP samples is consistent with variable degrees of melting of a hybrid of enriched and depleted mantle sources. The difference in degree of melting indicated by the model for the CLF and BR (~15-30%) relative to the DF (~5-10%) is consistent with a model in which the CLF and BR lie near the plume axis, while the DF is situated

near the plume margin. Paradoxically, although the Nd isotopic compositions of the CLIP samples suggest a variably depleted source, the results of the batch melting model suggest contributions from source material with greater trace element enrichment than primitive mantle. The combination of a variably depleted isotopic signature with depleted to enriched trace element compositions suggests that the enriched material was generated by the relatively recent metasomatism of a long-term depleted mantle source.

The results of these models are consistent with a formation mechanism for the CLIP in which melting is mediated by the interaction between plume head material and asthenospheric mantle flow associated with nearby subduction zones. Changes in the mantle flow regime due to variations in the orientation (e.g. polarity reversals, slab rollback) of nearby subduction zones would allow for localized upwelling beneath the initially formed CLIP (~94 Ma), allowing for ~30 million years of intermittent magmatism through the repeated tapping of this mantle source. The petrogenetic model for the CLIP presented here demonstrates that the classical paradigm for LIP petrogenesis is not universally applicable, and suggests that the formation of LIPs may be significantly influenced by lithosphere-asthenosphere dynamics (such as subduction-driven mantle flow) in addition to plume-driven melting.

A Petrogenetic Model for the Caribbean Large Igneous Province

by
Kyle A. Krawl

A THESIS

submitted to

Oregon State University

in partial fulfillment of
the requirements for the
degree of

Master of Science

Presented September 8, 2014
Commencement June 2015

Master of Science thesis of Kyle A. Krawl presented on September 8, 2014.

APPROVED:

Co-Major Professor, representing Ocean, Earth, and Atmospheric Sciences

Co-Major Professor, representing Ocean, Earth, and Atmospheric Sciences

Dean of the College of Earth, Ocean and Atmospheric Sciences

Dean of the Graduate School

I understand that my thesis will become part of the permanent collection of Oregon State University libraries. My signature below authorizes release of my thesis to any reader upon request.

Kyle A. Krawl, Author

ACKNOWLEDGEMENTS

The work that led to this thesis began when I was a sophomore at OSU, and over the past four years many individuals have aided me in getting to this point. Bob Duncan has been an excellent mentor. His guidance has helped me through both an undergraduate and a Master's thesis, and I'm grateful for the knowledge he's shared. Adam Kent has advised me for about as long. He's taught me a great deal about geochemistry, and his suggestions have saved me from several (mostly modeling-induced) headaches. I've learned quite a bit from Dave Graham as well, and I'm grateful to him for serving on my committee.

I've also received a great deal of support from fellow students. Matt Loewen in particular deserves high praise. It was Matt who first showed me how to examine thin sections, model magma evolution with MELTS, and tackle the various obstacles that emerge in research and writing. Jenny DiGiulio and Jacob Petersen-Perlman also deserve thanks. They've been great office-mates, and have helped me preserve my sanity throughout the process of preparing this thesis. I am very grateful to Julie Klath as well. Her perseverance and independent spirit have been an inspiration to me over the last four years, and I'm fortunate to know her.

The analytical work in this thesis would not have been possible without the helpful instruction of several people. Frank Tepley and Dale Burns provided invaluable assistance with electron microprobe analysis. Jesse Muratli and Brian Haley gave me a crash course in the sample preparation and analysis of isotopic compositions in whole rock samples. Rick Conrey at Washington State University provided me with valuable assistance preparing samples for X-ray fluorescence

spectroscopy and inductively-coupled plasma mass spectrometry. Samples from the Dumisseau Formation, Haiti were provided by Prof Florentin Maurrasse, Florida International University.

The foundation of this thesis was laid when I was still an OSU undergraduate, and during that time I was fortunate to learn from several excellent instructors. A number of CEOAS faculty have helped guide me through my education as a scientist, and I'm thankful to each of them. I owe a great deal of gratitude to Kaplan Yalcin in particular. It was his teaching that spurred my interest in geology started me down the path of earth science.

Lastly, but most importantly, I'd like to thank my parents. Their hard work has inspired me throughout my education. I'm grateful for their love and support. They've played a crucial role in helping me get to where I am today.

TABLE OF CONTENTS

Page

LIST OF FIGURES

LIST OF TABLES

LIST OF APPENDIX TABLES

1 Introduction

Large igneous provinces (LIPs) are laterally extensive (~1000 km) bodies of primarily mafic intrusive and extrusive igneous rock produced by processes other than typical seafloor spreading. They represent a significant component of mafic crustal material, second only to mid-ocean ridge basalt produced at spreading centers. LIPs occur as both continental flood basalts and oceanic plateaus, and may also manifest as submarine ridges or ocean basin flood basalts (Coffin and Edholm, 1994). In contrast to the relatively stable and continuous production of crust at mid-ocean ridges, LIPs are more episodic in nature (Larson, 1991). LIPs thus have the potential to provide constraints on mantle processes that are distinct from those associated with typical shallow upper mantle production of oceanic crust at spreading centers.

A prevailing model attributes the petrogenesis of LIPs to melting triggered by upwelling associated with mantle plumes during the initial stages of hotspot activity (Morgan, 1981; Richards *et al*., 1989; Duncan and Richards, 1991). According to this model, LIPs typically form within a few million years (Morgan, 1981; Richards *et al*., 1989; Duncan and Richards, 1991). Although this model appears to adequately describe the petrogenesis of many flood basalts and oceanic plateaus, there are also a number of LIPs that require more complex histories. The Kerguelen Plateau, for example, shows evidence of ~130 m.y. of plume-related magmatism (e.g. Duncan, 1978; Mahoney *et al*., 1983). Similarly, ages for the Ontong Java Plateau provide evidence of distinct pulses of volcanism at 120-122 Ma and 88-90 Ma (Bercovici and Mahoney, 1994). Additionally, the petrogenesis of several LIPs has been attributed to mechanisms other than mantle plumes. For example, Ingle and Coffin (2004) proposed that the formation of the Ontong

Java Plateau may have resulted from melting associated with a bolide impact on the basis of geochemical evidence (e.g. low volatile contents and platinum group element enrichment in basalts). Although these alternative models remain the subject of debate, it is clear that the classical model of LIP petrogenesis—formation in a few million years due to rapid, plume-initiated melting—cannot be fully applied to all LIPs. Continued research is thus needed in order to constrain the range of possible melting conditions and petrogenetic mechanisms for LIPs and to determine the extent to which this classical model can be applied.

1.1 The Caribbean Plateau

The Caribbean Plateau is an oceanic LIP that serves as a useful case study of the limitations of the classical model of LIP petrogenesis. Previous work suggests that the Caribbean Large Igneous Province (CLIP) formed in the eastern Pacific as a result of melting associated with the arrival of a mantle plume at the base of the lithosphere, in broad agreement with the classical model for LIP petrogenesis described above (e.g. Duncan and Hargraves, 1984; Duncan and Richards, 1991). Multiple plate tectonic models suggest that the CLIP began moving eastward into its present position during the late Cretaceous (Burke *et al*., 1984; Duncan and Hargraves, 1984; Pindell and Barrett, 1990; Kerr *et al*., 1999). Duncan and Hargraves (1984) report that this eastward movement resulted in the collision of the CLIP with the Greater Antilles Arc between South and Central America between 80 and 90 Ma. According to these authors, this resulted in the uplift and accretion of thick sections of Caribbean Plateau crust along the margins of northwestern South America. Rather than being subducted, the CLIP was

sufficiently thick and buoyant to clog the trench. This resulted in a polarity flip of the subduction zone associated with the Greater Antilles Arc (from northeast-dipping to southwest-dipping), accompanied by subduction of oceanic crust beneath the eastern margin of the Caribbean Plateau. By about 60 Ma, the Central American Arc had formed to the southwest of the CLIP, accompanied by the subduction of the Farallon plate beneath the Caribbean Plateau (Duncan and Hargraves, 1984).

The close association of subduction zones with the Caribbean Plateau is supported by field observations and geochemical evidence. Thompson *et al*. (2004) identified lavas at Bonaire with isotopic signatures of island arc magmatism (e.g. negative Nb and Ta anomalies, ε_{Hf} of +12 to +14, ε_{Nd} of +6.5 to +8). ^{40}Ar-^{39}Ar ages for these rocks suggest that subduction was occurring by ~92-100 Ma. Escuder Viruete *et al*. (2007) identified adakites, magnesian andesites, and other island arc compositions among lavas in a Late Cretaceous sequence in Hispaniola. U-Pb and ^{40}Ar-^{39}Ar ages for this sequence suggest that subduction initiated before ~90 Ma. White *et al*. (1998) noted that a sequence of CLIP lavas in Aruba are intruded by a tonalitic batholith (considered a product of arc magmatism) with an age of ~82-85 Ma. Field observations (e.g. foliation in CLIP basalts) suggest that the emplacement of this batholith occurred while the CLIP sequence was experiencing significant deformation, consistent with collision with a subduction zone. These observations provide evidence for the interaction between the CLIP and a subduction zone during the late Cretaceous.

More recent (16-71 Ma) volcanism associated with the Galápagos hotspot has also been geochemically linked to the Caribbean Plateau. Hoernle *et al*. (2002) demonstrated that basalts from hotspot tracks accreted along the western coast of South

and Central America (continuing westward as younger, intact linear volcanic features in the Panama basin—the Cocos Ridge, the Carnegie Ridge, and the Malpelo Ridge) exhibit Pb and Nd isotopic compositions that overlap with those of basalts from both the Galápagos Islands and multiple CLIP localities. Hauff et al. (2000a) and Thompson *et al*. (2003) report that Sr, Nd, Pb and Hf isotopic compositions of CLIP are similar to those observed in lavas derived from the Galápagos plume. Geldmacher *et al*. (2003) demonstrated that Hf-Nd-Pb isotopic signatures in CLIP lavas with ages of 70-95 Ma are also found in samples from accreted Galápagos paleo-hotspot tracks (54-65 Ma) and recently formed Galápagos hotspot tracks (<20 Ma). These isotopic similarities suggest that the CLIP was derived from plume head material associated with the initiation of the Galápagos plume.

Mantle temperature calculations also support the idea that the CLIP was formed by melting associated with the head of a mantle plume. Herzberg and Gazel (2009) demonstrated that the FeO and MgO contents of CLIP lavas indicate a mantle potential temperature of 1560 to 1620 °C (~200-300 °C greater than melting temperatures beneath spreading ridges), consistent with a mantle plume mechanism for petrogenesis. These results are consistent with modeling by Hastie and Kerr (2010), which suggests that the primary magmas for CLIP lavas can be reproduced by 30-32% partial melting of a fertile peridotite source with a mantle potential temperature of 1564 to 1614 °C.

Despite significant evidence that a mantle plume was responsible for the formation of the CLIP, alternate models have been proposed. Pindell *et al*. (2006) posited that the formation of a slab window (requiring collision of a spreading ridge with a trench) at a west-dipping subduction zone to the east of the incipient Caribbean

lithosphere was responsible for the magmatism associated with the largest pulse of CLIP activity. Hastie and Kerr (2010), however, found that partial melting of asthenosphere below a downgoing slab (at a potential temperature equal to that of the ambient mantle) triggered by extensional upwelling would not produce enough melt to account for the volume of the CLIP. The authors also noted that geochemical indicators of rocks formed by slab windows (e.g. negative Nb and Ta anomalies) are generally not observed in CLIP lavas.

Although the majority of models suggest that a mantle plume is responsible for the petrogenesis of the CLIP, the mantle source compositions and melting conditions associated with the formation of the oceanic plateau have not been fully constrained. Rare earth element (REE) and isotopic data collected by Sinton *et al*. (1998) suggest that the formation of the CLIP involved both enriched and depleted mantle sources and variable degrees of melting. However, workers examining different sites of the CLIP have posited a number of different mantle sources and melting regimes (e.g. Sen *et al*., 1988; Révillon, 2000; Kerr *et al*., 1996) in order to explain the petrogenesis of the oceanic plateau. Additionally, the extent of variation in mantle source composition and melting processes over time remains unclear (e.g. Sinton *et al*., 1998; Loewen *et al*., 2013).

This thesis presents an updated model for the petrogenesis of the Caribbean Plateau based on geochemical and geochronological data from three CLIP localities—the Curaçao Lava Formation (CLF), the Dumisseau Formation (DF) in Haiti, and the submarine Beata Ridge (BR) south of Hispaniola. These localities define an approximately NW-SE transect across the central-eastern Caribbean Plateau (Figure 1.1). Thus, variations in geochemistry and age distribution among these sites have the potential

to reveal variations in melting processes and source composition across the axis of the plume head that gave rise to the Caribbean Plateau. By incorporating ^{40}Ar-^{39}Ar ages, major and trace element chemistry, and isotope geochemistry into models of partial melting and fractional crystallization, this integrated model provides additional constraints on the spatial and temporal variations in mantle melting and source composition experienced by the CLIP during its emplacement history.

1.2 The Curaçao Lava Formation

The island of Curaçao contains some of the best-preserved subaerial sections of the Caribbean Plateau, and the petrology and stratigraphy of this region are well-documented. Klaver (1987) suggested that the Curaçao Lava Formation (CLF) is more than 5 km thick, and composed predominately of massive and pillow lavas, hyaloclastites and sills. The lower half of the exposed section is dominated by olivine basalts and picrites, some containing as much as 31 wt% MgO (Beets *et al*., 1982). Kerr *et al*. (1996) suggest that the high-MgO picrites are olivine cumulates. The upper half of the CLF consists of more evolved plagioclase- and clinopyroxene-phyric pillow basalts, dolerite sills, and hyaloclastites (Klaver, 1987). Kerr *et al*. (1996) concluded that the picrites of the CLF are related to the basalts by simple fractional crystallization of olivine, clinopyroxene, and plagioclase.

Although stratigraphic relationships and radiometric ages from previous research suggest that the lavas of the CLF were formed relatively rapidly, more recent work has provided evidence of a more prolonged period of emplacement. Only one intercalation of pelagic sediments has been found within the CLF, suggesting that the extrusion of the

lavas occurred during a short timeframe (Klaver, 1987). Sinton *et al*. (1998) obtained ^{40}Ar-^{39}Ar ages of 89.6 ± 1.0 and 88.1 ± 1.2 Ma from lava flows at the top and bottom of the CLF (respectively), as well as an age of 75.9 ± 2.0 Ma from a diabase sill. These ages are consistent with the stratigraphy identified by Klaver (1987), and led Sinton *et al*. (1998) to conclude that the magmatism on Curaçao occurred in two pulses—an initial extrusive phase followed by an intrusive phase. A Re-Os isochron age of 85.0 ± 8.1 Ma has also been obtained for a Curaçao lava flow (Walker *et al*., 1999). Wiedmann (1978) identified ammonites present in sediments intercalated with lava flows as mid-Albian (~105 Ma). However, Kerr *et al*. (2003) noted that these fossils had experienced significant deformation, indicating that they may have been reworked. Wright and Wyld (2011) obtained a U-Pb age of 86.3 ± 0.8 Ma for a quartz diorite plug intruding the CLF, and Humphrey (2010) obtained a U-Pb age of 112.8 ± 7.3 Ma for a baddeleyite from a diabase sill, suggesting an older emplacement age for the CLF. Most recently Loewen *et al*. (2013), however, reported 22 ^{40}Ar-^{39}Ar incremental heating ages for CLF lavas and intrusives between ~60 to ~92 Ma for a suite of tholeiites, sills, and hyaloclastites from the CLF. This larger age range forced a reexamination of volcanism in the CLF. Loewen *et al*. (2013) argued that this broad age range could be explained by repeated melting of residual plume head material beneath the CLIP as a result of asthenospheric flow associated with nearby subduction zones. Mixing between this plume source and upwelling asthenosphere could allow for the episodic eruptions during the approximately 30 m.y. emplacement history for the CLIP.

The source composition(s) and melting conditions of the CLF have also been examined in previous research. Kerr *et al*. (1996) report that the Curaçao lavas have ε_{Nd}

of +6.1 to +7.6, $^{87}Sr/^{86}Sr$ of 0.70296 to 0.70671, and flat REE patterns. Modeling by these authors suggests that the relatively narrow range of isotopic compositions observed for CLF basalts and picrites can be explained by either a homogenous mantle source or by relatively uniform mixing of melts from a heterogeneous source prior to eruption. Loewen *et al*. (2013) found that samples spanning the full age range of the CLF (60-92 Ma) exhibit broadly similar geochemical signatures (e.g. REE patterns, Nb/Zr). This suggests that the melting conditions and/or mantle source composition for the CLF experienced little change over the course of its emplacement.

1.3 The Dumisseau Formation

The Dumisseau Formation (DF) of Haiti is an uplifted section of oceanic crust and associated sedimentary units exposed along the northern margin of the Caribbean Plateau. The upper boundary of the formation is marked by an unconformity, and is overlain by late Eocene limestone. The formation is comprised of interbedded pillow and massive basalts intercalated with pelagic limestones, chert, siltstones, and turbidites. The sequence is cut by multiple dolerite sills and occasional gabbroic intrusions. The basalts and dolerites of the DF contain plagioclase, clinopyroxene, olivine and opaque oxide phenocrysts, with a groundmass composed predominately of clinopyroxene, olivine and opaque oxides. Both basalts and dolerites exhibit glomeroporphyritic, ophitic and intergranular textures. The DF is thought to correspond to oceanic crust associated with the B" acoustic reflector observed across broad areas of the Caribbean plateau, and a similar sequence of tholeiitic basalts, picrites, doleritic sills and intercalated sedimentary

units corresponding to this layer was recovered during DSDP Leg 15 (Donnelly *et al.*, 1973; Maurrasse *et al*., 1979).

Previous research has established that the geochemistry of the DF falls within the range of compositions observed at other CLIP localities. Sen *et al*. (1988) demonstrated that basalts and picrites from the DF are geochemically similar to lavas obtained by ocean drilling from the interior of the Caribbean Plateau during DSDP Leg 15. Samples from both localities exhibit La/Th of ~10, consistent with derivation from a common mantle source. These samples also exhibit $^{87}Sr/^{86}Sr$ of 0.70280 to 0.70316, $^{143}Nd/^{144}Nd$ of 0.512929 to 0.513121, and $^{206}Pb/^{204}Pb$ from 19.00 to 19.27. The isotopic compositions from both localities are similar to those exhibited by Galápagos basalts. Although the majority of the samples are geochemically similar to Caribbean Plateau lavas, several exhibit light REE-enrichment commonly associated with ocean island basalts (OIB). Modeling by Sen *et al*. (1998) indicates that the geochemistry of the majority of DF samples is consistent with 10-25% partial melting of the E-MORB source of Wood (1979), followed by 20-60% fractional crystallization. This is consistent with the contribution of plume source material to the formation of the Caribbean oceanic crust.

Multiple authors have previously examined the temporal range of magmatism at the DF. ^{40}Ar-^{39}Ar plateau ages obtained for whole rock samples from the DF by Sinton *et al*. (1998) range from 96.3 ± 6.5 to 89.9 ± 1.1 Ma. These ages are similar to those of Coniacian to Turonian fossils (94–84 Ma) found in intercalated sediments at the base of the Dumisseau Formation and are older than the late Santonian to early Campanian (84–80 Ma) fossils found in sediments at the top of the formation (Maurrasse *et al*., 1979). Five samples analyzed by Snow *et al*. (2005) produced ^{40}Ar-^{39}Ar total fusion ages

ranging from 95.1 to 92.2 Ma. Although these ages are similar to those obtained by Sinton *et al*. (1998), the analyses exhibited evidence of ^{39}Ar recoil and did not produce statistically valid age plateaus. Loewen *et al*. (2013) report ^{40}Ar-^{39}Ar ages obtained for tholeiites from the DF ranging from ~76 to ~105 Ma. The ages obtained for DF lavas fall within the uppermost portion of the age range observed for the CLIP.

1.4 The Beata Ridge

The Beata Ridge (BR) is a SSW-trending linear feature in the central Caribbean that extends from Cape Beata in Hispaniola (Révillon *et al*., 2000). The structure is 450 km long and 300 km wide, and exhibits a steep western margin and a more gently sloping eastern margin, consistent with E-W extension and normal faulting (Mauffret and Leroy, 1997; Mauffret *et al*., 2001). The BR is located within an area of anomalously thick (up to 20 km) crust (Case *et al*., 1990). Samples of basalt, dolerites, and gabbro collected from the BR are geochemically similar (e.g flat to slightly enriched REE patterns) to samples recovered from nearby central Caribbean sites during the Deep Sea Drilling Program (DSDP) Leg 15 (Révillon *et al*., 2000; Donnelly *et al*., 1973). The gabbros and dolerites of the BR are composed of 40-60 vol. % plagioclase, 25-45 vol. % clinopyroxene and variable but minor olivine phenocrysts. The basalts contain euhedral olivine phenocrysts, augite pheoncrysts and microcrysts, and plagioclase microlites (Révillon *et al*., 2000).

Previous studies of the petrogenesis of BR have found similarities to other LIP localities. Révillon *et al*. (2000) found that the major element compositions of the basalts and dolerites are consistent with fractional crystallization of olivine, clinopyroxene and

plagioclase. As in the CLF, the samples exhibit near-chondritic trace element ratios and flat REE patterns. The gabbros and dolerites exhibit ε_{Nd} of +7.4 to +9.5. The basalts have higher trace element ratios and enriched REE patterns. Modeling by Révillon *et al*. (2000) suggests that the dolerites and gabbros were formed by the pooling of fractional melts of spinel peridotite (~1-10% melting), while the more enriched basalts may have been formed by low degree melting of a source with ε_{Nd} of ~+5.

The timescales of magmatism at the BR have also been constrained by previous work. Révillon *et al*. (2000) obtained ^{40}Ar-^{39}Ar plateau ages ranging from ~55 to ~82 Ma and total fusion ages of ~55 to ~112 Ma for samples from the BR. The authors concluded that the BR consists of a dike and sill complex built during three volcanic episodes at 55, 76 and 90 Ma. These ages cover a similar range to those reported for the BR, CLF, and DF by Loewen *et al*. (2013). Révillon *et al*. (2000) attribute the 90 Ma and potentially the 76 Ma episode to melting associated with the arrival of a mantle plume (the Sala y Gomez and/or Galápagos plume) at the base of the lithosphere, but determined that the 55 Ma episode (and possibly also the 76 Ma episode) was initiated by lithospheric extension and thinning.

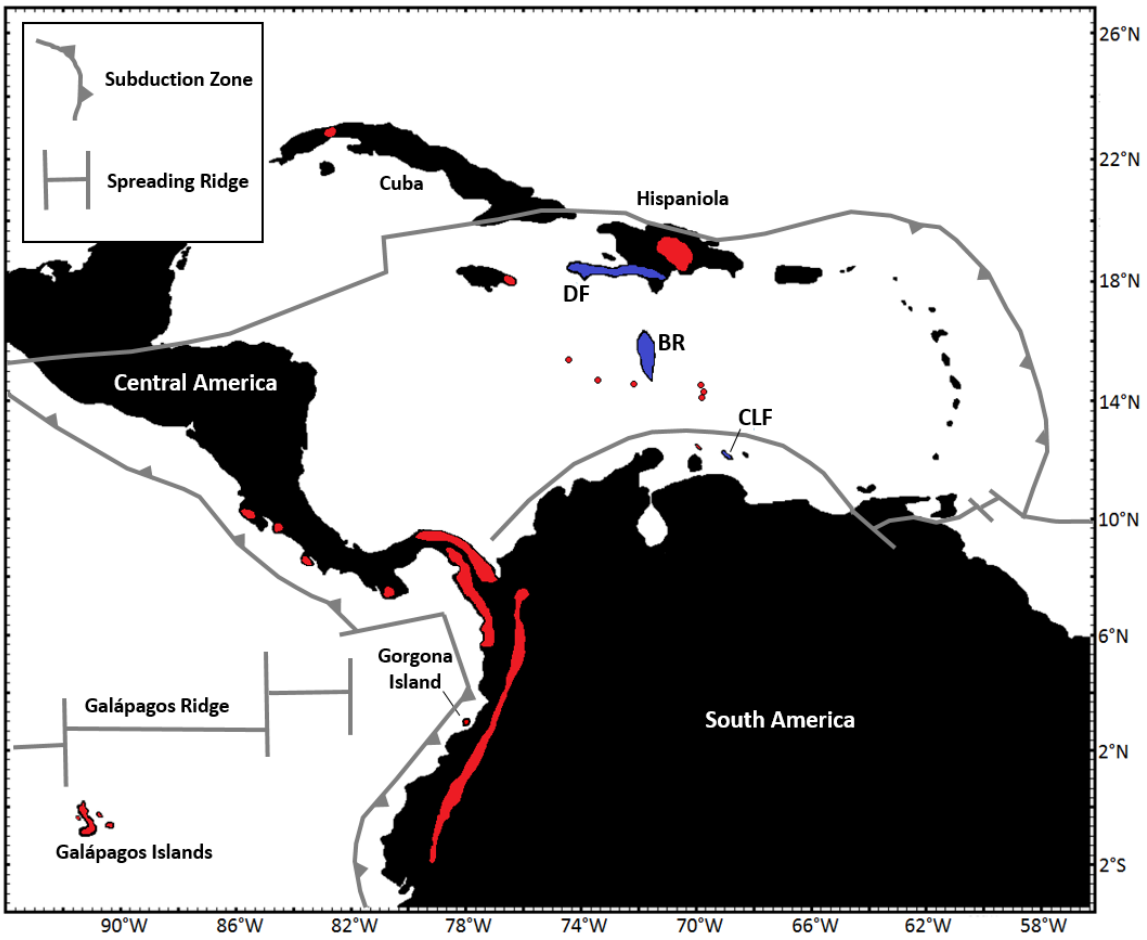

Figure 1.1. Location map of the Caribbean Large Igneous Province (CLIP). The Dumisseau Formation (DF), Beata Ridge (BR), and Curaçao Lava Formation (CLF) are shown in blue, other localities are shown in red. Modified after Kerr et al. (1997) and Loewen *et al*. (2013).

2 Methods

Whole rock samples from the CLF were collected by R. A. Duncan and M. Loewen in April 2010. These samples were supplemented with samples previously examined by Kerr *et al*. (1996) and Klaver *et al*. (1987). Sample locations and brief rock descriptions are provided in Table 2.1. Whole rock samples from the DF are previously described in Maurasse *et al*. (1979) and Sen *et al*. (1988). Samples from both localities were examined in thin section and categorized based on differences in mineral assemblage and texture. Samples in which mineral phases were unidentifiable due to alteration were excluded from further analysis.

Major and trace element data were collected for selected samples from the CLF using X-ray fluorescence spectroscopy (XRF) by Dr. Chris Sinton at the University of Redlands. Additional major element data were collected for CLF and DF whole rock samples using XRF by the Washington State University Geoanalytical Lab. Trace element data were collected using inductively coupled plasma mass spectrometry (ICP-MS) at the Washington State University Geoanalytical Lab. Analytical methods for XRF and ICP-MS are described in Johnson *et al*. (1999) and Knaack *et al*. (1994).

Major and trace element data were collected for olivine, plagioclase, and clinopyroxene in selected CLF and DF samples using Electron Microprobe Analysis (EMPA). EMPA was conducted at Oregon State University using a Cameca SX-100 Electron Microprobe equipped with five wavelength dispersive spectrometers (WDS), one energy dispersive spectrometer (EDS), and a high speed back scattered electron (BSE) imaging system. A total of 45 olivine, 58 pyroxene and 51 plagioclase crystals were analyzed in eight of the CLF samples (two picrites, two poikilitic sills and four

tholeiitic basalts). A total of 11 olivine and 29 pyroxene crystals were analyzed in four of the DF tholeiites. All analyses were conducted using a spot size of 1 μm, a beam intensity of 30 nA and an acceleration voltage of 15 kV. Compositional data for samples and standards analyzed using EMPA are shown in Tables 8.1 through 8.8 in the Appendix.

For samples analyzed for Nd and Sr isotopic compositions, 50 mg of rock powders were digested in a mixture of 1:1 HNO_3 and HF using a CEM MARS-5 Microwave. After digestion, samples were evaporated using the MARS-5. After the first evaporation, 4 mL of 50% HNO_3 was added to each sample and a second evaporation was carried out. Samples were then dried down, mixed with 600 μL 1M HCl, and passed through a column with 1.8 mL AG50 8X resin to remove cations and separate out Sr and REEs. The Sr fraction was subsequently dried overnight, mixed with 200 μL 3M HNO_3 and then dried again. After drying, the sample was mixed with 75 μL 3M HNO_3 and then passed through a column with 50 μL Sr-Spec resin. The REE fraction was dried overnight, combined with 500 μL 0.1 M HCL, and passed through a column with Ln-Spec resin to separate out Nd. Sr and Nd isotopes for five sample were analyzed using a Nu Plasma multicollector ICP-MS at Oregon State University. Reference standards used during analysis yielded average values of $^{143}Nd/^{144}Nd = 0.512097 \pm 0.000008$ for JNdi-1 and $^{87}Sr/^{86}Sr = 0.710418 \pm 0.000017$ for NBS 987. The ratio $^{87}Sr/^{86}Sr$ was normalized during run time to $^{86}Sr/^{88}Sr = 0.1194$; $^{143}Nd/^{144}Nd$ was normalized to $^{146}Nd/^{144}Nd = 0.7218$. Sample data are reported relative to accepted values of $^{143}Nd/^{144}Nd = 0.512115$ for JNdi-1 and $^{87}Sr/^{86}Sr = 0.710245$ for NBS 987.

Table 2.1. Locations and brief descriptions of CLF samples. Ol = olivine, Plag = plagioclase, Cpx = clinopyroxene.

Sample	Latitude	Longitude	Rock Type
Cur10-02	12.1172	-68.88011	Plag-cpx tholeiite
Cur10-03b	12.1187	-68.87856	Ol tholeiite
Cur10-05a	12.16245	-68.99731	Poikilitic sill
Cur10-07	12.13055	-68.81734	Plag-cpx tholeiite
Cur10-09	12.09051	-68.84546	Ol tholeiite
Cur10-11	12.0882	-68.84898	Picrite
Cao3	12.27329	-69.07389	Plag-cpx tholeiite
Cao4a	12.26857	-69.07848	Plag-cpx tholeiite
Cao10	12.14768	-68.84962	Plag-cpx tholeiite
Cao13	12.12588	-68.81816	Poikilitic sill
Cao14	12.13771	-68.83017	Poikilitic sill
Cao16	12.08765	-68.84751	Picrite
Cao17	12.08617	-68.84669	Picrite
Cao18b	12.16639	-68.96115	Poikilitic sill
Cao19	12.25535	-69.07915	Plag-cpx tholeiite
Cao20	12.28987	-69.07974	Plag-cpx tholeiite
Cao21	12.30754	-69.13903	Plag-cpx tholeiite
Cao22	12.37064	-69.13426	Plag-cpx tholeiite
Cao22b	12.37	-69.13488	Hornblende quartz diorite
Cao23	12.0677	-68.81051	Picrite
Cao24	12.07111	-68.81129	Pyroxenic picrite
Cao26	12.07946	-68.80961	Plag-cpx tholeiite
Cao27	12.1003	-68.827	Plag-cpx tholeiite
Cao30	12.14723	-68.84871	Plag-cpx tholeiite
Cao31	12.09617	-68.88527	Tholeiite
Cao32	12.28911	-69.09496	Plag-cpx tholeiite
Cao36	12.37468	-69.14223	Hornblende quartz diorite
Cao39	12.09036	-68.84907	Tholeiite
Cao40a	12.14115	-68.96057	Plag-cpx tholeiite, hyaloclastite
Cao40b	12.14115	-68.96057	Poikilitic sill
Cao41	12.15835	-68.98969	Tholeiite
Cao7	12.26914	-69.07892	Plag-cpx tholeiite, hyaloclastite
Cao35d	12.30081	-69.09429	Plag-cpx tholeiite, hyaloclastite
Cao38b	12.28202	-69.07218	Plag-cpx tholeiite, hyaloclastite

3 Petrography

3.1 Curaçao Lava Formation

Thin sections were prepared for 33 of the samples collected from the CLF by R. A. Duncan and M. W. Loewen (Table 2.1). Of these, five samples were discarded from further analysis due to either excessive alteration or cryptocrystalline texture. Among the 28 remaining samples three unique rock types were identified—picrites, poikilitic sills, and tholeiitic basalts. Picrites and tholeiites were classified on the basis of mineralogy and major element chemistry. Poikolitic sills were classified petrographically on the basis of texture and using field observations by R. A. Duncan and M. W. Loewen. Five samples were classified as picrites, five as poikilitic sills, and 18 as tholeiites. Four of the tholeiites with significant amounts of altered glass were further classified as hyaloclastites. Images of thin sections from CLF samples are shown in Figure 3.1.

The picrites are composed of 40-70 vol. % olivine, 5-15 vol. % clinopyroxene, and 5-10 vol. % spinel. Olivine phenocrysts have sizes of 0.125-5 mm, and are predominately euhedral to subhedral. Hexagonal and rounded morphologies are common, and rare spinifex crystals were also observed. Nearly all of the olivine crystals have been at least partially altered to iddingsite. Clinopyroxene phenocrysts have sizes of up to 2.5 mm, and are predominately euhedral to subhedral. Crystal morphology varies greatly, and includes feathery quench growths as well as skeletal and tabular phenocrysts. Spinel phenocrysts have sizes of up to 0.25 mm. Crystals are predominately euhedral, and exhibit either blocky or elongate morphologies. Spinel phenocrysts are observed both within and between olivine grains, and in the latter case were often grouped together in branching chains.

The poikilitic sills are composed of 25-60 vol. % clinopyroxene, 20-60 vol. % plagioclase, and 5-10 vol. % spinel. Clinopyroxene phenocrysts have sizes of 0.125-2 mm. Crystals are predominately subhedral, and exhibit blocky, tabular and occasionally partially rounded morphologies. Subophitic and ophitic clinopyroxene is common, often forming almost radial clusters with plagioclase crystals. Plagioclase phenocrysts have sizes of 0.05-4.5 mm. Both ophitic and subophitic plagioclase is present. Crystals are predominately subhedral, and exhibit blocky, tabular, and needle morphologies. Plagioclase crystals in several samples have been at least partially altered to sericite. Spinel phenocrysts have sizes of 0.05-1.25 mm. Crystals are predominately euhedral, and exhibit both compact and elongate morphologies. Spinel phenocrysts are observed both within and between clinopyroxene and plagioclase grains. Chlorite is commonly present as an alteration product, and composed up to 5 vol. % of the more pervasively altered samples.

The tholeiites are composed of 1-50 vol. % clinopyroxene, 5-70 vol. % plagioclase, and 5-10 vol. % spinel. Clinopyroxene phenocrysts have sizes of 0.02-1.25 mm. Crystals are predominately subhedral to anhedral, exhibiting blocky, tabular, and occasionally rounded morphologies. Plagioclase phenocrysts have sizes of 0.1-3 mm. Crystals are predominately subhedral to anhedral, and exhibit both tabular and needle-like morphologies. Spinel phenocrysts have sizes of 0.02-0.400 mm. As in the sills, crystals are predominately euhedral, and exhibit both compact and elongate morphologies. The predominant alteration products are chlorite (up to 5 vol. %) and sericite (up to 1 vol. %).

The hyaloclastites are composed of 5-10 vol. % plagioclase and clinopyroxene and up to 90 vol. % glass, with less than 1 vol. % spinel. Nearly all of the glass in the hyaloclastites has been altered to palagonite. Plagioclase crystals are euhedral, present as tabular and needle-like phenocrysts with sizes of 0.125-1.25 mm and as glomerocrysts of up to 3 mm. Clinopyroxene is rare, and occurs as subhedral to euhedral crystals with sizes of up to 0.75 mm.

3.2 Dumisseau Formation

Samples from the DF examined here have been previously described by Maurasse *et al*. (1979) and Sen *et al*. (1988). Thin sections were obtained for 12 of these samples. Images of thin sections are shown in Figure 3.2. The samples are tholeiitic basalts composed of 10-55% plagioclase phenocrysts, 10-35% clinopyroxene phenocrysts, 5-30% olivine phenocrysts and 1-55% groundmass. The most common type of groundmass consists of plagioclase and clinopyroxene (and occasionally olivine) microcrysts, although cryptocrystalline groundmasses are also observed. Several of the samples exhibit porphyritic texture, and contain two populations of differently sized plagioclase phenocrysts. In these samples, the smaller (<1 mm) plagioclase crystals tend to be subophitic to ophitic, while the larger (~2-5 mm) plagioclase partially enclose clinopyroxene phenocrysts. Clinopyroxene phenocrysts are predominately subhedral, and range in size from 0.1 to 0.9 mm. Multiple samples contain clinopyroxene glomerocrysts up to 2 mm across. Olivine phenocrysts range in size from 0.1 to 1 mm and are moderately to pervasively (~40-90 vol. %) altered to iddingsite. Crystals are typically subhedral to euhedral and equant, although more elongate olivine phenocrysts are

observed in HA77-109. Samples are predominately avesicular, although some samples contain up to 3 volume % rounded, equant to slightly elongate vesicles up to 0.5 mm in diameter. Vesicles are typically infilled with carbonate or yellow-orange to yellow-gray clays.

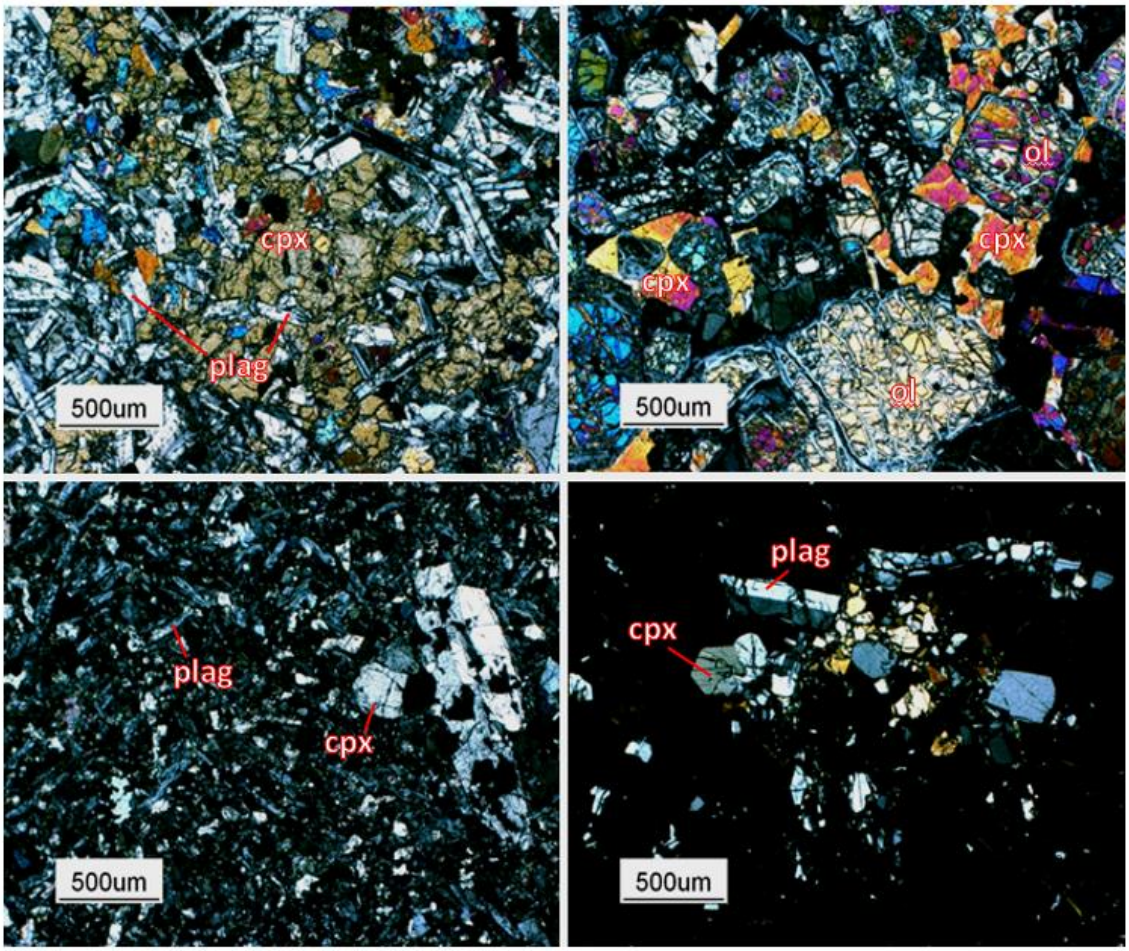

Figure 3.1. Photomicrographs of CLF thin sections. Sample CAO 13 (upper left) is a sill, sample CAO 15a (upper right) is a picrite, sample CAO 22 (lower left) is a tholeiite, and sample CAO 35d (lower right) is a hyaloclastite. Ol = olivine, Plag = plagioclase, Cpx = clinopyroxene.

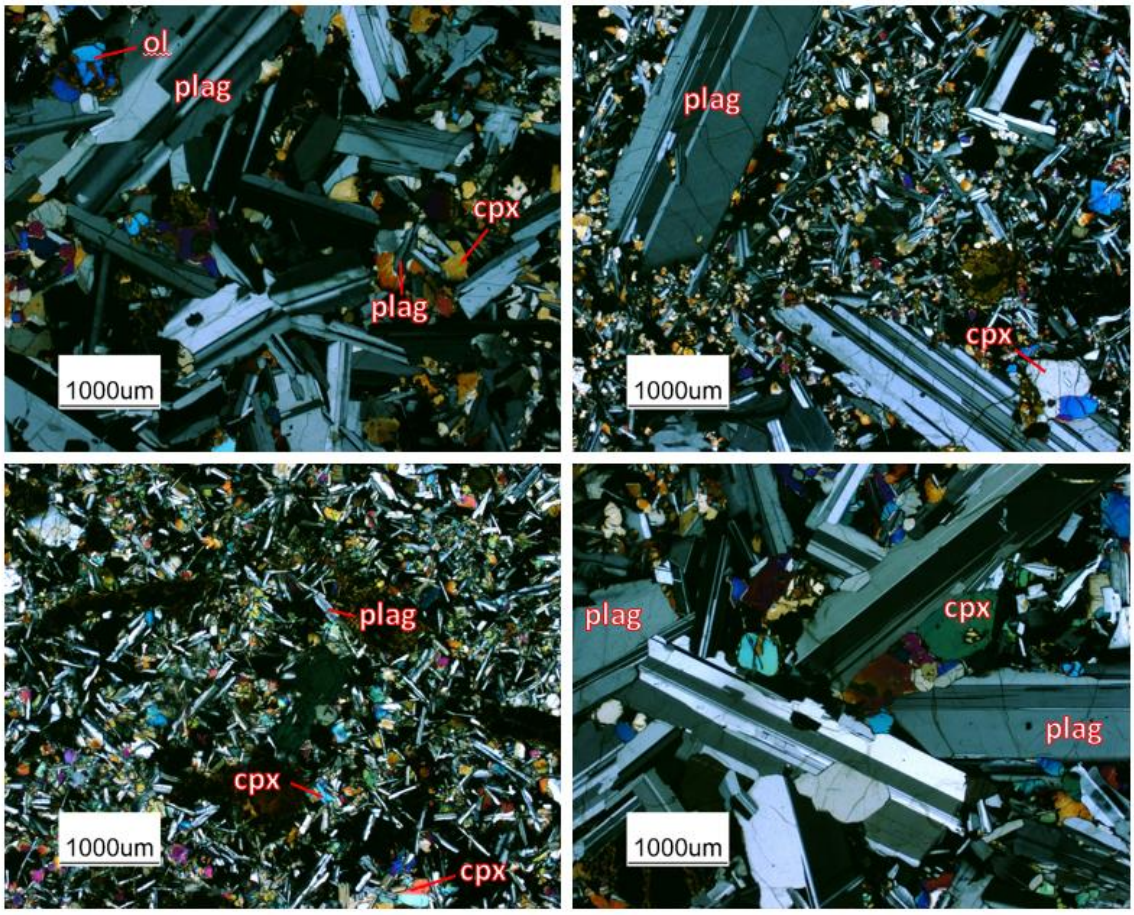

Figure 3.2. Photomicrographs of DF thin sections from samples HA76-28 (upper left), HA77-29 (upper right), HA77-109 (lower left) and HA77-244 (lower right). Ol = olivine, Plag = plagioclase, Cpx = clinopyroxene.

4 Geochemistry

4.1 Curaçao Lava Formation

The major and trace element chemistry of the CLF samples (Table 4.1) exhibit relatively limited variation. All compositions plot within the basalt and picrite fields on a TAS diagram (Figure 4.1). Samples identified as picrites are composed of 21.4 to 29.1 wt% MgO and 41.1 to 44.1 wt% SiO_2. Poikilitic sills are composed of 7.4 to 9.0 wt% MgO and 44.1 to 51.4 wt% SiO_2. Tholeiites are composed of 7.7 to 9.3 wt% MgO and 49.9 to 51.4 wt% SiO_2. In general, the compositions of the picrites, sills, and tholeiites fall within the range of compositions reported by Klaver (1987) for samples with similar petrographic characteristics.

The mineral chemistry of the CLF samples is also relatively consistent, although some minor variations are present. Olivine crystals analyzed using EMPA have compositions of Fo_{81-89}, with a mean composition of Fo_{87} (Figure 4.2). These values are similar to those reported by Klaver (1987) (Fo_{85-90}). Olivine crystals with hexagonal and spinifex morphologies show little compositional variation (Fo_{87-89}) between rim and core. Rounded crystals tend to show slight compositional zoning, exhibiting rims with lower forsterite contents (Fo_{81-86}) than the cores (Fo_{86-89}). Plagioclase crystals have compositions of An_{88-60}, with a mean composition of An_{73} (Figure 4.3). Plagioclase crystals in the poikolitic sills have, on average, lower anorthite content (mean composition An_{71}) than plagioclase in the tholeiites (mean composition An_{76}). Clinopyroxene crystal compositions have ranges of En_{34-70}, Fs_{8-40}, and Wo_{20-46}, with a mean composition of $En_{48}Fs_{16}Wo_{35}$ (Figure 4.4). Clinopyroxene crystals in the picrites

tend to be closer in composition to diopside (mean composition of $En_{44}Fs_{13}Wo_{43}$) than clinopyroxene found in the tholeiites and sills (mean composition of $En_{49}Fs_{17}Wo_{34}$).

4.2 Dumisseau Formation

As with the CLF samples, the major and trace element chemistry (Table 4.2) of the DF samples exhibit relatively minor variation. All samples plot within the basalt fields on a TAS diagram (Figure 4.1). Samples are composed of 4.19 to 7.81 wt% MgO and 48 to 50 wt% SiO_2, and are generally more evolved than the CLF samples. Olivine crystals analyzed using EMPA have compositions of Fo_{67-76}, with a mean composition of Fo_{71} (Figure 4.2). Core and rim compositions are similar, although the latter tend to be slightly more Fe-rich. Pyroxene crystals compositions have compositions of En_{35-50}, Fs_{11-31}, and Wo_{32-40}, with a mean composition of $En_{47}Fs_{16}Wo_{36}$ (Figure 4.4). Pyroxene rim compositions tend to be more Fe-rich and Ca-poor than core compositions.

The isotopic chemistry of the DF samples also varies relatively little. Nd and Sr isotopic compositions for five DF samples are shown in Table 4.3. These samples exhibit $^{143}Nd/^{144}Nd$ of 0.51298 to 0.51306, ε_{Nd} of 6.76 to 8.33 and $^{87}Sr/^{86}Sr$ of 0.70295 to 0.70301. These values are similar to those reported for DF samples by Sen *et al*. (1989).

Table 4.1. Major and trace element compositions of CLF samples. Values are reported in weight percent (major elements) and ppm (trace elements). Samples names ending in "R" are repeat analyses.

Sample	CAO-3	CAO-4A	CAO-10	CAO-13	CAO-14	CAO-15	CAO-16
SiO_2	49.94	49.13	50.75	49.12	49.08	41.10	44.02
TiO_2	1.21	0.97	1.06	0.65	0.95	0.39	0.56
Al_2O_3	13.83	13.52	14.84	15.57	13.98	5.62	8.64
Fe_2O_3*	12.01	10.90	11.56	8.99	10.99	11.32	10.64
MgO	6.98	8.26	8.57	9.00	8.20	29.09	22.26
MnO	0.19	0.17	0.18	0.16	0.18	0.17	0.17
CaO	9.90	11.37	11.92	13.82	11.38	5.49	7.62
K_2O	0.28	0.18	0.32	0.06	0.11	0.02	0.06
Na_2O	3.47	3.01	2.49	1.73	2.61	0.05	1.11
P_2O_5	0.13	0.09	0.08	0.07	0.08	0.05	0.07
SO_3	0.02	0.03	-	0.02	0.02	0.02	0.01
Total	97.96	97.63	100.60	99.19	97.58	93.32	95.16
La	3.25	2.57	2.76	1.65	2.33	1.18	1.85
Ce	8.40	6.76	7.33	4.39	6.11	2.99	4.77
Pr	1.32	1.10	1.16	0.71	0.97	0.46	0.72
Nd	6.79	5.65	5.95	3.73	4.98	2.30	3.57
Sm	2.34	2.01	2.05	1.37	1.77	0.78	1.19
Eu	0.90	0.77	0.81	0.56	0.75	0.31	0.48
Gd	3.22	2.65	2.87	1.84	2.53	1.04	1.63
Tb	0.62	0.52	0.55	0.36	0.48	0.19	0.29
Dy	4.15	3.41	3.60	2.36	3.26	1.29	1.95
Ho	0.89	0.74	0.78	0.52	0.71	0.28	0.42
Er	2.53	2.04	2.16	1.42	1.97	0.76	1.17
Tm	0.37	0.30	0.32	0.21	0.29	0.11	0.17
Yb	2.30	1.83	1.98	1.32	1.81	0.68	1.04
Lu	0.38	0.31	0.32	0.21	0.29	0.11	0.17
Ba	17.56	21.02	15.04	7.85	9.86	3.70	11.81
Th	0.29	0.22	0.23	0.13	0.20	0.10	0.17
Nb	4.15	3.14	3.55	2.13	2.85	1.34	2.16
Y	22.73	18.60	19.14	12.78	17.15	6.72	10.31
Hf	1.62	1.31	1.43	0.89	1.23	0.53	0.80
Ta	0.29	0.22	0.27	0.15	0.21	0.09	0.15
U	0.09	0.07	0.08	0.05	0.07	0.03	0.05
Pb	0.19	0.16	0.63	0.48	0.60	0.08	0.24
Rb	3.56	1.80	0.74	0.44	1.28	0.62	2.37
Cs	0.02	0.01	0.00	0.00	0.01	0.02	0.01
Sr	119.94	101.85	224.36	88.17	90.77	12.90	60.09
Sc	48.14	46.95	49.77	45.28	48.46	22.54	29.87
Zr	56.52	46.40	49.74	30.29	41.96	18.18	28.06

Table 4.1 (Continued)

Sample	CAO-17	CAO-18	CAO-19	CAO-19R	CAO-20	CAO-21	CAO-22
SiO_2	44.07	50.44	49.93	50.38	51.18	49.69	47.44
TiO_2	0.58	1.14	1.02	1.02	1.21	0.87	0.92
Al_2O_3	8.77	14.21	14.45	14.55	13.78	14.40	13.88
Fe_2O_3*	10.52	11.83	11.17	11.04	11.64	10.38	11.02
MgO	21.44	7.53	7.68	7.67	6.85	8.45	8.76
MnO	0.16	0.20	0.17	0.17	0.18	0.17	0.19
CaO	7.60	11.19	10.67	10.73	11.35	11.15	10.18
K_2O	0.06	0.06	0.37	0.37	0.07	0.27	0.94
Na_2O	0.86	1.96	3.17	3.17	2.50	3.02	2.73
P_2O_5	0.07	0.10	0.09	0.09	0.10	0.08	0.19
SO_3	0.02	0.02	0.02	0.01	0.02	0.03	0.02
Total	94.15	98.68	98.74	99.20	98.88	98.51	96.27
La	1.98	3.28	2.74	2.74	3.32	2.35	3.49
Ce	5.05	8.19	7.27	7.28	8.54	6.24	9.36
Pr	0.77	1.23	1.16	1.19	1.30	1.00	1.55
Nd	3.79	6.25	5.99	6.12	6.77	5.08	8.03
Sm	1.26	2.14	2.08	2.15	2.34	1.76	2.63
Eu	0.50	0.89	0.85	0.87	0.90	0.71	0.94
Gd	1.66	2.96	3.01	3.02	3.23	2.49	3.19
Tb	0.30	0.56	0.58	0.57	0.61	0.49	0.55
Dy	2.06	3.88	3.93	3.86	4.09	3.28	3.44
Ho	0.44	0.84	0.83	0.85	0.90	0.72	0.72
Er	1.19	2.34	2.36	2.33	2.54	2.03	1.99
Tm	0.17	0.35	0.34	0.34	0.37	0.31	0.28
Yb	1.09	2.18	2.17	2.12	2.35	1.91	1.75
Lu	0.17	0.35	0.34	0.33	0.38	0.31	0.27
Ba	25.54	7.19	27.82	26.19	24.91	11.65	242.90
Th	0.19	0.27	0.23	0.25	0.28	0.21	0.48
Nb	2.24	3.97	3.09	3.10	4.29	2.63	2.38
Y	10.60	20.68	20.70	20.86	22.34	16.73	18.00
Hf	0.85	1.54	1.51	1.49	1.63	1.21	1.32
Ta	0.16	0.28	0.22	0.22	0.31	0.19	0.16
U	0.05	0.11	0.09	0.09	0.10	0.06	0.24
Pb	0.20	1.06	0.86	0.86	0.82	0.20	0.66
Rb	3.39	0.55	7.82	7.92	0.96	2.71	12.55
Cs	0.15	0.00	0.11	0.11	0.01	0.24	0.07
Sr	95.36	80.80	288.09	295.42	123.49	151.43	267.02
Sc	30.24	48.51	47.35	47.25	48.21	47.84	45.84
Zr	29.04	52.36	51.22	51.50	56.39	40.90	43.51

Table 4.1 (Continued)

Sample	CAO-22B	CAO-23	CAO-24	CAO-26	CAO-27	CAO-30	CAO-31
SiO_2	-	50.24	44.11	50.01	50.62	49.96	47.10
TiO_2	-	0.73	0.45	0.86	0.87	1.02	0.76
Al_2O_3	-	12.68	7.42	13.09	13.48	14.05	12.27
Fe_2O_3*	-	9.88	11.25	9.85	10.13	11.07	8.83
MgO	-	9.18	27.00	8.66	9.35	8.38	7.92
MnO	-	0.19	0.17	0.17	0.17	0.18	0.16
CaO	-	13.93	6.63	13.79	12.09	11.98	18.55
K_2O	-	0.03	0.02	0.07	0.14	0.24	0.03
Na_2O	-	1.86	0.50	1.54	2.46	2.58	0.12
P_2O_5	-	0.07	0.05	0.08	0.08	0.09	0.07
SO_3	-	0.02	0.01	0.01	0.01	0.01	0.01
Total	-	98.81	97.61	98.13	99.40	99.56	95.82
La	7.87	2.48	1.48	3.01	3.25	2.65	2.93
Ce	16.67	6.24	3.79	7.46	7.90	7.09	6.94
Pr	2.29	0.95	0.59	1.13	1.17	1.12	1.04
Nd	9.85	4.62	2.87	5.65	5.70	5.76	5.07
Sm	2.34	1.53	0.98	1.81	1.91	2.00	1.68
Eu	0.87	0.61	0.37	0.70	0.71	0.78	0.71
Gd	2.29	2.13	1.29	2.43	2.44	2.79	2.22
Tb	0.36	0.40	0.24	0.46	0.46	0.53	0.41
Dy	2.17	2.75	1.62	3.05	3.12	3.56	2.69
Ho	0.43	0.60	0.34	0.65	0.65	0.76	0.58
Er	1.21	1.67	0.97	1.77	1.81	2.09	1.59
Tm	0.17	0.25	0.14	0.26	0.26	0.31	0.23
Yb	1.10	1.54	0.87	1.64	1.65	1.92	1.43
Lu	0.18	0.25	0.14	0.26	0.27	0.31	0.22
Ba	355.67	10.34	5.33	15.23	25.05	11.01	5.45
Th	1.01	0.27	0.15	0.28	0.29	0.23	0.25
Nb	2.67	3.08	1.71	3.51	3.71	3.31	2.94
Y	11.16	14.78	8.49	16.10	16.32	18.59	14.06
Hf	1.76	1.05	0.64	1.23	1.25	1.36	1.09
Ta	0.19	0.22	0.12	0.24	0.25	0.24	0.21
U	0.37	0.19	0.04	0.08	0.09	0.06	0.07
Pb	1.26	2.83	0.19	0.26	0.24	0.20	0.45
Rb	15.83	0.53	1.00	0.90	1.64	0.66	0.18
Cs	0.09	0.00	0.01	0.01	0.01	0.01	0.01
Sr	448.66	56.95	38.87	91.55	95.77	221.89	11.69
Sc	16.49	42.45	25.66	43.28	44.27	47.89	35.88
Zr	63.96	36.58	22.69	43.21	43.44	47.90	38.24

Table 4.1 (Continued)

Sample	CAO-32	CAO-36	CAO-36R	CAO-39	CAO-40A	CAO-40B	CAO-41
SiO_2	49.98	-	-	44.42	51.27	51.41	48.91
TiO_2	1.20	-	-	0.78	1.04	1.20	0.92
Al_2O_3	13.37	-	-	14.70	14.05	13.73	14.03
Fe_2O_3*	12.58	-	-	8.94	11.39	12.87	10.89
MgO	7.11	-	-	6.56	8.01	7.63	9.68
MnO	0.19	-	-	0.15	0.19	0.20	0.19
CaO	10.77	-	-	19.92	12.45	11.70	11.75
K_2O	0.09	-	-	0.02	0.04	0.11	0.07
Na_2O	1.83	-	-	0.19	1.80	1.81	1.80
P_2O_5	0.09	-	-	0.07	0.09	0.10	0.08
SO_3	0.02	-	-	0.02	0.01	0.02	0.01
Total	97.23	-	-	95.77	100.34	100.78	98.33
La	2.98	15.48	15.46	3.49	3.41	3.78	3.04
Ce	7.70	31.19	31.47	7.97	8.67	9.91	7.66
Pr	1.22	4.06	4.08	1.13	1.34	1.55	1.18
Nd	6.28	16.40	16.71	5.57	6.67	7.70	5.85
Sm	2.24	3.85	3.99	1.73	2.20	2.64	1.93
Eu	0.84	1.20	1.21	0.76	0.87	0.97	0.76
Gd	2.98	3.94	3.95	2.31	3.01	3.44	2.63
Tb	0.58	0.66	0.67	0.42	0.56	0.64	0.49
Dy	3.97	4.26	4.23	2.87	3.74	4.23	3.20
Ho	0.86	0.86	0.87	0.60	0.80	0.91	0.69
Er	2.39	2.37	2.44	1.66	2.20	2.54	1.98
Tm	0.35	0.35	0.35	0.25	0.32	0.38	0.28
Yb	2.24	2.16	2.24	1.51	2.00	2.35	1.77
Lu	0.36	0.34	0.35	0.25	0.32	0.38	0.28
Ba	20.49	1078.92	1086.66	7.01	10.61	23.42	12.31
Th	0.28	4.10	4.11	0.34	0.34	0.38	0.26
Nb	3.77	6.05	6.15	3.63	4.07	4.78	3.54
Y	21.05	22.08	22.36	15.06	19.53	22.67	17.23
Hf	1.55	3.86	3.92	1.17	1.52	1.78	1.35
Ta	0.27	0.43	0.44	0.26	0.30	0.35	0.25
U	0.08	1.21	1.22	0.13	0.12	0.15	0.13
Pb	0.33	6.60	6.61	2.82	1.09	1.12	1.91
Rb	1.03	28.31	28.55	0.36	0.37	1.42	0.79
Cs	0.01	1.37	1.40	0.03	0.01	0.01	0.00
Sr	133.29	363.64	365.07	19.21	92.93	90.57	86.24
Sc	49.53	20.88	20.96	40.81	48.66	48.02	44.36
Zr	52.32	142.35	146.57	40.89	51.93	62.22	47.02

Table 4.1 (Continued)

Sample	CUR-10-02	CUR-10-3b	CUR-10-5a	CUR-10-07	CUR-10-09	CUR-10-11
SiO_2	50.88	50.27	50.58	50.64	51.41	43.67
TiO_2	1.01	0.86	1.22	0.91	0.89	0.54
Al_2O_3	14.01	13.55	13.90	13.60	14.01	8.31
Fe_2O_3*	10.88	10.20	12.59	10.44	10.33	10.58
MgO	7.94	9.05	7.38	8.29	8.59	22.83
MnO	0.17	0.18	0.20	0.16	0.18	0.16
CaO	10.78	12.71	9.99	11.74	12.05	7.37
K_2O	0.19	0.03	0.05	0.11	0.08	0.05
Na_2O	3.32	2.45	3.66	2.76	2.51	0.98
P_2O_5	0.13	0.09	0.10	0.07	0.09	0.07
SO_3	0.01	0.01	0.01	0.01	0.01	0.01
Total	99.32	99.40	99.68	98.73	100.15	94.57
La	2.77	2.99	3.35	2.32	3.26	1.81
Ce	7.34	7.33	8.77	6.17	7.96	4.61
Pr	1.17	1.11	1.36	1.00	1.19	0.71
Nd	6.01	5.51	6.87	5.20	5.71	3.50
Sm	2.12	1.81	2.38	1.85	1.84	1.15
Eu	0.85	0.70	0.92	0.74	0.73	0.47
Gd	2.92	2.43	3.31	2.57	2.48	1.56
Tb	0.56	0.45	0.63	0.49	0.47	0.28
Dy	3.76	3.01	4.23	3.26	3.07	1.87
Ho	0.80	0.64	0.92	0.70	0.66	0.40
Er	2.27	1.80	2.60	1.98	1.85	1.10
Tm	0.33	0.26	0.38	0.29	0.27	0.17
Yb	2.08	1.64	2.40	1.80	1.69	1.00
Lu	0.32	0.26	0.38	0.30	0.26	0.16
Ba	26.02	10.21	5.70	8.33	21.83	13.88
Th	0.31	0.27	0.30	0.19	0.32	0.16
Nb	2.91	3.27	4.22	2.85	3.77	2.07
Y	20.14	15.94	22.96	17.46	16.44	9.95
Hf	1.43	1.19	1.71	1.27	1.25	0.77
Ta	0.20	0.22	0.30	0.21	0.25	0.14
U	0.07	0.07	0.08	0.06	0.09	0.05
Pb	0.20	0.24	0.27	0.17	0.27	0.16
Rb	2.76	0.36	0.58	0.64	1.04	2.47
Cs	0.02	0.00	0.01	0.00	0.00	0.06
Sr	156.87	97.86	155.13	179.67	152.86	73.08
Sc	46.76	43.46	50.76	47.52	45.12	29.17
Zr	49.23	42.44	58.10	43.16	43.89	27.13

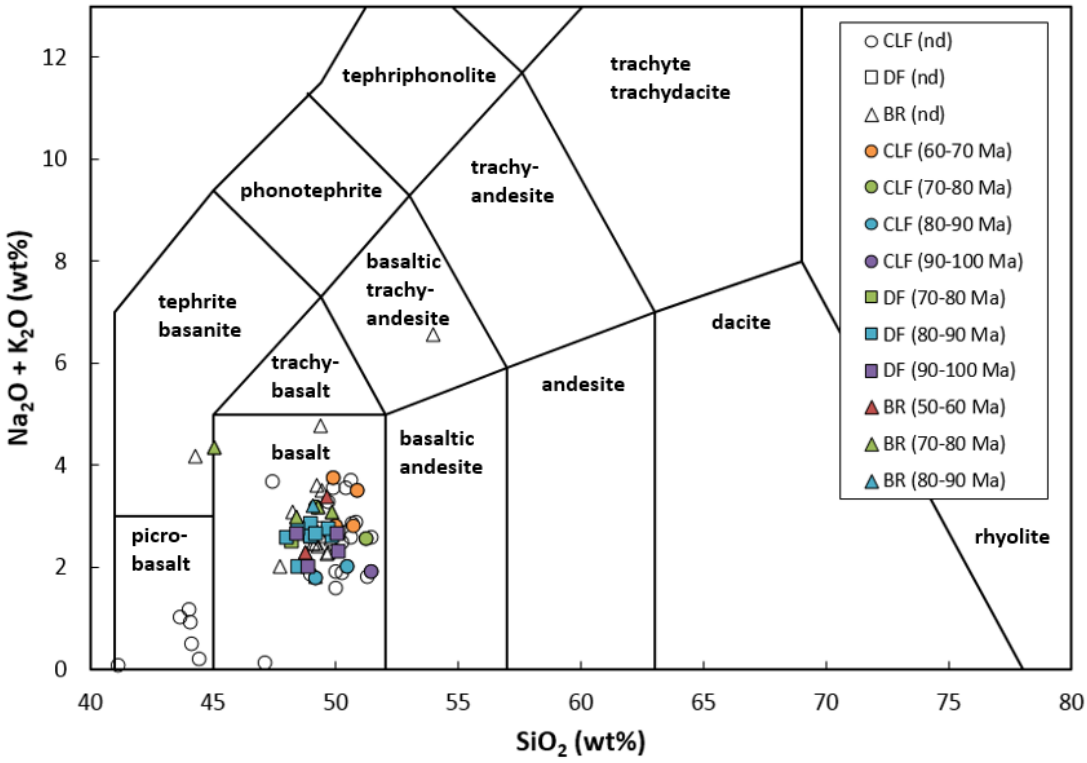

Figure 4.1. Total Alkali Silica (TAS) diagram showing composition of samples from the CLF, DF, and BR. BR samples are from Révillon *et al*. (2000). Ages are from Loewen *et al*. (2013).

Table 4.2. Major and trace element compositions of DF samples. Values are reported in weight percent (major elements) and ppm (trace elements). Samples names ending in "R" are repeat analyses.

Sample	HA-76-117	HA-76-165	HA-77-28	HA-77-29	HA-77-62	HA-77-109	HA-77-110
SiO_2	48.01	49.25	50.11	48.92	50.14	48.88	48.49
TiO_2	2.87	2.91	3.17	3.23	1.31	2.17	2.16
Al_2O_3	14.79	14.17	13.73	14.98	15.06	13.60	13.73
FeO*	13.15	12.70	12.76	12.24	11.89	11.83	11.64
MgO	5.08	5.54	5.94	5.29	6.28	7.81	7.73
MnO	0.22	0.19	0.21	0.20	0.20	0.21	0.23
CaO	11.46	11.27	11.00	11.12	12.09	12.26	12.52
K_2O	0.12	0.27	0.27	0.32	0.09	0.06	0.07
Na_2O	2.48	2.47	2.44	2.53	2.24	1.96	1.95
P_2O_5	0.25	0.27	0.28	0.29	0.11	0.17	0.17
Total	98.41	99.03	99.90	99.14	99.41	98.95	98.68
La	11.80	12.65	14.00	13.62	3.66	7.61	7.53
Ce	29.80	31.77	34.67	34.23	9.48	19.63	19.57
Pr	4.44	4.74	5.15	5.07	1.53	3.00	3.01
Nd	21.23	22.58	24.43	24.17	8.07	14.77	14.73
Sm	6.04	6.51	6.95	6.90	2.88	4.47	4.48
Eu	2.18	2.28	2.32	2.36	1.14	1.62	1.59
Gd	6.73	7.15	7.45	7.69	4.14	5.03	5.09
Tb	1.15	1.23	1.25	1.29	0.82	0.84	0.85
Dy	6.72	7.33	7.53	7.56	5.60	5.04	5.04
Ho	1.31	1.42	1.44	1.46	1.25	0.97	0.97
Er	3.26	3.63	3.64	3.67	3.52	2.46	2.43
Tm	0.45	0.49	0.49	0.49	0.52	0.33	0.32
Yb	2.60	2.90	2.83	2.93	3.33	1.93	1.93
Lu	0.39	0.43	0.44	0.44	0.53	0.29	0.29
Ba	45.23	55.99	67.17	69.55	20.79	21.07	20.61
Th	0.99	1.05	1.20	1.13	0.35	0.61	0.63
Nb	13.42	14.82	15.78	15.35	3.46	8.78	8.76
Y	31.70	35.22	35.36	35.88	31.16	23.78	23.40
Hf	4.26	4.55	4.83	4.88	2.03	2.97	2.96
Ta	0.90	1.03	1.06	1.04	0.24	0.61	0.60
U	0.30	0.33	0.37	0.35	0.11	0.19	0.19
Pb	1.01	1.33	1.01	0.83	0.54	0.50	0.53
Rb	0.60	2.89	2.54	4.89	1.39	0.98	1.28
Cs	0.00	0.01	0.04	0.04	0.01	0.09	0.04
Sr	274.71	248.37	261.51	264.06	90.00	211.21	211.36
Sc	35.66	36.85	35.74	34.15	51.12	35.23	35.03
Zr	157.14	173.79	184.41	185.49	70.80	108.57	109.56

Table 4.2 (Continued)

Sample	HA-77-144	HA-77-159	HA-77-164	HA-77-170	HA-77-178	HA-77-237	HA-77-244
SiO_2	49.72	48.21	50.01	48.36	48.45	49.15	48.95
TiO_2	2.92	3.39	3.18	2.58	2.73	2.78	2.47
Al_2O_3	13.67	13.08	13.27	15.45	15.38	14.53	15.11
FeO*	13.03	14.27	13.83	12.33	12.56	13.30	12.18
MgO	5.62	5.74	5.96	4.19	4.98	5.74	6.13
MnO	0.20	0.23	0.20	0.19	0.22	0.18	0.18
CaO	11.08	10.88	10.63	10.88	11.01	10.67	11.46
K_2O	0.31	0.13	0.26	0.14	0.19	0.21	0.23
Na_2O	2.43	2.39	2.38	2.52	2.57	2.45	2.40
P_2O_5	0.30	0.31	0.27	0.23	0.24	0.22	0.21
Total	99.29	98.63	99.99	96.88	98.31	99.23	99.33
La	15.64	15.19	12.36	11.62	11.78	10.73	9.94
Ce	37.71	38.05	31.87	28.63	29.12	26.20	25.04
Pr	5.38	5.56	4.78	4.22	4.30	3.91	3.72
Nd	25.40	26.25	23.11	20.08	20.37	18.60	17.81
Sm	7.08	7.45	6.85	5.59	5.86	5.40	5.20
Eu	2.34	2.47	2.31	2.06	2.10	1.92	1.90
Gd	7.69	8.11	7.55	6.34	6.54	6.01	5.75
Tb	1.28	1.32	1.26	1.06	1.09	1.00	0.98
Dy	7.48	7.99	7.41	6.20	6.43	6.00	5.76
Ho	1.46	1.52	1.42	1.21	1.25	1.14	1.12
Er	3.65	3.82	3.62	3.08	3.15	2.90	2.79
Tm	0.49	0.51	0.47	0.41	0.43	0.39	0.39
Yb	2.84	3.01	2.81	2.44	2.51	2.32	2.24
Lu	0.44	0.45	0.42	0.36	0.37	0.35	0.33
Ba	73.36	61.97	53.82	41.36	53.24	52.75	44.23
Th	1.38	1.29	1.05	0.93	0.98	0.87	0.79
Nb	16.85	17.54	14.27	12.81	13.25	12.34	11.21
Y	35.78	37.18	35.00	29.52	30.30	28.10	27.35
Hf	4.99	5.17	4.80	3.92	4.00	3.76	3.57
Ta	1.13	1.19	1.01	0.87	0.89	0.85	0.77
U	0.42	0.38	0.33	0.29	0.30	0.27	0.25
Pb	2.55	1.08	0.77	1.59	1.47	1.60	0.60
Rb	3.56	2.96	2.70	1.32	1.35	1.84	3.03
Cs	0.01	0.04	0.02	0.03	0.01	0.01	0.01
Sr	259.06	266.92	236.01	287.43	280.34	258.73	261.83
Sc	35.54	37.42	35.33	30.65	32.02	33.29	32.56
Zr	190.84	198.35	182.41	148.00	153.21	141.35	134.46

Table 4.2 (Continued)

Sample	HA-77-245	HA-76-28	HA-76-28R
SiO_2	48.94	49.83	49.43
TiO_2	3.10	2.50	2.50
Al_2O_3	13.47	15.13	15.07
FeO*	13.80	12.07	12.04
MgO	6.03	6.76	6.73
MnO	0.21	0.19	0.18
CaO	10.76	11.39	11.34
K_2O	0.18	0.21	0.20
Na_2O	2.43	2.42	2.42
P_2O_5	0.28	0.22	0.21
Total	99.19	100.71	100.13
La	13.89	9.95	-
Ce	34.33	24.97	-
Pr	5.03	3.76	-
Nd	23.61	18.06	-
Sm	6.70	5.18	-
Eu	2.30	1.89	-
Gd	7.39	5.79	-
Tb	1.23	0.98	-
Dy	7.28	5.85	-
Ho	1.41	1.14	-
Er	3.53	2.83	-
Tm	0.47	0.38	-
Yb	2.79	2.23	-
Lu	0.42	0.34	-
Ba	73.46	51.20	-
Th	1.19	0.81	-
Nb	16.20	11.29	-
Y	34.43	27.80	-
Hf	4.83	3.62	-
Ta	1.08	0.75	-
U	0.36	0.25	-
Pb	1.19	0.65	-
Rb	2.49	1.92	-
Cs	0.06	0.01	-
Sr	265.11	261.51	-
Sc	35.18	31.87	-
Zr	178.08	135.37	-

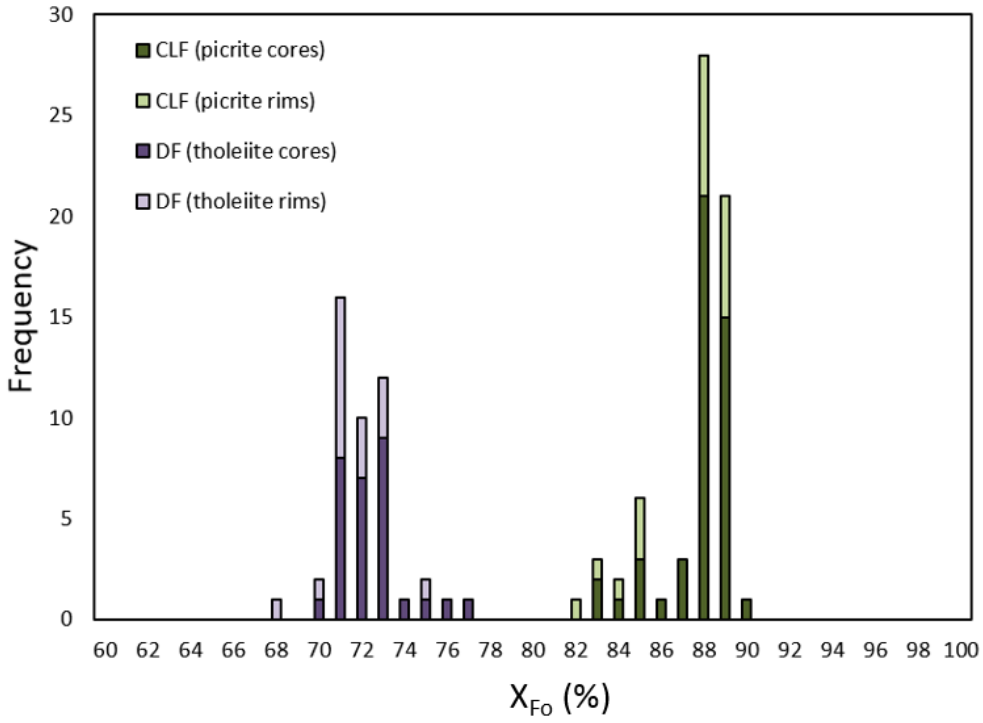

Figure 4.2. Histograms of compositions of rims and cores of olivine phenocrysts in CLF picrites and DF tholeiites, expressed as percent forsterite.

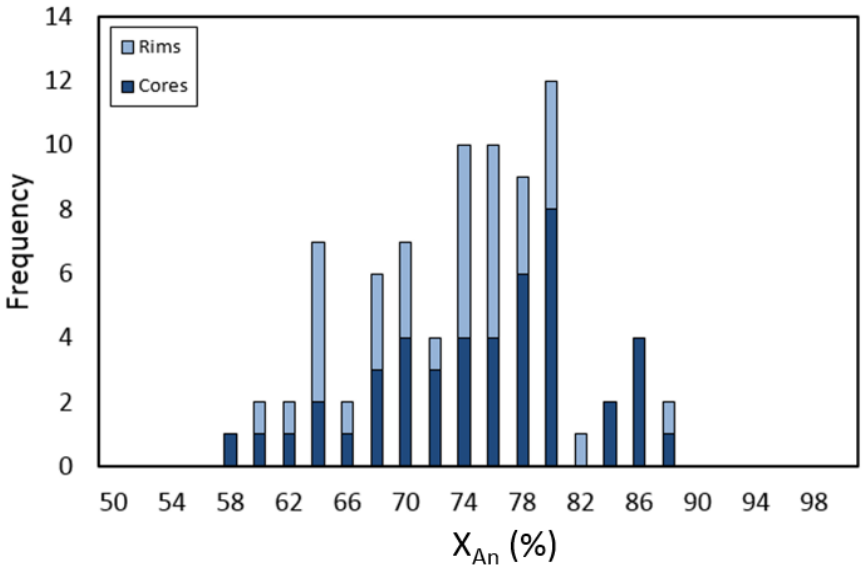

Figure 4.3. Histograms of compositions of rims and cores of plagioclase in CLF plagioclase phenocrysts, expressed as percent anorthite.

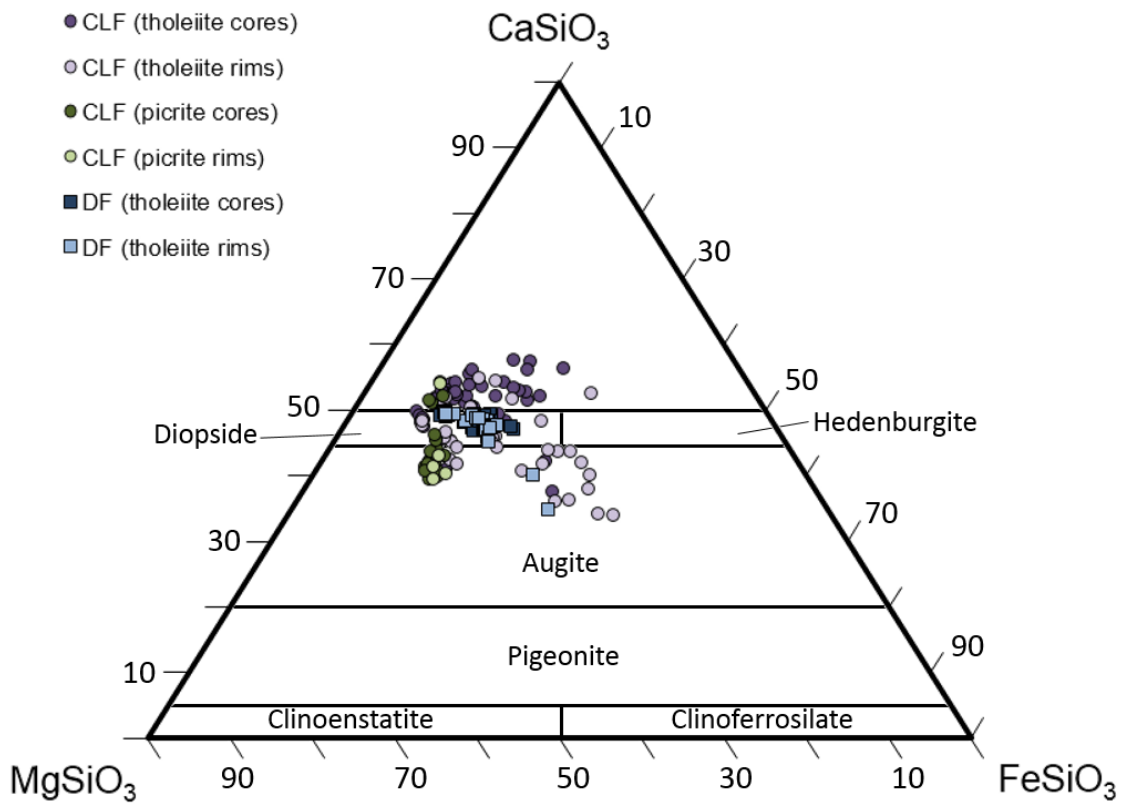

Figure 4.4. En-Wo-Fs ternary diagram showing composition of clinopyroxene phenocrysts from the CLF and DF.

Table 4.3. Nd and Sr isotopic compositions for DF samples analyzed in this study. Ages used to calculate initial compositions are from Loewen *et al*. (2013). $^{147}Sm/^{144}Nd$ and $^{87}Rb/^{86}Sr$ were calculated using trace element data in Tables 10 and 11.

Sample	HA-76-28	HA-77-62	HA-77-110	HA-77-159	HA-77-237
$^{143}Nd/^{144}Nd$	0.512989	0.513065	0.512986	0.512985	0.512989
2σ	0.000009	0.000008	0.000007	0.000009	0.000010
$^{87}Sr/^{86}Sr$	0.702963	0.703001	0.703014	0.702991	0.702946
2σ	0.000013	0.000015	0.000013	0.000015	0.000017
$^{147}Sm/^{144}Nd$	0.174	0.216	0.184	0.172	0.176
$^{87}Rb/^{86}Sr$	0.021	0.045	0.018	0.032	0.021
ε_{Nd} (0 Ma)	6.85	8.33	6.80	6.76	6.86
ε_{Nd} (T)	7.11	8.08	6.94	7.01	7.09
$(^{143}Nd/^{144}Nd)_i$	0.512890	0.512917	0.512879	0.512899	0.512891
$(^{87}Sr/^{86}Sr)_i$	0.702937	0.702935	0.702991	0.702956	0.702921

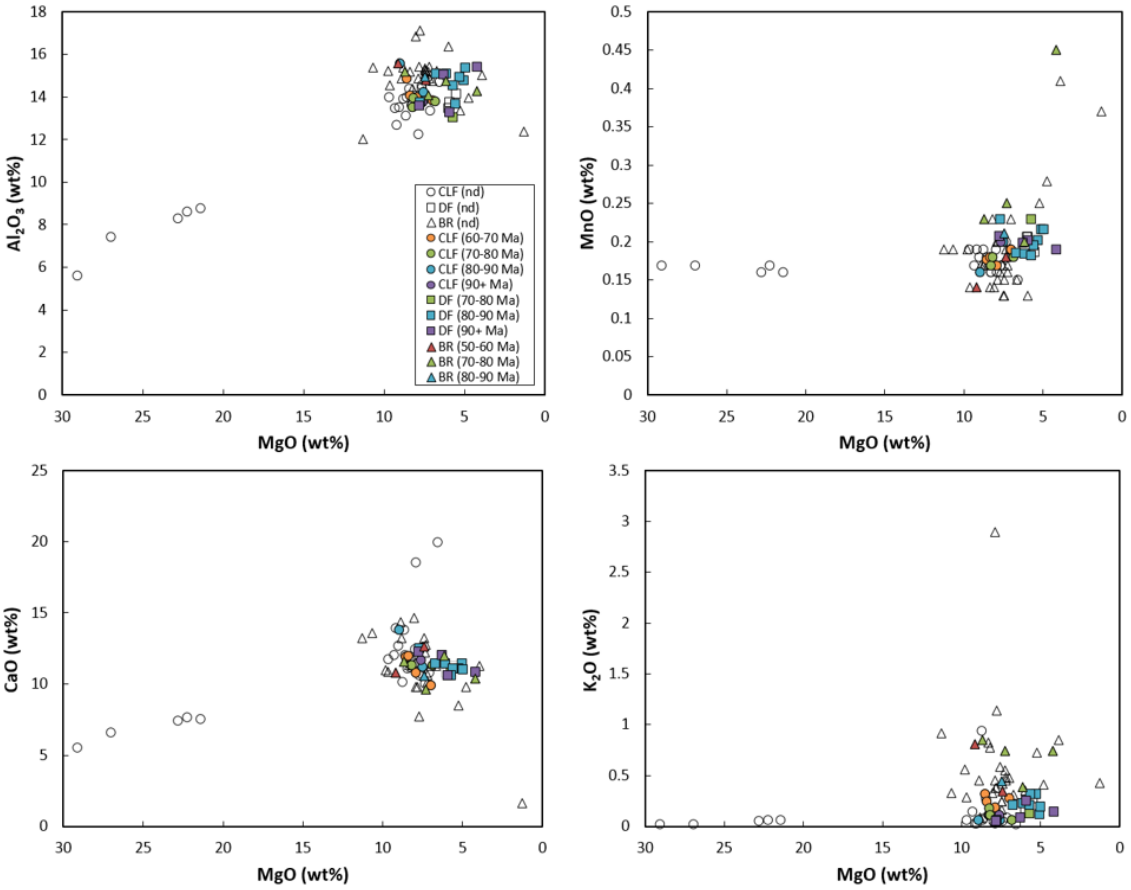

Figure 4.5. Major and minor element variation diagrams for CLF, DF and BR samples of various ages. BR samples are previously described by Révillon *et al*. (2000). Ages are from Loewen *et al*. (2013).

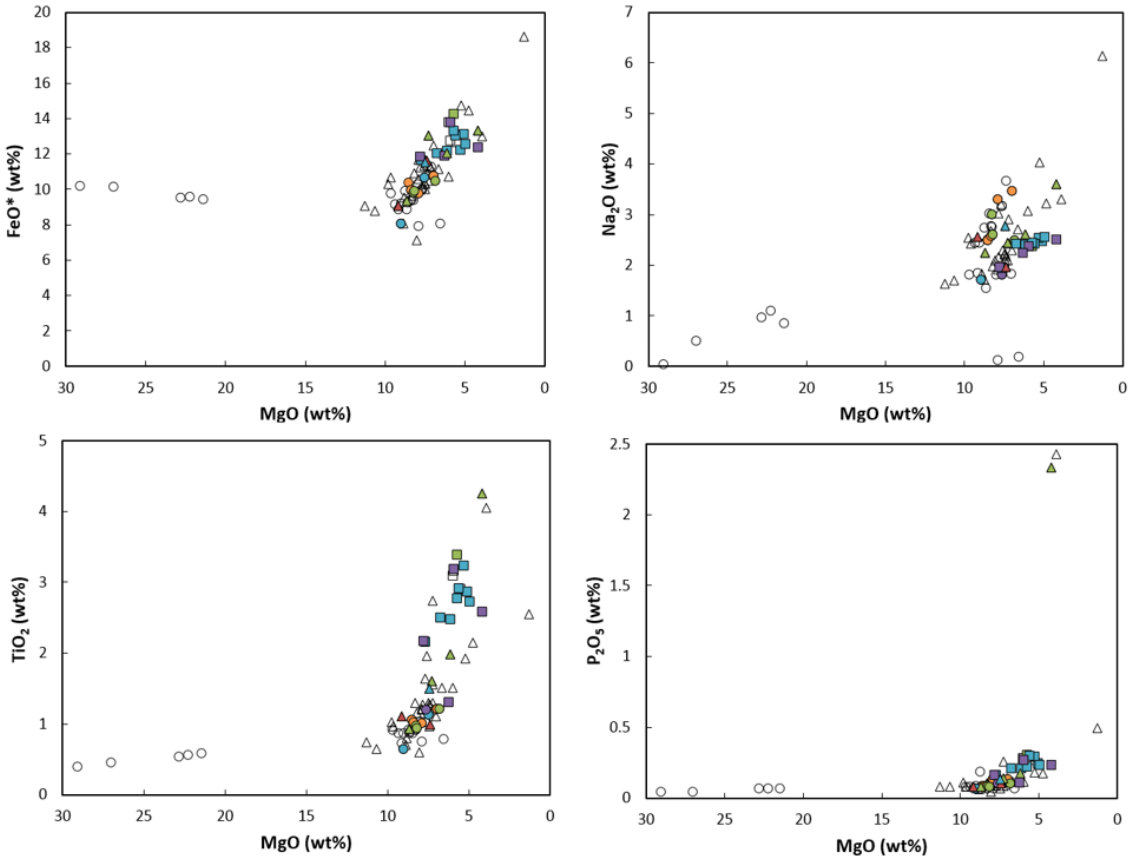

Figure 4.5 (Continued)

5 Discussion

5.1 Magma Evolution

The major element chemistry of samples from the CLF, BR, and DF provide a window into the formation and evolution of the parental magmas for the CLIP. Major and minor element variation diagrams for CLF, DF and BR samples are shown in Figure 4.5. Although trends on several diagrams (particularly Al_2O_3, FeO*, and CaO) exhibit inflections at ~7-10 wt% MgO that appear to be consistent with the onset of plagioclase and clinopyroxene crystallization, the position of the DF samples relative to the CLF and BR samples suggests that samples from all three localities are not necessarily related by a single parental magma. Although the samples appear to fall onto a single trend on the FeO* diagram, the high degree of scatter in the Al_2O_3 and CaO diagrams suggests that multiple parental magmas may be required to explain the evolution of this magmatic suite.

In order to address this possibility, parental magma evolution was modeled by using the MELTS software package to generate liquid lines of descent produced by fractional crystallization (Ghiorso and Sack, 1995; Asimow and Ghiorso, 1998). The end member parental magma compositions used in the model are shown in Table 5.1. These compositions are based on the primary magmas for the CLF calculated by Hastie and Kerr (2010). These authors calculated these magma compositions for four CLF picrites and a CLF basalt using the PRIMELT2 software of Herzberg and Asimow (2008), which determines a primary melt composition for a given sample by incrementally adding and removing equilibrium olivine. The primary magmas calculated by Hastie and Kerr (2010) have relatively high MgO contents of ~20-22 wt%. The parental magma compositions

used in this study were estimated by rescaling the major element compositions of these primary magmas to an Mg number of ~73 (approximately in equilibrium with upper mantle olivine, Fo_{92}). It should be noted that the CLF picrites examined in these thesis in this study are olivine cumulates (Kerr *et al*., 1999). These samples are significantly more Mg-rich than the chosen parental magma, and thus cannot be described by the modeled crystallization trends below.

The water contents of the end member magmas shown in Table 5.1 were constrained by modeling liquid lines of descent for parental magmas at a range of water contents. A subset of these (0 to 2 wt% water at a pressure of 1 kbar) are shown in Figure 5.1. The downward inflection in the liquid line of descent on the Al_2O_3 diagram (at about 9% MgO for the trend with 0 wt% water) indicates the onset of plagioclase crystallization. The shift of this inflection point to lower MgO values with increasing water content is consistent with the suppression of plagioclase crystallization under increasingly hydrous conditions. The downward inflection on the CaO diagram at about 10-11 wt% MgO indicates the onset of clinopyroxene crystallization. Trends on the Al_2O_3 and CaO diagrams suggest that the parental magma of the CLF samples and the majority of the BR samples was relatively dry, while the parental magma of the DF samples may require a higher water content (up to ~1 wt%). Although variations in water content alone can account for the majority of compositions on the Al_2O_3 and FeO* diagrams, it cannot reproduce many of the compositions on the CaO diagram.

The effects of varying pressure on fractional crystallization were also evaluated. Modelled liquid lines of descent for dry parental magmas at pressures of 0.5 to 4 kbar are shown in Figure 5.2. Trends on the Al_2O_3 and CaO diagrams demonstrate that increasing

pressure tends to suppress plagioclase crystallization and stabilize clinopyroxene crystallization. The poor fit of the modeled liquid lines of descent to the DF compositions on the Al_2O_3 and to samples from the DF, CLF and BR on the FeO* diagram suggest that fractional crystallization of a dry parental magma at relatively high pressures cannot produce the majority of compositions observed for the three localities.

Additional MELTS models were run in order to further constrain differences in the pressure of crystallization and magmatic water content of samples within each locality. Modelled liquid lines of descent for parental magmas with 0.25 wt% water at 0.25 to 1.5 kbar and 1 wt% water at 0.5 to 1.5 kbar are shown in Figures 5.3 and 5.4, respectively. These diagrams demonstrate that the majority of the CLF and BR compositions can be reproduced by crystallization of a relatively dry parental magma at a relatively high pressure, while the majority of the DF compositions can be reproduced by crystallization of a relatively wet parental magma at relatively low pressures. This is further illustrated in Figure 5.5, which shows that nearly the full range of compositions from all three localities can be bracketed by the two end-member parental magma compositions from Table 5.1—a dry magma crystallizing at 2.5 kbar and a magma with 1 wt% water crystallizing at 1 kbar. The modeling thus indicates that the majority of compositions for lavas from the BR, CLF, and DF can be reproduced by crystallization of parental magmas of similar major element composition (though varying water contents) at relatively shallow depths in the crust. The implications of these results are discussed later in this thesis.

5.2 Constraints on Source Composition and Melting

Processes occurring in the upper mantle portion of the CLIP magma transport system set a compositional baseline (i.e. primary mantle melts) that is later modified during transport and storage in the crust. Understanding these processes is thus important for characterizing the petrogenesis of the CLIP. In particular, it is important to constrain both the composition of the mantle source and the melting conditions involved in generating primary magmas from said source. This can be accomplished by using concentrations of REEs and other trace elements in the rocks that form from the magmas that reach the surface. Figure 5.6 shows bivariate plots of selected moderately to highly incompatible trace elements for CLF, DF, and BR samples grouped by age. These elements tend to be preferentially partitioned into the melt phase during partial melting, and thus variations in these ratios can be attributed to variations in degree of melting (for ratios of elements with different incompatibilities) or in mantle source composition (for ratios of elements with similar incompatibilities). Figure 5.6 shows that samples from the three localities form two distinct trends on a subset of trace element diagrams (with trace elements normalized to concentrations in C1 chondrite after Sun and McDonough, 1989). The majority of the DF samples define a trend with La/Yb of ~2.6-3.7 and Dy/Yb of ~1.6-1.7, while the majority of the CLF and BR samples and a small subset of the DF samples define a trend with La/Yb of ~0.6-1.6 and Dy/Yb of ~1.0-1.3. However, despite the relatively large range in La/Yb (~0.6-3.7), samples from all three localities have a relatively restricted range of Nb/Zr (~0.8-1.4). This discrepancy suggests that although it is possible that samples from all three localities are derived from a mantle source of similar composition (as suggested by Nb/Zr), differences in degree of melting are

required in order to produce the different trends observed on the La/Yb and Dy/Yb diagrams. Figure 5.6 also demonstrates that, aside from the slight tendency of younger samples to belong to the lower La/Yb trend, there is little variation in La/Yb and Nb/Zr with age. This suggests limited variation in the mantle source composition and degree of melting within each locality over the age range of the CLIP, consistent with the observations of Loewen *et al*. (2013).

Variations in the mantle source composition and melting conditions of the CLIP can also be characterized using rare earth and multi-element diagrams for the CLF, DF and BR (Figures 15 and 16). As demonstrated by Figure 5.7, REE patterns for CLF samples are flat to slightly light REE-depleted. Samples from the DF generally exhibit light REE-enrichment, while samples from the BR are predominately flat to slightly depleted in light REEs. REE patterns from all three localities exhibit some variation, but this variation shows no clear relationship with age. This is consistent with limited variation in mantle source composition and melting conditions within each locality over the emplacement history of the CLIP.

Trace element and isotopic compositions can also be used to determine whether or not the petrogenesis of the CLIP can be attributed to a mantle plume. The likelihood that the CLIP was derived from a mantle plume can be investigated using a plot of Nb/Y vs. Zr/Y (originally devised by Fitton *et al*. (1997) for Iceland and the North Atlantic), an example of which is shown in Figure 5.9. The majority of samples from all three localities plot within the lines on this diagram. This suggests that, despite the large age range of the CLIP samples, their trace element chemistry is not inconsistent with a plume-related source. Additionally, as shown by Figure 5.10, the initial Nd and Sr

isotopic compositions of samples from the DF and CLF overlap the range of compositions reported for samples from the Galápagos Islands by White *et al.* (1993) and are distinct from Pacific MORB. As previously noted by Hauff *et al*. (2000a) and Kerr *et al*. (1996), much of the variation in Sr isotopic composition observed in the samples can likely be attributed to assimilation of altered oceanic crust or seawater alteration. Nevertheless, the isotopic similarity between samples from the CLIP and Galápagos Islands provides evidence that the Galápagos plume contributed materially to the petrogenesis of the CLIP. However, as noted by Loewen *et al*. (2013), a mantle plume model for the petrogenesis of the CLIP also requires a mechanism capable of producing the limited variation in geochemistry observed for CLIP samples despite ~30 m.y. of repeated melting. A potential mechanism that satisfies these criteria is discussed in more detail below.

5.3 Mantle Source Composition

In order to further constrain the temporal and spatial variations in mantle source composition and melting regime for the CLIP, a non-modal batch melting model (after Shaw, 1970) was used. The model calculates concentrations of selected trace elements present in a liquid derived from a given percent of partial melt of a specified mantle source. Tables 5.2 and 5.3 summarize the mantle source composition end members, mantle source mineralogy, melting modes and crystal-liquid partition coefficients used in the model. The depleted source used in the model is modified after Johnson *et al*. (1990), Wood *et al*. (1979), Le Roex (1987), and Donnelly *et al*. (2004). The enriched source used in the model was generated by mixing a depleted mantle source in Table 5.2 with

~2% of a liquid composition produced by ~0.1% partial melting of the depleted source, and is thus analogous to metasomatized mantle. The amount of partial melting and mixing involved in the generation of this enriched source were chosen such that trends for liquids produced by batch melting of this enriched source intersect the compositions of samples from CLIP localities over a similar range of degrees of partial melting on multiple trace element ratio plots (e.g. Figure 5.11). It should be noted that the trace element ratios of this source are similar to those of the enriched mantle source of Donnelly *et al*. (2004). Figure 5.11 shows the composition of liquids produced by batch melting of an enriched and depleted garnet spinel lherzolite source compared with the compositions of samples from the CLF, BR, and DF. As demonstrated by these figures, melting trends for a depleted source alone cannot reproduce the majority of the compositional range of samples from the CLIP, necessitating a contribution from a more enriched source. The figures also demonstrate that nearly the full range of samples from the three localities can be reproduced by mixing liquids generated by melting these enriched and depleted end members. The majority of samples from the DF can be reproduced by mixing liquids produced by ~5-10% batch melting of these enriched and depleted sources, while samples from the CLF and BR and a small subset of samples from the DF can be reproduced by mixing liquids produced by ~15-30% melting. These estimated values for degree of melting overlap, but also differ somewhat from previous models. The trace element model of Sen *et al*. (1998) suggested that samples from the DF could be reproduced by ~10-25% melting of an enriched and depleted source, while the model of Révillon *et al*. (2000) suggested that compositions of samples from the BR can be reproduced by ~10-15% melting. It should be noted, however, that these models

exhibit some important limitations. The model of Sen *et al*. (1988) estimated degree of melting using only La and Yb, while the model of Révillon *et al*. (2000) was based on only four samples. The model presented in this research predicts concordant melting trends for a large number of samples from three CLIP localities using multiple trace element ratios. These consistent results provide evidence that the model can effectively approximate the melting conditions and mantle source compositions for the CLIP.

The feasibility of this model is also supported by the fact that the melting trends it predicts can be used to reproduce the REE patterns for the CLF, BR, and DF. Figure 5.12 compares REE patterns of sample from the three localities to those of liquids generated by a liquids produced by various degrees of melting of hybrid enriched and depleted sources, followed by varying degrees of fractional crystallization. The REE patterns of CLF and BR samples can be reproduced by ~1-52% fractional crystallization, while the majority of DF samples can be reproduced by ~13-55% fractional crystallization. These values are similar to those estimated for DF samples by Sen *et al*. (1988), and are consistent with the major element chemistry of the samples examined in this thesis.

These models thus demonstrate that the trace element compositions of the CLF, BR, and DF samples can be generated by mixing liquids produced by various degrees of melting of enriched and depleted garnet spinel lherzolite sources followed by fractional crystallization. The model provides evidence for spatial variation in degree of melting across the CLIP, and indicates that the compositions of the CLF and BR samples may be consistent with a slightly greater contribution from depleted source material than samples from the DF. However, neither mantle source composition or degree of melting exhibit a clear relationship with age.

Although the results of the trace element modeling indicates the involvement of an enriched source in the petrogenesis of the CLIP, the isotopic evidence suggests a more nuanced interpretation. As shown by Figure 5.13, values for age-corrected ε_{Nd} for samples range from ~5.1 to 9.4. This suggests a mantle source that is depleted relative to the Chondritic Uniform Reservoir (CHUR), but distinct from depleted MORB mantle and similar to the Gálapagos plume. There are several potential explanations for an isotopically depleted, yet trace element-enriched source. It is possible that the isotopic signature associated with liquids derived from an enriched source has been obscured through mixing with more isotopically depleted liquids. However, a more likely explanation is that the enriched trace element signature indicated by the modeling was generated by metasomatism of a more depleted source. Fluids produced by decompression melting associated with the Gálapagos plume provide a potential mechanism for such metasomatism. If the melting event that generated this enriched source occurred relatively recently (i.e. during the initiation of the Gálapagos plume at ~90 Ma), then said source may not necessarily exhibit an ε_{Nd} value significantly lower than that of depleted mantle. Thus, a mantle source with a relatively enriched trace element composition and a relatively depleted isotopic composition is not unreasonable. In order to provide temporal constraints on the origin of the mantle source(s) suggested by these Nd isotopic compositions, a depleted mantle extraction age was calculated for the CLIP samples. Values of $^{147}Sm/^{144}Nd = 0.222$ and $^{143}Nd/^{144}Nd = 0.513144$ were used for the modern depleted mantle (after Michard *et al*., 1985). These calculations suggest that the source material for the CLIP could have been extracted from the upper mantle at ~400 to 2000 Ma. This range of extraction ages suggests that the mantle sources of the

CLIP may have arose from a history of distinct melting events occurring within a largely depleted mantle reservoir, resulting in a heterogeneous (though isotopically depleted) source. If this source was affected by metasomatism at some point after this age range (e.g. during the initiation of the Galápagos hotspot at ~95-100 Ma), then the source could become enriched in trace elements while maintaining an isotopically depleted signature.

The lack of a strong age-related trend in mantle source composition is also supported by Nd isotopic compositions of samples from the three localities. Although a range of initial Nd isotopic compositions is observed, there is considerable overlap between samples from different age groups. However, there are slight differences in Nd isotopic composition between the different localities. Samples from the BR tend to have higher age-corrected ε_{Nd} (~8-10) than samples from the CLF and DF (~5-7). This suggests that the latter may be tapping slightly more long-term enriched source material than the former. These variations provide further evidence that the mantle source of the CLIP is heterogeneous across a length scale of ~10^2 to 10^3 km, and can be attributed to varying contributions from enriched and depleted source material.

The isotopic signature of the mantle source for the CLIP bears similarities to sources proposed for other oceanic plateaus, but also differs in several key respects. Mahoney *et al.* (1993) found that the source for the Ontong Java Plateau (OJP) exhibits age-corrected ε_{Nd} ranging from +4.0 to +6.3. This overlaps the range of Nd isotopic compositions for the CLIP, but suggests that the source of the OJP is more isotopically enriched than that of the CLIP. Additionally, the more narrow range of ε_{Nd} implies either that the source of the CLIP is more heterogeneous than that of the OJP or that the magma transport system of the OJP allows for more complete homogenization of distinct mantle

signatures (i.e. through melt aggregation and mixing). In contrast, the Kerguelen Plateau exhibits ε_{Nd} ranging from ~-5 to +5 (Weis *et al*., 1993; Neal *et al.*, 2002; Frey *et al.*, 2002). Much of the more enriched end of this range can be attributed to the influence of continental lithosphere (Neal *et al.*, 2002; Frey *et al.*, 2002). However, Neal *et al.* (2002) suggested that both isotopic and trace element evidence indicate a primitive mantle (i.e. ε_{Nd} of ~0) source played a role in the petrogenesis of the LIP. This shows a clear contrast to the mantle source proposed for the CLIP, which exhibits both isotopic depletion and a combination of trace element-enrichment and depletion. The differences in mantle source for CLIP compared with other oceanic plateaus implies a difference in the processes that led to the generation of these sources, further illustrating that a single, overarching petrogenetic model is likely an inappropriate approach to describing the formation of LIPs.

5.4 Model for CLIP Formation

The seemingly paradoxical observation that samples from the CLF, BR, and DF exhibit limited trace element variation despite spanning an age range of ~30 m.y. was previously noted by Loewen *et al*. (2013). These authors suggested that the complex tectonic history of the CLIP provides a possible mechanism for generating the invariant trace element chemistry of samples from the three localities over multiple melting episodes. The model developed by Loewen *et al*. (2013) utilizes the interactions between plumes and subduction zones through mantle flow to explain the origin of the CLIP (Figure 5.14). As noted by Richards and Griffiths (1988), mantle flow can result in the horizontal displacement of mantle plumes. Thus, following the polarity reversal of the subduction zone associated with the Greater Antilles Arc at ~80-90 Ma as a result of its

collision with the Caribbean plateau, mantle flow associated with subduction at the now southwest-dipping trench would be expected to result in an eastward deflection of the head of the plume that formed the CLIP. Mantle dynamic models (e.g. Druken *et al*., 2012; Long *et al*., 2012) indicate that subsequent slab rollback to the east would be expected to enhance this motion by generating a relatively strong counterflow in the asthenosphere. The combination of the eastward flow with the asthenosphere counterflow initiated by slab rollback could then result in extension of the initial thickened plateau lithosphere and continued upwelling of the residual plume head material beneath the Caribbean Plateau. The subsequent formation of the northeast-dipping Central America Arc by 60 Ma would then result in the separation of the plume head from the tail, causing the former to be essentially isolated beneath the CLIP. Northeast and southwest mantle flow generated by the subduction zone associated with the Central America Arc and the Greater Antilles Arc (respectively) would then effectively isolate the plume head material beneath the CLIP. Volcanism over the ~30 m.y. age range of the CLIP could thus repeatedly tap this mantle source material.

The results of the batch melting modeling presented here are broadly consistent with the model of Loewen *et al*. (2013). According to the mantle plume model of Campbell and Griffiths (1990), the starting heads of mantle plumes entrain material from the surrounding mantle during ascent. Under this model, depleted material from the upper mantle could be incorporated into the more enriched plume head during its initial ascent. The lateral displacement of plume head material through the depleted upper mantle beneath the CLIP due to asthenospheric flow associated with nearby subduction zones could promote additional mixing between of depleted upper mantle material and more

enriched, metasomatized plume material (Figure 5.15). This mechanism would further explain the hybrid enriched and depleted mantle sources indicated by the geochemical data.

The spatial variation in degree of melting across the CLIP indicated by the batch melting models can be described by the conceptual model shown in Figure 5.15. The results of the modeling suggest that the CLF and BR samples exhibit a greater degree of melting (~15-30%) than the majority of the DF samples (~5-10% melting). This would be consistent with the hotter plume head being approximately centered beneath the CLF and thinning outward toward the DF. Under this conceptual model, the greater extent of melting observed for CLF and BR samples results from the fact that anomalously hot (relative to the ambient mantle) plume head material extends to a greater depth in this area than at the DF, resulting in a deeper melt column. Although the CLF is currently located at the southern margin of the modern Caribbean plate, this conceptual model does not necessarily require an asymmetric plume head. As previously stated, tectonic models for the CLIP suggest that much of the southern portion of the oceanic plateau have been accreted along the western coast of South America. Additionally, seismic imaging by Miller et al. (2009) shows a cold slab beneath the Maracaibo block of northern South America, which the authors interpreted as the southernmost portion of the CLIP. It is thus possible that the CLF was located near the center of the original Caribbean Plateau. The conceptual model presented here is broadly consistent with the spatial variation in geochemistry observed along the CLF-BR-DF transect and compatible with the model used by Loewen *et al*. (2013) to explain the lack of temporal variation in geochemistry across the CLIP.

5.5 CLIP Magma Transport System

The results of the major and trace element modeling provide constraints on the nature of the magma transport system of the CLIP. The shallow depths of crystallization indicated by the MELTS modeling suggest that the lavas and intrusives examined in this study represent only the uppermost portion of the magmatic plumbing system of the CLIP. This interpretation is consistent with the structure of the CLIP as inferred by Kerr *et al*. (1998) from obducted terranes in the Caribbean and western Colombia. These authors conclude that the uppermost portion of the CLIP is composed of relatively homogenous pillow basalts, dolerite sills, and gabbro stocks, with a lower crustal sequence composed of komatiites, picrites, and trace element-enriched and -depleted basalts. Kerr *et al*. (1998) explain this structure using a model in which, during the initial stages of LIP formation, magma chambers are poorly developed due to the relatively thin lithosphere. This allows relatively primitive, highly magnesian melts to ascend through the lithosphere and erupt as komatiites and picrites. Continued development of the LIP results in both lithospheric thickening and an increase in the number and size of magma chambers. This increases the likelihood that high-MgO magmas produced in the mantle source region will stall during ascent and experience homogenization and fractional crystallization in these crustal magma chambers. These factors lead to the predominance of more evolved basalts with relatively homogenous trace element signatures in the uppermost portion of the LIP.

Although picrites are present in the CLF and DF and highly enriched basalts have been identified at the BR, the relative scarcity of these compositions and the notable lack of komatiites suggest that the lower portions of the CLIP have not been significantly

exposed in these areas. Thus, although MELTS modeling using lavas and intrusives from these localities can be used to characterize the magmatic conditions in the uppermost section of the CLIP, it likely provides fewer constraints on processes occurring in the lower crust. The fact that the two end member parental magmas used in the MELTS model have similar major element compositions, however, is consistent with the idea that the CLIP is fed by a magma transport system characterized by a large number of crustal magma chambers dominated by vigorous mixing (and subsequently, homogenization of distinct geochemical signatures). Recall that the results of the trace element modeling imply a gradient in degree of melting from the CLF (plume center) to the DF (plume margin). The lack of variation in the major element compositions of parental magmas across the horizontal extent of the plume suggests that the primary mantle melts in these areas are efficiently homogenized by magma mixing in crustal magma chambers prior to experiencing fractional crystallization at relatively shallow depths.

The MELTS modeling results also suggest that as much as 1 wt% water is needed in order to explain the formation of a subset of the CLIP samples. The involvement of magmas with comparable water contents in the petrogenesis of LIP basalts has been documented by previous research. Tholeiitic basalts from Hawaii contain up to 0.9 wt% water (Dixon *et al*. 1991; Johnson *et al*. 1994). Water contents of as much as 1.5% wt% have been identified in mid-ocean ridge basalt in close proximity to a mantle plume (Dixon *et al*. 2002). Basaltic glasses from the Kerguelen Plateau exhibit water contents of up to 0.7 wt%, while more alkalic basalts from the same LIP contain inclusions with up to 2 wt% water (Wallace, 2002; Borisova *et al*. 2002). Thus, although the maximum

water contents proposed for the CLIP parental magmas are relatively high, they are not unprecedented.

While the MELTS modeling presented in this research provides constraints primarily on the upper crustal portion of the magma transport system of the CLIP, the results of the trace element modeling allow for a characterization of the upper mantle portion of the plateau's plumbing system. As previously discussed, batch melting of variably depleted and enriched mantle source material can not only reproduce the majority of trace element compositions of CLF, BR, and DF samples, but is also compatible with the range of Nd isotopic compositions observed for these rocks. The results of this modeling could be interpreted to indicate that true equilibrium melting is responsible for generating the parental magmas of the CLIP, but a more likely explanation is that these magmas are formed as a result of pooling of fractional melts from a range of mantle source compositions. As previously noted by Révillon *et al*. (2000) and others, the two processes produce similar trace element signatures. Additionally, as noted by Sparks (1992), batches of melt in the mantle are mobile and capable of mingling at degrees of melting as low as 1%. Thus, given the ~5-30% partial melting implicated for the formation of the CLIP by the trace element modeling, pooling of fractional melts is a more realistic mechanism for generating the parental magmas of the CLIP.

The proposed structure of the magma transport system for the CLIP differs somewhat from those found in terrestrial flood basalts. A striking example is the flood basalts of the West Greenland Basin. Larsen and Pedersen (2000) described the magma transport system of this LIP as a complex system of steep, dike-like conduits within the

lithospheric mantle and crust. The authors suggested that melting occurs beneath an approximately 100 km thick lithospheric lid, and that melt batches travelling through these conduit systems experienced variable degrees of crystallization, magma mixing and oxidation. The proposed conduit system is essentially devoid of sills and similar density filters. In contrast, the numerous doleritic sills and gabbro plutons of the CLIP suggest a magma transport system with storage areas and density filters at multiple levels in the crust. Modeling by Larsen and Pedersen (2000) also suggests that the majority of crystallization at the West Greenland Basin flood basalts occurred from a depth of 45 km up to the surface. This implies crystallization at significantly greater depths than suggested by the MELTS modeling of CLIP lavas and intrusives in this thesis. However, as previously mentioned, the apparently shallow crustal nature of the CLIP magma transport system indicated by this modeling may be due in part to limited ability to sample the lower portions of the CLIP magma transport system in the CLF, BR, and DF. Nevertheless, the fact that the MELTS modeling here utilizes a relatively large number of both lavas and intrusives from all three localities implies that a significant portion of fractional crystallization at the CLIP must occur at relatively shallow depths in the crust.

As previously discussed, the results of the trace element modeling suggest that the relatively homogenous REE compositions of CLIP samples can be attributed to the pooling and aggregation of variably enriched and depleted liquids en route to the earth's surface. However, the depth range over which this aggregation occurs is unclear. Under the model proposed by Larsen and Pedersen (2000) for the West Greenland flood basalts, mixing between mantle melts occurs within conduits extending from the within the upper mantle through ~100 km of the lithosphere. Kent *et al*. (2002), however, found that the

magma transport system associated with the Oligiocene continental flood basalts in Yemen CFB were capable of channeling compositionally distinct batches of melt through the lithospheric mantle with only limited mixing. The authors concluded that the majority of magma mixing and aggregation occurred in crustal magma chambers. It is unclear which of these two models best fits the CLIP. The magma transport system of the CLIP appears to be composed of numerous shallow crustal magma chambers, but the possibility that melts experience significant mixing prior to reaching these chambers cannot be ruled out. Although the work in this thesis provides constraints on the upper crustal and upper mantle portions of the CLIP magma transport system, additional research is needed to further characterize the processes occurring within the lower crust.

Table 5.1. End member parental magmas used in MELTS modeling. Major element compositions are modified after the CLF parental magmas of Hastie and Kerr (2010).

Oxide (wt%)	A	B
SiO_2	47.70	47.60
TiO_2	0.90	0.83
Cr_2O_3	0.23	0.24
Al_2O_3	11.54	11.40
FeO	8.99	8.83
Fe_2O_3	1.05	1.06
MgO	15.38	15.30
MnO	0.25	0.25
CaO	11.99	11.85
K_2O	0.30	0.24
Na_2O	1.55	1.45
P_2O_5	0.05	0.04
H_2O	0.00	1.00
Pressure (kbar)	2.5	1
fO_2	QFM-1	QFM-1

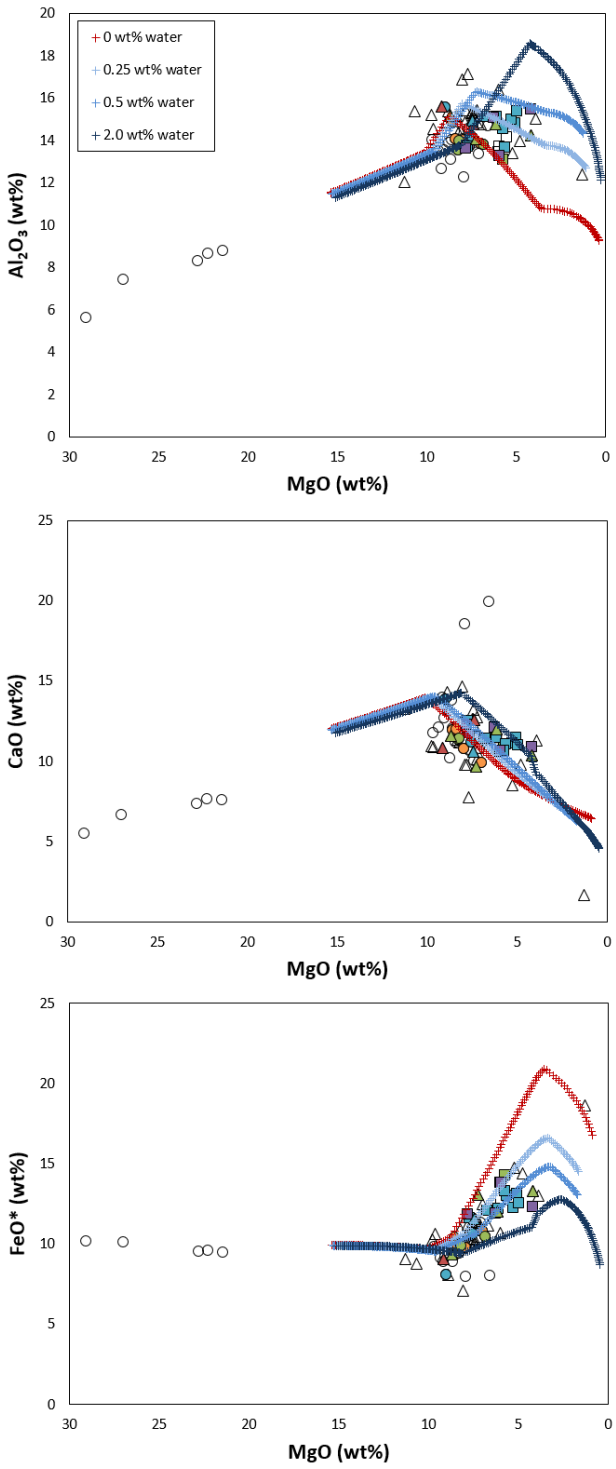

Figure 5.1. MELTS liquid lines of descent for parental magmas with water contents of 0 to 2 wt% water at 1 kbar, with oxygen fugacity buffered at QFM-1. Major element compositions of parental magmas are intermediate between those listed for Magmas A and B in Table 5.1. Symbols are as in Figure 4.1.

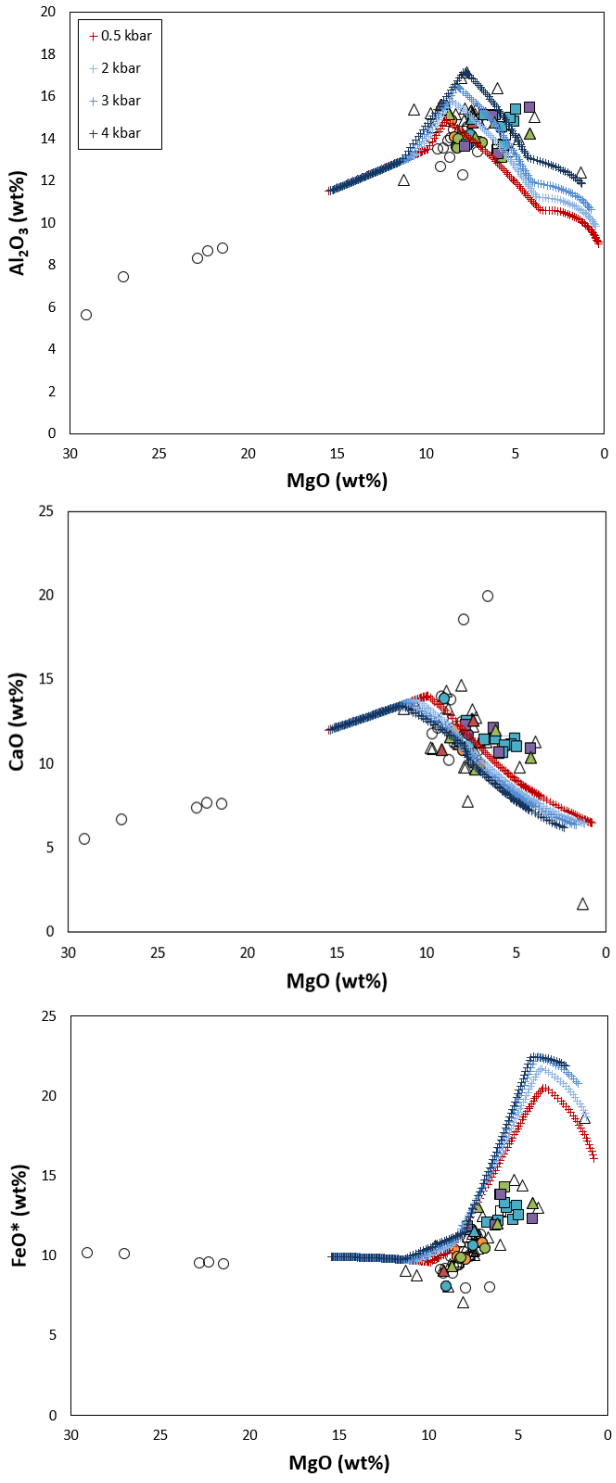

Figure 5.2. MELTS liquid lines of descent for dry parental magmas at pressures of 0.5 to 4 kbar, with oxygen fugacity buffered at QFM-1. Major element compositions of parental magmas are intermediate between those listed for Magmas A and B in Table 5.1. Symbols are as in Figure 4.1.

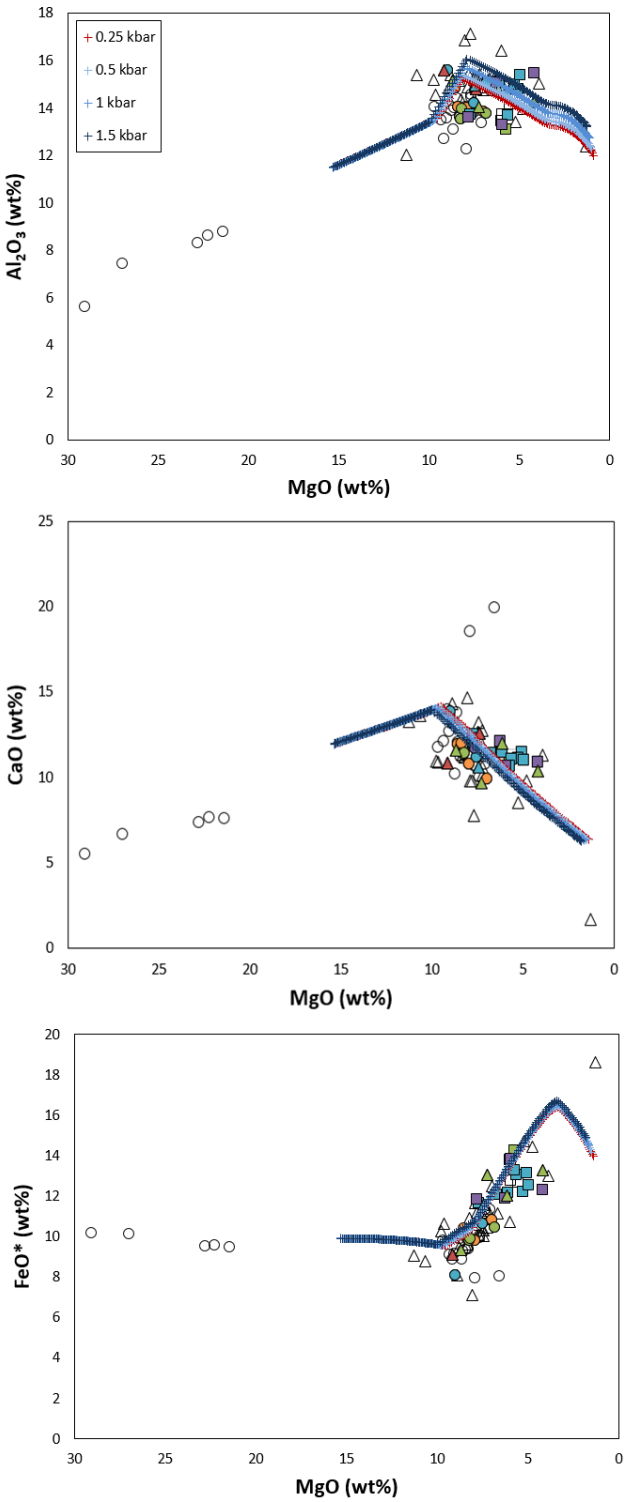

Figure 5.3. MELTS liquid lines of descent for parental magmas with 0.25 wt% water at pressures of 0.25 to 1.5 kbar, with oxygen fugacity buffered at QFM-1. Major element compositions of parental magmas are intermediate between those listed for Magmas A and B in Table 5.1. Symbols are as in Figure 4.1.

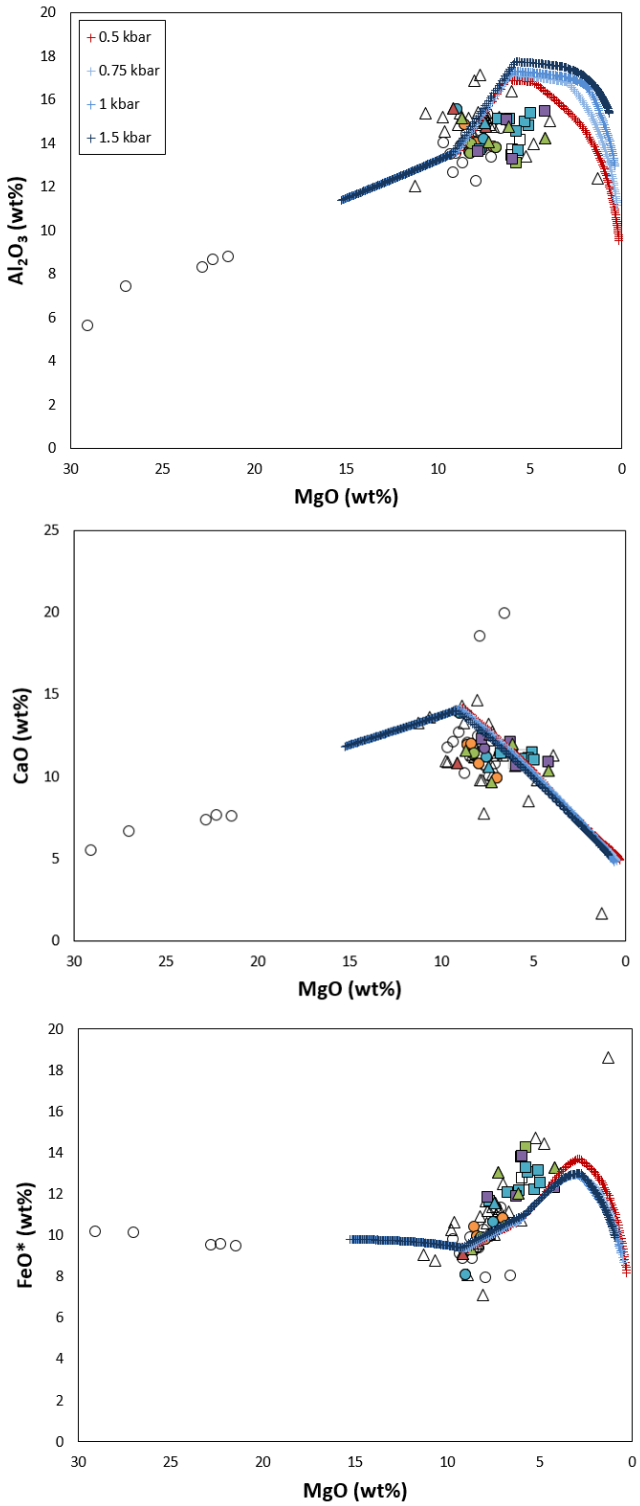

Figure 5.4. MELTS liquid lines of descent for parental magmas with 1 wt% water at pressures of 0.5 to 1.5 kbar, with oxygen fugacity buffered at QFM-1. Major element compositions of parental magmas are intermediate between those listed for Magmas A and B in Table 5.1. Symbols are as in Figure 4.1.

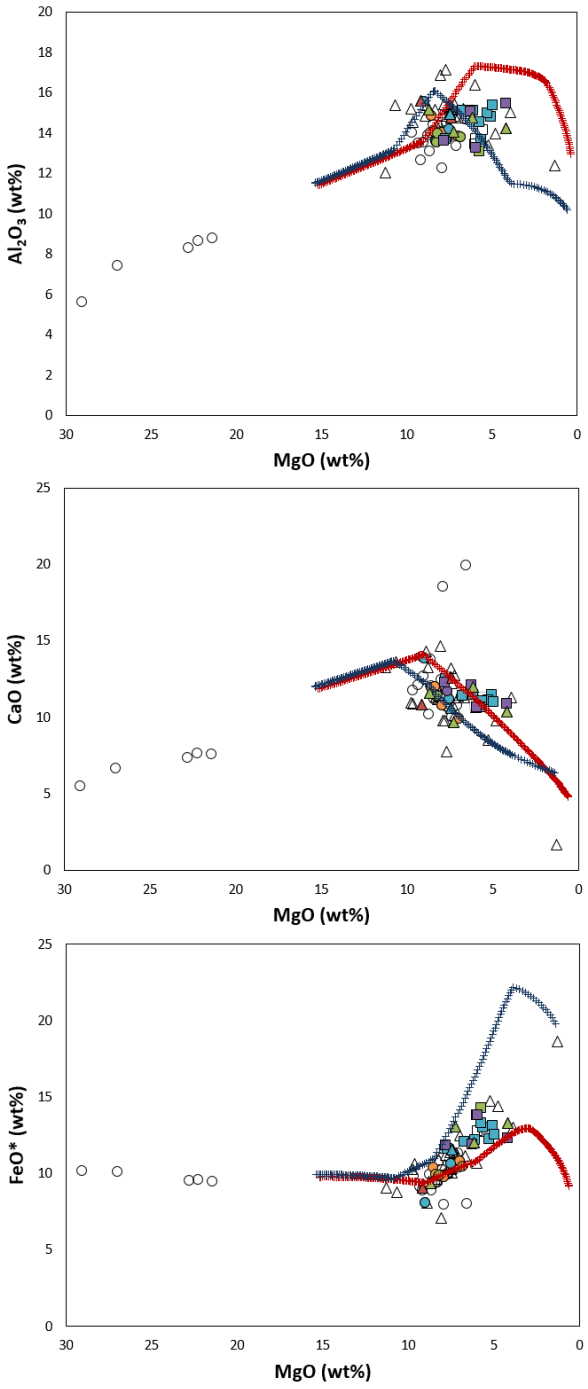

Figure 5.5. MELTS liquid lines of descent for parental magmas shown in Table 5.1 (blue trend is for Magma A, red trend is for Magma B). Symbols are as in Figure 4.1.

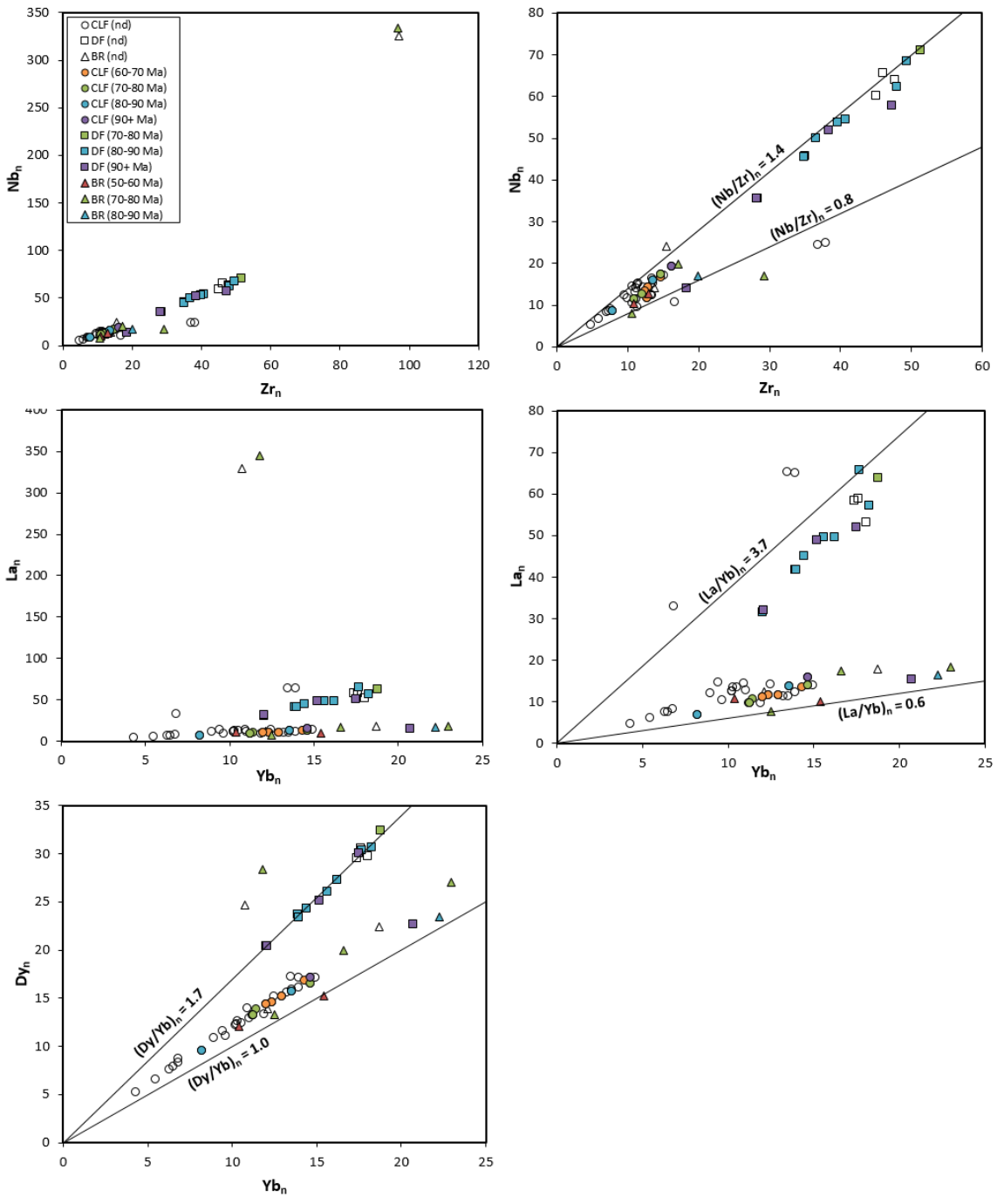

Figure 5.6. Bivariate trace element plots for the CLF, DF and BR. Horizontally adjacent plots show the same compositions, but use a different scale to better depict the variation in the majority of the samples. BR samples are previously described by Révillon *et al*. (2000). Ages are from Loewen *et al*. (2013). Elements are normalized to C1 chondrite (Sun and McDonough, 1989).

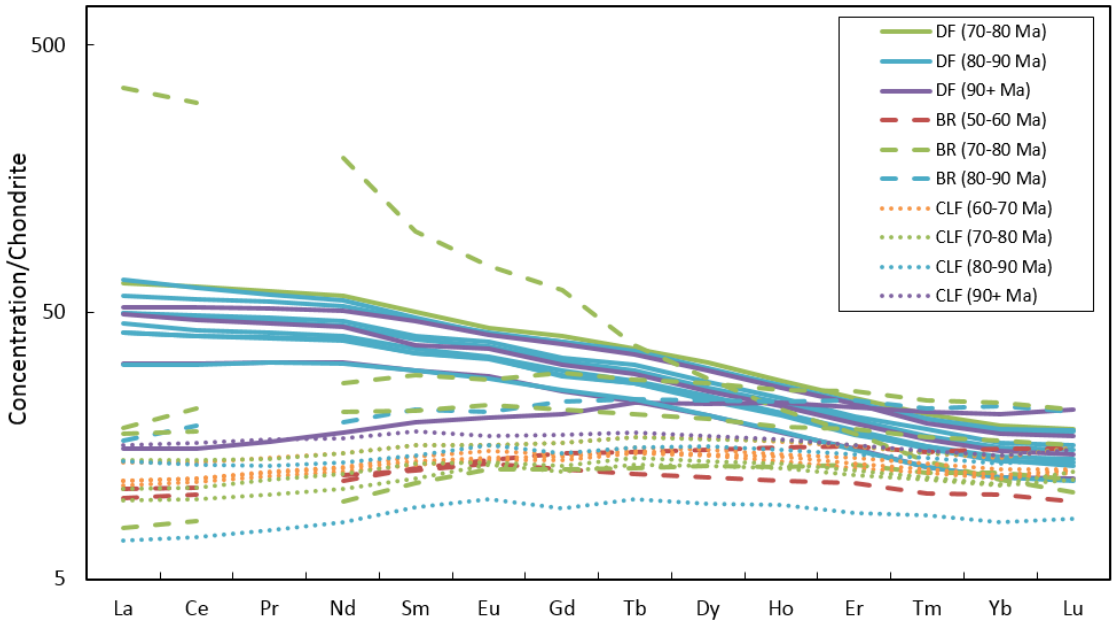

Figure 5.7. Rare earth element diagrams for DF, BR, and CLF samples of various ages. Elements are normalized to C1 chondrite (Sun and McDonough, 1989). BR samples are previously described by Révillon *et al*. (2000). Ages are from Loewen *et al*. (2013).

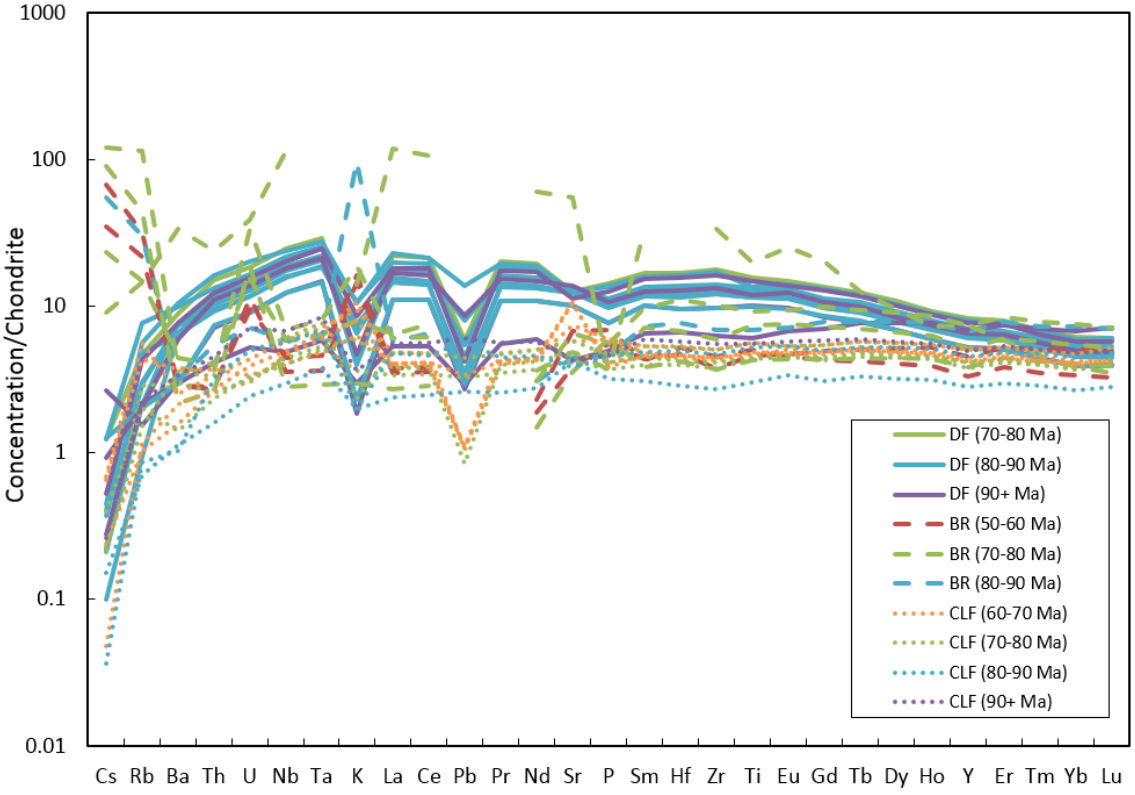

Figure 5.8. Multi-element diagrams for DF, BR, and CLF samples of various ages. Elements are normalized to C1 chondrite (Sun and McDonough, 1989). BR samples are previously described by Révillon *et al*. (2000). Ages are from Loewen *et al*. (2013).

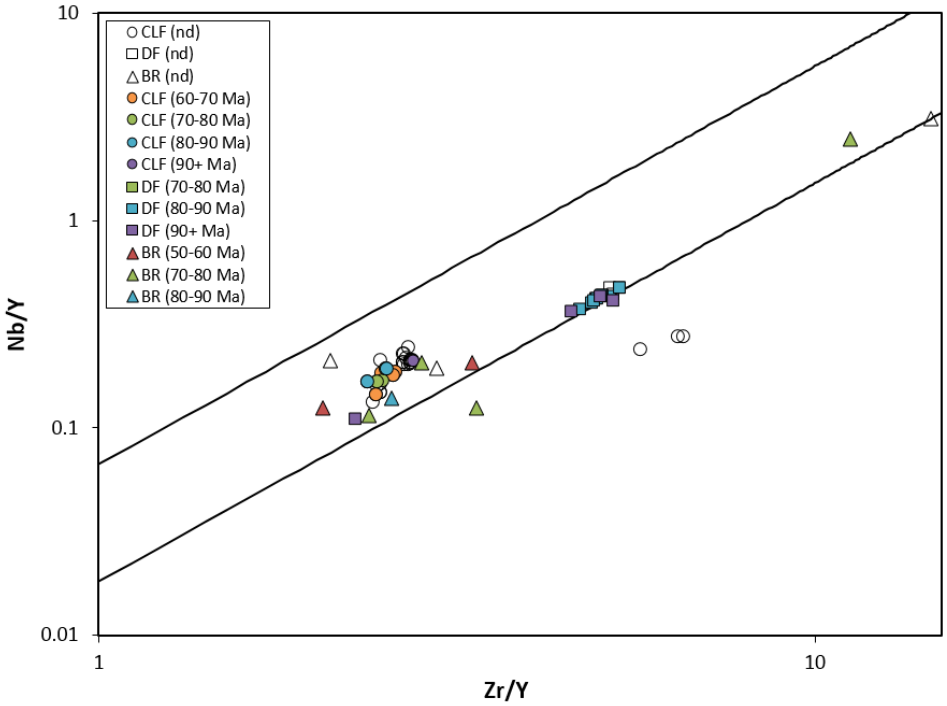

Figure 5.9. Nb/Y vs. Zr/Y plot of CLF, DF, and BR samples, after Fitton *et al*. (1997). Samples plotting between the black lines are consistent with a mantle plume source. BR samples are previously described by Révillon *et al*. (2000). Ages are from Loewen *et al*. (2013).

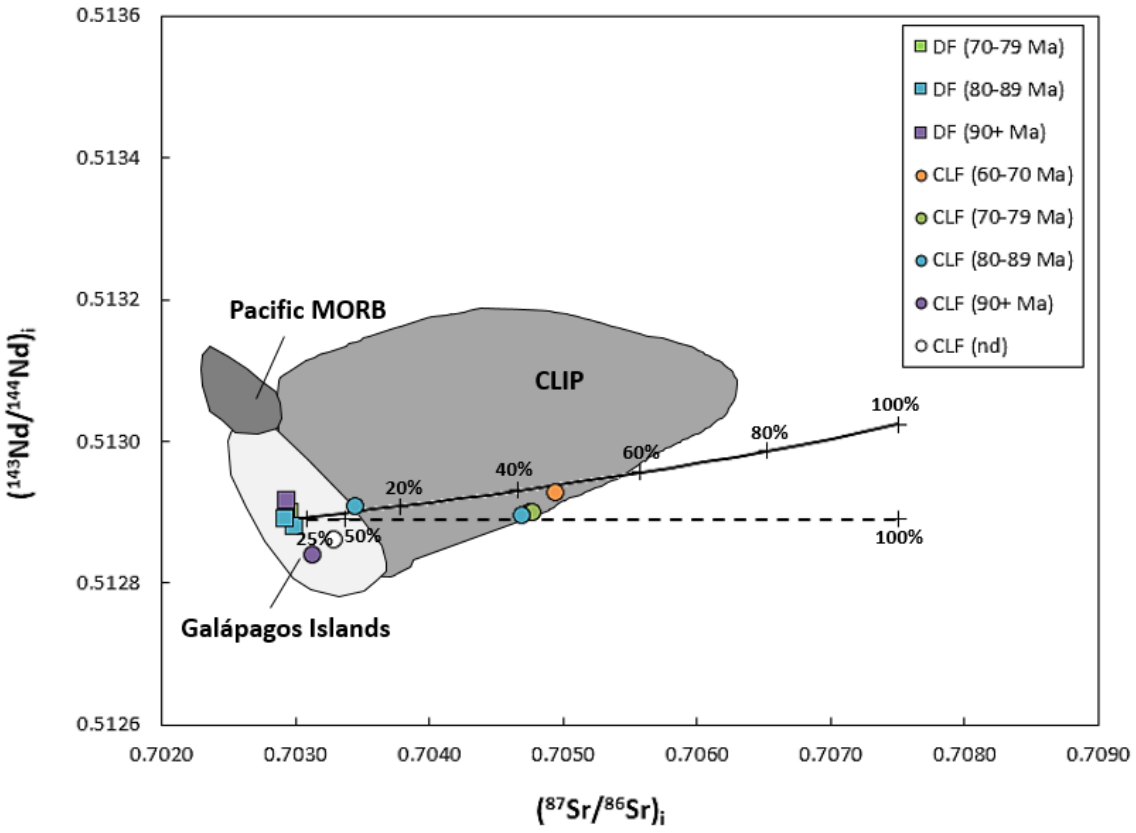

Figure 5.10. Initial Nd and Sr isotopic compositions of CLIP and Galápagos samples. DF compositions are from this study, CLF compositions are from A. Durkefalden (pers. communication). CLIP compositions after Hauff *et al*. (2000a), Hauff *et al*. (2000b), Sinton *et al*. (1997), Mamberti *et al*. (2004). Galápagos compositions are from White *et al*. (1993). Pacific MORB compositions are from Janney and Castillo (1997) and White *et al*. (1993). Mixing lines for altered oceanic crust (solid line) and seawater (dashed line) are shown. The altered oceanic crust composition used has $^{143}Nd/^{144}Nd = 0.513024$, [Nd] = 8 ppm, $^{87}Sr/^{86}Sr = 0.7075$, and [Sr] = 200 ppm (modified after Kerr *et al*. (1996). Seawater assimilation is assumed to have a negligible effect on the Nd isotopic composition of the CLIP samples. The seawater composition used has $^{87}Sr/^{86}Sr = 0.7075$ and [Sr] = 7.7 ppm (after Faure, 1986).

Table 5.2. Partition coefficients and mantle source compositions used in melting models. Sources of data: ol (olivine) after Kennedy *et al*. (1993) and McKenzie and O'Nions (1991), opx (orthopyroxene) after Kennedy *et al*. (1993) and Green *et al*. (2000), cpx (clinopyroxene) after Hart and Dunn (1993) and Green *et al*. (2000), sp (spinel) after Keleman *et al*. (1993), Jenner *et al*. (1993), McKenzie and O'Nions (1991), garnet (ga) after Green *et al*. (1989) and Green *et al*. (2000). Mantle source compositions are in ppm. Depleted mantle source (D Mantle) modified after Johnson *et al*. (1990), Wood *et al*. (1979), Le Roex (1987), and Donnelly *et al*. (2004). Enriched mantle source (E Mantle) calculated as described above.

	ol	opx	cpx	sp	ga	D Mantle	E mantle
La	3.10E-05	4.40E-05	5.36E-02	6.00E-04	1.00E-03	0.31	0.78
Ce	1.00E-04	1.40E-04	8.58E-02	6.00E-04	4.00E-03	0.95	2.09
Nd	4.20E-04	5.20E-04	1.87E-01	6.00E-04	5.70E-02	0.86	1.41
Sm	1.10E-03	1.60E-03	2.91E-01	6.00E-04	3.70E-01	0.32	0.43
Eu	7.50E-04	6.40E-04	3.50E-01	6.00E-04	1.00E+00	0.13	0.17
Gd	1.50E-03	3.40E-02	7.70E-01	1.00E-02	7.50E-01	0.494	0.57
Tb	1.50E-03	2.96E-02	6.10E-01	1.00E-02	1.50E+00	0.091	0.10
Dy	1.40E-03	8.40E-03	4.42E-01	1.50E-03	2.40E+00	0.635	0.70
Ho	1.60E-03	5.00E-03	2.50E-01	1.00E-02	3.70E+00	0.141	0.15
Er	1.30E-02	1.70E-02	3.87E-01	3.00E-03	4.40E+00	0.423	0.45
Yb	3.00E-02	3.30E-02	4.30E-01	4.50E-03	6.25E+00	0.425	0.44
Lu	1.50E-03	1.19E-01	5.80E-01	1.00E-02	6.85E+00	0.065	0.07
Nb	5.00E-05	1.40E-03	7.70E-03	1.00E-02	2.10E-02	0.28	1.37
Zr	5.80E-04	3.30E-03	1.23E-01	7.00E-02	7.89E-01	8.4	11.82
Y	9.40E-03	9.60E-03	4.67E-01	4.00E-03	3.57E+00	4.1	4.37

Table 5.3. Mantle source mineralogy and melting modes used in batch melting models (modified after Gurenko and Chaussidon, 1995).

Phase	Source Proportion	Melting Mode
ol	0.55	-0.1
opx	0.22	0.25
cpx	0.15	0.61
sp	0.04	0.04
ga	0.04	0.2

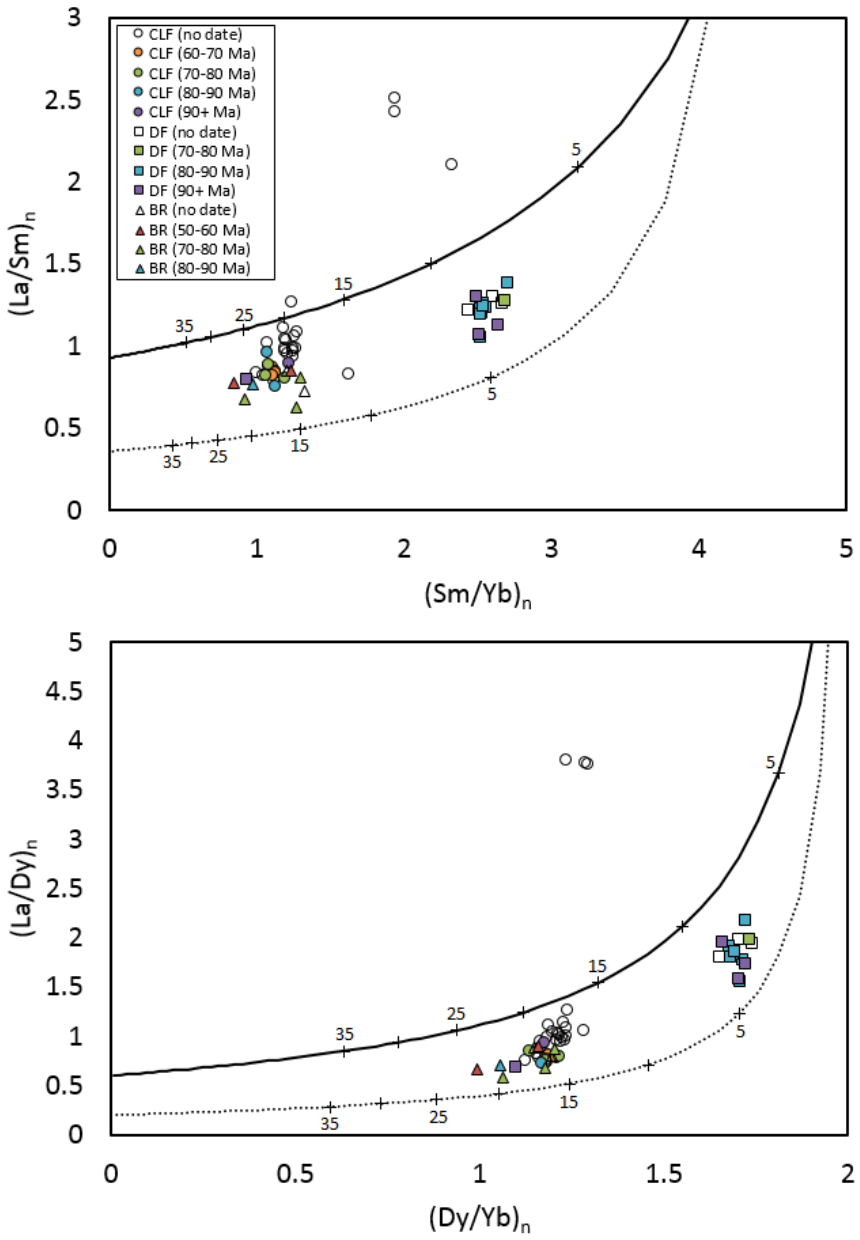

Figure 5.11. Batch melting models for CLF, DF, and BR samples. Trace element ratios are normalized to C1 chondrite (Sun and McDonough, 1989). Liquid trends produced by batch melting of a garnet spinel lherzolite source (after Gurenko and Chaussidon, 1995) with the depleted composition (*dotted line*) and enriched composition (*solid line*) shown in Table 5.2. Tick marks on each liquid trend are labeled with the corresponding degree of melting, with each tick mark representing an additional 5% melting.

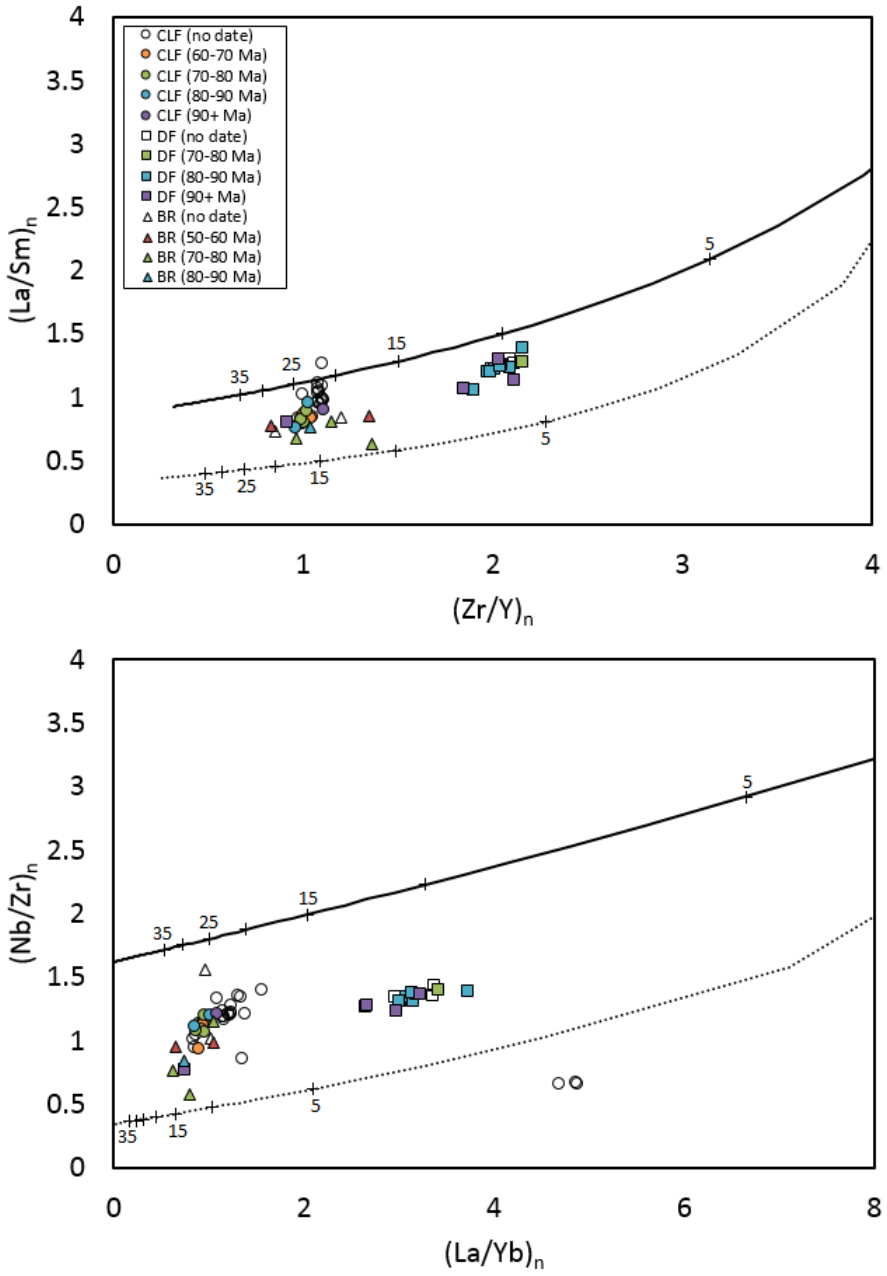

Figure 5.11 (Continued)

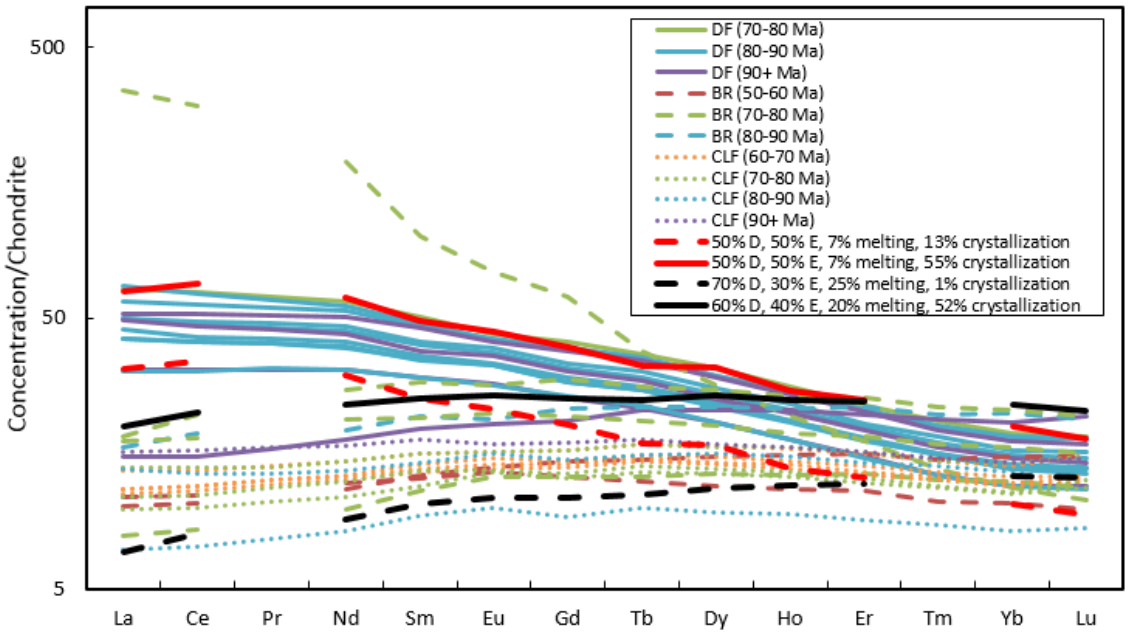

Figure 5.12. Comparison of modelled REE patterns to DF, BR, and CLF sample compositions. Trends are shown for 13% fractional crystallization of a liquid produced by 7% melting of a 50% enriched (E), 50% depleted (D) source, 55% fractional crystallization of a liquid produced by 7% melting of a 50% enriched, 50% depleted source, 1% fractional crystallization of a liquid produced by 25% melting of a 70% depleted, 30% enriched source and 52% fractional crystallization of a liquid produced by 20% melting of a 60% depleted, 40% enriched source.

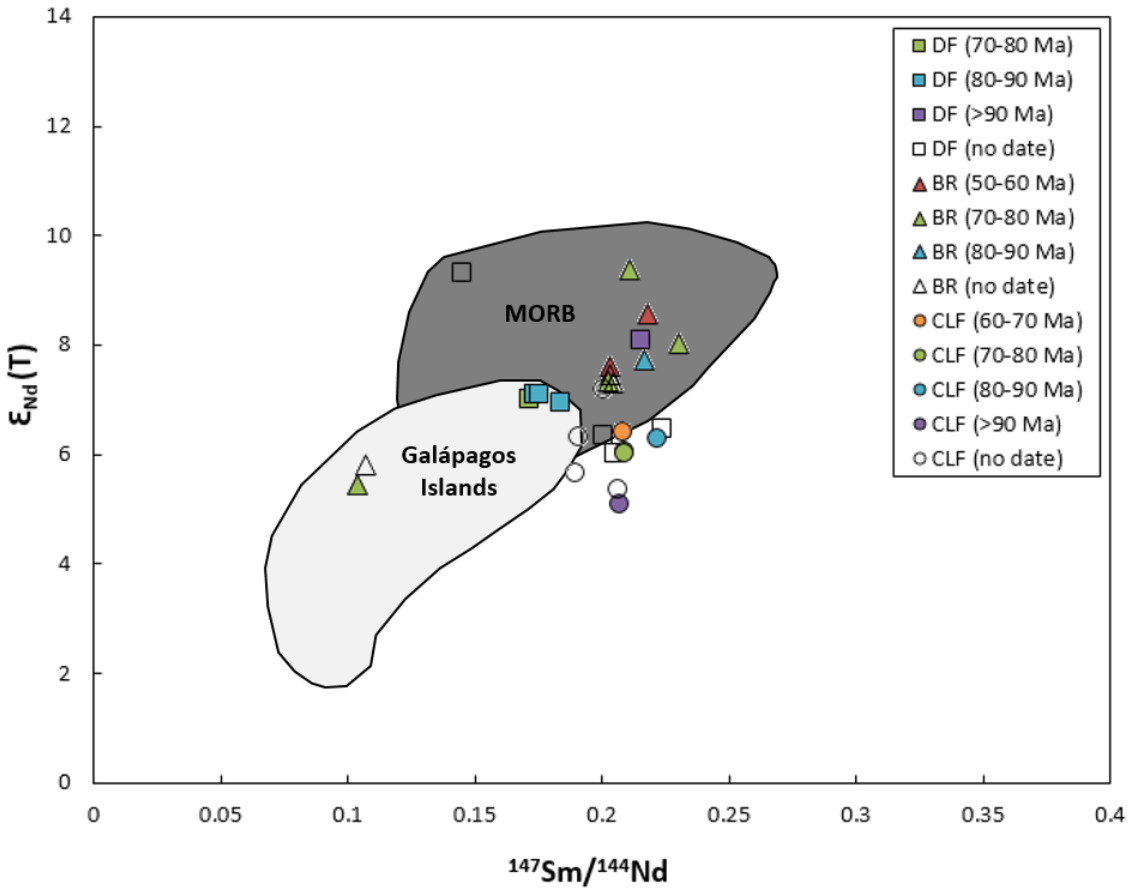

Figure 5.13. Age-corrected ε_{Nd} and $^{147}Sm/^{144}Nd$ compositions of BR, DF and CLF samples. DF compositions are from this study, CLF compositions are from A. Durkefalden (pers. communication) and Révillon *et al*. (1999), BR compositions are from Révillon *et al*. (2000). Galápagos Islands data are from White et al. (1993), MORB data are from Cohen and O'Nions (1982) and White et al. (1987).

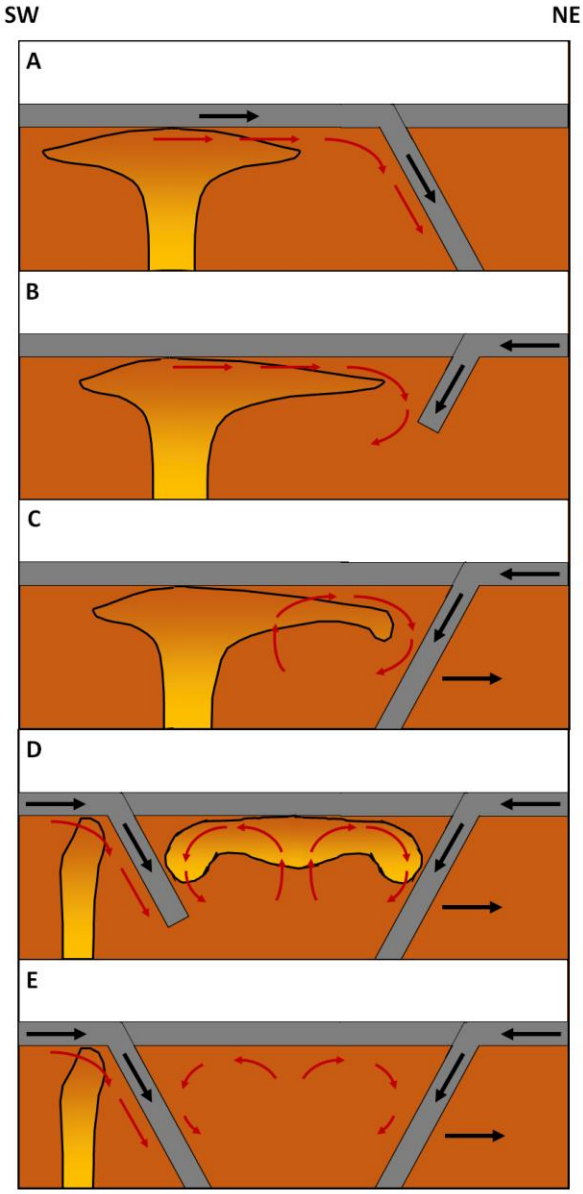

Figure 5.14. Conceptual model for the petrogenesis of the CLIP (modified after Loewen *et al*. (2013). Oceanic lithosphere is shown in gray, plume material is shown in yellow-orange, asthenospheric mantle is shown in dark orange. Black arrows show the movement of oceanic lithosphere, red arrows show asthenospheric mantle flow. A. 95-90 Ma: Galápagos plume head reaches base of oceanic lithosphere. B. 90-85 Ma: Collision of Caribbean Plateau with subduction zone beneath the Greater Antilles Arc results in a polarity flip. C. 85-70 Ma: Slab rollback results in the eastward movement of plume head material relative to the plume tail, which remains approximately fixed in the mantle reference frame. Upwelling results in continued volcanism. D. 70-60 Ma: Initiation of subduction to the SW of the CLIP separates plume head from plume tail. Plume tail initiates OIB volcanism, producing seamount trails. E. <50 Ma: Waning of CLIP volcanism.

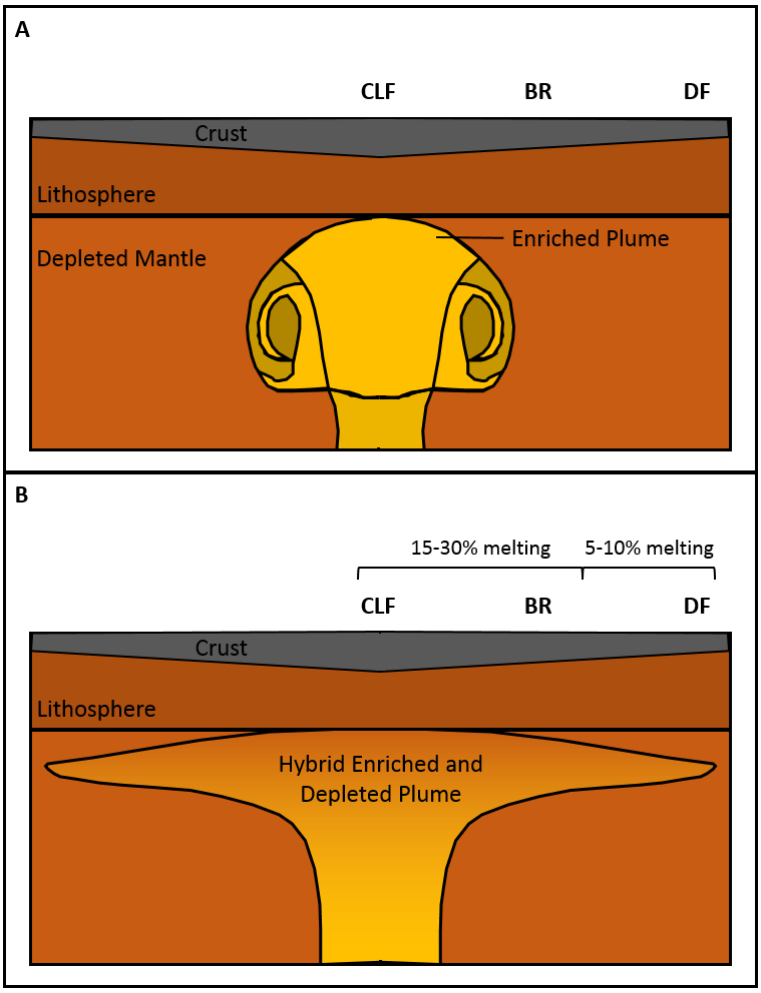

Figure 5.15. Conceptual model of Galápagos plume initiation. A. Entrainment of depleted upper mantle material (ε_{Nd} of +9 to +10) by ascending enriched plume material (ε_{Nd} of ~0) produces a hybrid enriched and depleted mantle source (ε_{Nd} of +5.1 to +9.4). B. Emplacement of plume results in melting regime in which partial melting is highest at the plume axis (beneath the CLF) and decreases toward the margins (beneath the DF). Metasomatism of the plume source at the time of emplacement results in additional trace element enrichment.

6 Conclusions:

The petrogenetic model presented in this research provides a synthesis of the geochronological and geochemical trends observed for samples from the CLIP. Results from MELTS modeling suggest that nearly the full range of major element compositions observed in the CLF, BR, and DF can be reproduced by fractional crystallization of magmas with similar major element compositions and a range of water contents (0-1 wt%) crystallizing over a range of pressures (1-2.5 kbar). This range of pressures is consistent with crystallization at relatively shallow depths in the crust, suggesting that the samples examined in this thesis represent the uppermost section of the CLIP magma transport system. The maximum water contents of the CLIP parental magmas indicated by the modeling are somewhat high, but not unprecedented for LIP basalts.

Although the age range of samples from the CLIP is ~30 m.y., the magmatic episodes are geochemically consistent with a plume-related origin. Isotopic compositions in particular suggest that melting from the Galápagos plume was likely responsible for the formation of the Caribbean Plateau. Batch melting and fractional crystallization models indicate that the geochemistry of CLF, DF and BR samples is consistent with variable degrees of melting of a hybrid enriched and depleted mantle source. The larger degree of melting needed to reproduce the compositions of the majority of the CLF and BR samples (15-30%) relative to the DF samples (5-10%) is consistent with the CLF and BR being located above the plume axis, and thus derived by melting over a greater depth range than the DF, which lies along the outer edge of the plume head. The range of mantle source compositions (30-50% enriched, 50-70% depleted) needed in order to reproduce the REE patterns for the three localities suggests that the mantle source

invoked by this model is heterogeneous on a length scale of at least hundreds of kilometers. This observation is not inconsistent with the starting plume model of Campbell and Griffiths (1990), and suggests that enriched mantle plume entrains depleted upper mantle material during plume upwelling at the initiation of hotspot activity. These models are also consistent with the observation by Loewen *et al*. (2013) that there is little variation in the geochemistry of the CLIP with age. Modeling results also support the petrogenetic model of Loewen *et al*. (2013), as the advection of enriched plume material through the depleted upper mantle as a result of mantle flow associated with nearby subduction zones would also be expected to contribute to the generation of a hybrid enriched and depleted mantle source. The petrogenetic model presented in this thesis thus accounts for the spatial and temporal variation in geochemistry observed for the CLIP.

Despite the fact that this model is broadly consistent with the observed geochemical and geochronological trends in the CLIP, there are a number of refinements that could be made. Although the CLF, BR, and DF provide a transect across the CLIP, incorporating samples from additional localities (e.g. Gorgona and other northwestern South America locations) is necessary in order to further test the applicability of the model to the CLIP as a whole. Additionally, although this model provides an approximation of the end member parental magmas involved in the formation of the CLIP, it could benefit from additional constraints on composition and depth of crystallization (e.g. through the use of melt inclusions). This would potentially allow a more complete characterization of the crustal magma chambers in which the magmas of the CLIP likely crystallize. Nevertheless, the petrogenetic model presented here provides

a robust assessment of the processes responsible for generating the geochemical and geochronological trends observed in localities spanning the CLIP.

This petrogenetic model also serves as additional evidence that although some components of the classical model for LIP petrogenesis may be applicable to the majority of LIPs, several notable exceptions exist. Much like the Kerguelen and Ontong Java Plateaus, the CLIP exhibits evidence of magmatism over much larger timescales (e.g. tens of millions of years) than previously expected for LIPs. Additionally, although the geochemistry of the CLIP is consistent with a plume-related mechanism for formation, the details of its petrogenesis differs from that of other LIPs in several key respects. In particular, the apparent influence of nearby subduction zones on the melting processes that gave rise to the CLIP illustrates that, as with any earth system, mantle plumes and the processes they initiate are subject to the influence of boundary conditions. This implies that the mantle processes that give rise to LIP volcanism are more diverse than can be accommodated by the classical petrogenetic model. It remains to be seen whether or not a single, overarching model can be reasonably applied to LIPs, and additional work is needed to constrain the range of conditions that contribute to their petrogenesis. Nevertheless, it is clear that future research into LIPs must consider a broader range of mantle processes than implied by the classical paradigm.

Bibliography

Asimow, P.D. and M.S. Ghiorso. 1998. Algorithmic Modifications Extending MELTS to Calculate Subsolidus Phase Relations. *American Mineralogist, 83,* 1127-1131.

Beets, D.J., G.T. Klaver, F.F. Beunk, C. Kieft, and P. Maaskant, 1982. Picrites as parental magma of MORB type tholeiites. *Nature, 296,* 341-343.

Bercovici, D. and J. Mahoney. 1994. Double flood basalts and plume head separation at the 660-kilometer discontinuity. *Science, 266,* 1367-1367.

Borisova, A. Y., I. K. Nikogosian, J. S. Scoates, D. Weis, D. Damasceno, N. Shimizu, N., and J. L. Touret. 2002. Melt, fluid and crystal inclusions in olivine phenocrysts from Kerguelen plume-derived picritic basalts: evidence for interaction with the Kerguelen Plateau lithosphere. *Chemical Geology, 183(1),* 195-220.

Burke, K.C., C. Cooper, J.F. Dewey, P. Mann, and J.L. Pindell, 1984. Caribbean tectonics and relative plate motions, in W.E. Bonini, R.B. Hargraves, and R. Shagam, eds., The Caribbean-South American plate boundary and regional tectonics. *Geological Society of America Mem., 162,* 31-63.

Case, J.E., W.D. Macdonald, and P.J. Fox, 1990. Caribbean crustal provinces: seismic and gravity evidence. In Dengo, G., and Case, J. E., eds. The Caribbean region. (Geology of North America, Vol. H). Boulder, Colo., *Geol. Soc. Am.*, p. 15–36.

Coffin, M.F. and O. Edholm, 1994. Large igneous provinces: crustal structure, dimensions and external consequences. *Rev. Geophysics, 32,* 1-36.

Cohen, R. S., and R. K. O'Nions. 1982. The lead, neodymium and strontium isotopic structure of Ocean Ridge basalts. *Journal of Petrology, 23,* 299–324.

Dixon, J. E., D. A. Clague, and E. M. Stolper. 1991. Degassing history of water, sulfur, and carbon in submarine lavas from Kilauea Volcano, Hawaii. *The Journal of Geology,* 371-394.

Dixon, J. E., L. Leist, C. Langmuir, and J. G. Schilling. 2002. Recycled dehydrated lithosphere observed in plume-influenced mid-ocean-ridge basalt. *Nature, 420(6914),* 385-389.

Donnelly, T.W., W. Melson, R. Kay, and J.J.W. Rogers, 1973. Basalts and dolerites of late Cretaceous age from the central Caribbean. *Initial Rep. Deep Sea Drill. Proj., 15,* 989-1012.

Donnelly, K. E., S.L. Goldstein, C.H. Langmuir, and M. Spiegelman. 2004. Origin of enriched ocean ridge basalts and implications for mantle dynamics. *Earth and Planetary Science Letters, 226,* 347-366.

Duncan, R. 1978. Geochronology of basalts from the Ninetyeast Ridge and continental dispersion in the eastern Indian Ocean. *Journal of Volcanology and Geothermal Research*, *4*, 283–305.

Duncan, R.A. and R.B. Hargraves, 1984. Plate tectonic evolution of the Caribbean region in the mantle reference frame, in W.E. Bonini, R.B. Hargraves, and R. Shagam, eds., The Caribbean-South American plate boundary and regional tectonics. *Geol. Soc. America Mem*., *162*, 81-93.

Duncan, R.A. and M.A. Richards, 1991. Hotspots, mantle plumes, flood basalts, and true polar wander. *Rev. Geophysics*, *29*, 483-501.

Druken, K. A., D. R. Stegman, C. R. Kincaid, and R. W. Griffiths. 2012. Subduction disfigured mantle plumes: Plumes that are not plumes? Abstract DI43A-02 presented at 2012 Fall Meeting, AGU, San Francisco, Calif., 3–7 Dec.

Escuder Viruete, J., F. Contreras, G. Stein, P. Urien, M. Joubert, A. Pérez-Estaún, R. Friedman, and T. Ullrich, 2007. Magmatic relationships and ages between adakites, magnesian andesites and Nb-enriched basalt-andesites from Hispaniola: record of a major change in the Caribbean island arc magma sources. *Lithos*, *99*, 151-177.

Faure, G. (1986). Principles of isotope geology (Vol. 589). New York: Wiley.

Fitton, J.G., A.D. Saunders, M.J Norry, B.S. Hardarson, and R.N. Taylor, 1997. Thermal and chemical structure of the Iceland plume. *Earth and Planetary Science Letters*, *153*, 197–208.

Frey, F. A., D. Weis, A. Y. Borisova, and G. Xu. 2002. Involvement of continental crust in the formation of the Cretaceous Kerguelen Plateau: new perspectives from ODP Leg 120 sites. *Journal of Petrology*, *43(7)*, 1207-1239.

Geldmacher, J., B.B. Hanan, J. Blichert-Toft, K. Harpp, K. Hoernle, F. Hauff, R. Werner, and A.C. Kerr, 2003. Hafnium isotopic variations in volcanic rocks from the Caribbean Large Igneous Province and Galápagos hot spot tracks. *Geochemistry, Geophysics, Geosystems*, *4*(7).

Ghiorso, M. S., and R.O. Sack, 1995. Chemical mass transfer in magmatic processes IV. A revised and internally consistent thermodynamic model for the interpolation and extrapolation of liquid-solid equilibria in magmatic systems at elevated temperatures and pressures. *Contributions to Mineralogy and Petrology*, *119(2-3)*, 197-212.

Green, T. H., S.H. Sie, C.G. Ryan, and D.R. Cousens. 1989. Proton microprobe-determined partitioning of Nb, Ta, Zr, Sr and Y between garnet, clinopyroxene

and basaltic magma at high pressure and temperature. *Chemical Geology*, *74*, 201-216.

Green, T. H., J.D. Blundy, J. Adam, and G.M. Yaxley. 2000. SIMS determination of trace element partition coefficients between garnet, clinopyroxene and hydrous basaltic liquids at 2–7.5 GPa and 1080–1200 C. *Lithos*, *53*, 165-187.

Gurenko, A. A., and M. Chaussidon. 1995. Enriched and depleted primitive melts included in olivine from Icelandic tholeiites: origin by continuous melting of a single mantle column. *Geochimica et Cosmochimica Acta*, *59*, 2905-2917.

Hauff, F., K. Hoernle, G. Tilton, D.W. Graham, and A.C. Kerr. 2000a. Large volume recycling of oceanic lithosphere over short time scales: Geochemical constraints from the Caribbean Large Igneous Province. *Earth Planet. Sci. Lett.*, *174*, 247–263.

Hauff, F., K. Hoernle, P. van den Bogaard, G. Alvarado, and D. Garbe-Schönberg. 2000b. Age and geochemistry of basaltic complexes in western Costa Rica: Contributions to the geotectonic evolution of Central America. *Geochemistry, Geophysics, Geosystems*, *1(5)*.

Hart, S. R., and T. Dunn. 1993. Experimental cpx/melt partitioning of 24 trace elements. *Contributions to Mineralogy and Petrology*, *113*, 1-8.

Hastie, A.R. and A.C. Kerr, 2010. Mantle plume or slab window?: Physical and geochemical constraints on the origin of the Caribbean oceanic plateau. *Earth Sci. Rev.*, *98*, 283–293.

Herzberg, C., and P. D. Asimow. 2008. Petrology of some oceanic island basalts: PRIMELT2. XLS software for primary magma calculation. *Geochemistry, Geophysics, Geosystems*, *9(9)*.

Herzberg, C. and E. Gazel, 2009. Petrological evidence for secular cooling in mantle plumes. *Nature*, *458*, 619-622.

Hoernle, K., P. van den Bogaard, R. Werner, B. Lissinna, F. Hauff, G. Alvarado, and D. Garbe-Schönberg, 2002. Missing history (16–71 Ma) of the Galápagos hotspot: Implications for the tectonic and biological evolution of the Americas. *Geology*, *30*, 795-798.

Humphrey, C. G, 2010. In-situ U-Pb secondary ion mass spectrometry (IN-SIMS) geochronology from the Leeward Antilles islands of Aruba, Curaçao, Bonaire, and Gran Roque, MS thesis, Univ. of Georgia, Athens.

Janney, P. E., and P. R. Castillo. 1997. Geochemistry of Mesozoic Pacific mid-ocean ridge basalt: Constraints on melt generation and the evolution of the Pacific upper

mantle. *Journal of Geophysical Research: Solid Earth (1978–2012)*, *102(B3)*, 5207-5229.

Jenner, G. A., S. F. Foley, S. E. Jackson, T. H. Green, B. J. Fryer, and H. P. Longerich 1993. Determination of partition coefficients for trace elements in high pressure-temperature experimental run products by laser ablation microprobe-inductively coupled plasma-mass spectrometry (LAM-ICP-MS). *Geochimica et Cosmochimica Acta*, *57*, 5099-5103.

Johnson, K., H. J. Dick, and N. Shimizu. 1990. Melting in the oceanic upper mantle: an ion microprobe study of diopsides in abyssal peridotites. Journal of Geophysical Research: Solid Earth (1978–2012), 95(B3), 2661-2678.

Johnson, M. C., A. T. Anderson, and M. J. Rutherford. 1994. Pre-eruptive volatile contents of magmas. *Reviews in Mineralogy and Geochemistry*, *30(1)*, 281-330.

Johnson, D. M., P. R. Hooper, and R. M. Conrey. 1999. XRF analysis of rocks and minerals for major and trace elements on a single low dilution Li-tetraborate fused bead. *Advances in X-ray Analysis*, *41*, 843-867.

Kelemen, P. B., N. Shimizu, and T. Dunn. 1993. Relative depletion of niobium in some arc magmas and the continental crust: partitioning of K, Nb, La and Ce during melt/rock reaction in the upper mantle. *Earth and Planetary Science Letters*, *120*, 111-134.

Kennedy, A. K., G.E. Lofgren, and G.J. Wasserburg. 1993. An experimental study of trace element partitioning between olivine, orthopyroxene and melt in chondrules: equilibrium values and kinetic effects. *Earth and Planetary Science Letters*, *115*, 177-195.

Kent, A. J., J. A. Baker, and M. Wiedenbeck. 2002. Contamination and melt aggregation processes in continental flood basalts: constraints from melt inclusions in Oligocene basalts from Yemen. *Earth and Planetary Science Letters*, *202(3)*, 577-594.

Kerr, A. C., J. Tarney, G.F. Marriner, G.T. Klaver, A.D. Saunders, and M.F. Thirlwall, 1996. The geochemistry and petrogenesis of the late-Cretaceous picrites and basalts of the Curaçao, Netherlands, Antilles: A remnant of an oceanic plateau. *Contributions to Mineralogy and Petrology*, *124*, 29-43.

Kerr, A. C., J. Tarney, G. F. Marriner, A. Nivia, and A. D. Saunders. 1997. The Caribbean-Colombian Cretaceous igneous province: the internal anatomy of an oceanic plateau. *Large igneous provinces: Continental, oceanic, and planetary flood volcanism*, 123-144.

Kerr, A. C., J. Tarney, A. Nivia, G. F. Marriner, and A. D. Saunders. 1998. The internal structure of oceanic plateaus: Inferences from obducted Cretaceous terranes in western Colombia and the Caribbean. *Tectonophysics*, *292(3)*, 173-188.

Kerr, A. C., M. A. Iturralde-Vinent, A. D. Saunders, T. L. Babbs, and J. Tarney. 1999. A new plate tectonic model of the Caribbean: Implications from a geochemical reconnaissance of Cuban Mesozoic volcanic rocks. *Bulletin of the Geological Society of America*, *111*, 1581-1599.

Klaver, G.T., 1987. The Curaçao lava formation: An ophiolitic analogue of the anomalous thick layer 2B of the mid-Cretaceous oceanic plateaus in the western Pacific and central Caribbean. Ph.D. dissertation, University of Amsterdam, The Netherlands, 168 p.

Knaack, C., Cornelius, S. & Hooper, P. (1994) Trace element analyses of rocks and minerals by ICP-MS. http://www.wsu.edu/~geology/geolab/note/icpms.html.

Larson, R. L. (1991). Latest pulse of Earth: Evidence for a mid-Cretaceous superplume. *Geology*, *19(6)*, 547-550.

Larsen, L. M., and A. K. Pedersen. 2000. Processes in high-Mg, high-T magmas: evidence from olivine, chromite and glass in Palaeogene picrites from West Greenland. *Journal of Petrology*, *41(7)*, 1071-1098.

Le Roex, A. P. 1987. Source regions of mid-ocean ridge basalts: evidence for enrichment processes. *Mantle Metasomatism*, 389-422.

Loewen, M., R. A. Duncan, K. Krawl, and A.J.R. Kent, 2013. 30 Million Years of Plume Volcanism in the Caribbean Large Igneous Province. Manuscript in review.

Long, M. D., C. B. Till, K. A. Druken, R. W. Carlson, L. S. Wagner, M. J. Fouch, M. J., D. E. James, T. L. Grove, N. Schmerr, and C. Kincaid. 2012. Mantle dynamics beneath the Pacific Northwest and the generation of voluminous back-arc volcanism. *Geochemistry, Geophysics, Geosystems*, *13*.

Mahoney, J. J., J. D. Macdougall, G. W. Lugmair, and L. Gopalan. 1983. Kerguelen hot spot source for Rajmahal Traps and Ninetyeast Ridge? *Nature*, *303*, 385–389.

Mahoney, J. J., M. Storey, R. A. Duncan, K. J. Spencer, and M. Pringle. 1993. Geochemistry and age of the Ontong Java Plateau. *The Mesozoic Pacific: geology, tectonics, and volcanism*, 233-261.

Mamberti, M., H. Lapierre, D. Bosch, E. Jaillard, J. Hernandez, and M. Polvé. 2004. The Early Cretaceous San Juan Plutonic Suite, Ecuador: a magma chamber in an oceanic plateau?. *Canadian Journal of Earth Sciences*, *41(10)*, 1237-1258.

Mauffret, A. and Leroy, S., 1997. Seismic stratigraphy and structure of the Caribbean igneous province. *Tectonophysics*, *283*, 61–104.

Mauffret, A., S. Leroy, J.M. Vila, E. Hallot, B.M. de Lépinay, and R.A. Duncan, 2001. Prolonged magmatic and tectonic development of the Caribbean Igneous Province revealed by a diving submersible survey. *Marine Geophysical Researches*, *22*, 17-45.

Maurrasse, F., J. Husler, G. Georges, R. Schmitt, and P. Damond (1979), Upraised Caribbean sea floor below acoustic reflector B'' at the Southern Peninsula of Haiti. *Geol. Mijnbouw*, *8*, 71–83.

McKenzie, D. A. N. and R.K. O'nions. 1991. Partial melt distributions from inversion of rare earth element concentrations. *Journal of Petrology*, *32*, 1021-1091.

McDonough, W. F. and S. S. Sun, 1995. The composition of the Earth. *Chemical Geology*, *120*, 223-253.

Michard, A., P. Gurriet, M. Soudant, and F. Albarede. 1985. Nd isotopes in French Phanerozoic shales: external vs. internal aspects of crustal evolution. *Geochimica et Cosmochimica Acta*, *49(2)*, 601-610.

Miller, M. S., A. Levander, F. Niu, and A. Li. 2009. Upper mantle structure beneath the Caribbean-South American plate boundary from surface wave tomography. *Journal of Geophysical Research: Solid Earth (1978–2012)*, *114*(B1).

Morgan, W.J., 1981. Hotspot tracks and the opening of the Atlantic and Indian oceans, in *The Oceanic Lithosphere, The Sea*, ed. C. Emiliani, pp. 443-487, John Wiley and Sons, Hoboken, New Jersey.

Neal, C. R., J. J. Mahoney, and W. J. Chazey. 2002. Mantle sources and the highly variable role of continental lithosphere in basalt petrogenesis of the Kerguelen Plateau and Broken Ridge LIP: results from ODP Leg 183. *Journal of Petrology*, *43(7)*, 1177-1205.

Pindell, J.L. and S.F. Barrett, 1990. Geological Evolution of the Caribbean region: A plate tectonic perspective, in *The Geology of North Americ*a, *v. H, The Caribbean Region*, eds. G. Dengo and J.E. Case, pp. 405-432, Geological Society of America, Boulder, Colorado.

Pindell, J., L. Kennan, K.P. Stanek, W. Maresch, and G. Draper, 2006. Foundations of Gulf of Mexico and Caribbean evolution: Eight controversies resolved. *Geol. Acta*, *4*, 303–341.

Révillon, S., N. T. Arndt, E. Hallot, A. C. Kerr, and J. Tarney, 1999. Petrogenesis of picrites from the Caribbean Plateau and the North Atlantic magmatic province. *Lithos, 49*, 1-21.

Révillon, S., E. Hallot, N. T. Arndt, C. Chauvel and R. A. Duncan. 2000. A complex history for the Caribbean Plateau: petrology, geochemistry, and geochronology of the Beata Ridge, South Hispaniola. *The Journal of Geology*, *108*, 641-661.

Richards, M.A., R.A. Duncan, and V.E. Courtillot, 1989. Flood basalts and hotspot tracks: Plume heads and tails, *Science*, *246*, 103-107.

Richards, M. A., and R. W. Griffiths. 1988. Deflection of plumes by mantle shear flow: Experimental results and a simple theory. *Geophysical Journal International*, *94*, 367-376.

Shaw, D. M. 1970. Trace element fractionation during anatexis. *Geochimica et Cosmochimica Acta*, *34*, 237-243.

Sinton, C. W., R. A. Duncan, and P. Denyer. 1997. Nicoya Peninsula, Costa Rica: A single suite of Caribbean oceanic plateau magmas. *Journal of Geophysical Research: Solid Earth (1978–2012), 102(B7)*, 15507-15520.

Sinton, C.W., R.A. Duncan, M. Storey, J. Lewis, and J.J. Estrada, 1998. An oceanic flood basalt province within the Caribbean plate. *Earth and Planetary Science Letters*, *155*, 221-235.

Sen, G., R. Hickey-Vargas, D.G. Waggoner, and F. Maurrasse, 1988. Geochemistry of basalts from the Dumisseau Formation, southern Haiti: implications for the origin of the Caribbean Sea crust. *Earth and Planetary Science Letters*, *87*, 423-437.

Snow, L.J., R.A. Duncan, and T.J. Bralower, 2005. Trace element abundances in the Rock Canyon Anticline, Pueblo, Colorado, marine sedimentary section and their relationship to Caribbean plateau construction and oxygen anoxic event 2, *Paleoceanography*, *20*, 1–14.

Sparks, S. J. 1992. Magma generation in the Earth. Understanding the Earth. Cambridge University Press, Cambridge, 91-114.

Thompson, P.M.E., P.D. Kempton, R.V. White, A.C. Kerr, J. Tarney, A.D. Saunders, J.G. Fitton, and A. McBirney, 2003. Hf–Nd isotope constraints on the origin of the Cretaceous Caribbean plateau and its relationship to the Galapagos plume. *Earth and Planetary Science Letters*, *217*, 59-75.

Thompson, P.M.E., P.D. Kempton, R.V. White, A.D. Saunders, A.C. Kerr, J. Tarney, and M.S. Pringle, 2004. Elemental, Hf–Nd isotopic and geochronological constraints

on an island arc sequence associated with the Cretaceous Caribbean plateau: Bonaire, Dutch Antilles. *Lithos*, *74*, 91-116.

Walker, R.J., M.J. Storey, A.C. Kerr, J. Tarney, and N.T. Arndt, 1999. Implications of 187Os isotopic heterogeneities in a mantle plume: Evidence from Gorgona Island and Curaçao. *Geochemica et Cosmochemica Acta*, *63*, 713-728.

Wallace, P. J. 2002. Volatiles in submarine basaltic glasses from the Northern Kerguelen Plateau (ODP Site 1140): Implications for source region compositions, magmatic processes, and plateau subsidence. *Journal of Petrology, 43(7)*, 1311-1326.

Weis, D., F. A. Frey, H. Leyrit, and I. Gautier. 1993. Kerguelen Archipelago revisited: geochemical and isotopic study of the Southeast Province lavas. *Earth and Planetary Science Letters*, *118(1)*, 101-119.

White, W. M., A. W. Hofmann, and H. Puchelt. 1987. Isotope geochemistry of Pacific mid-ocean ridge basalts. *J. Geophys. Res.*, *92*, 4881–4893.

White, W. M., A. R. McBirney, and R. A. Duncan. 1993. Petrology and geochemistry of the Galápagos Islands: Portrait of a pathological mantle plume. *Journal of Geophysical Research: Solid Earth (1978–2012), 98(B11)*, 19533-19563.

White, R.V., J. Tarney, A.C. Kerr, A.D. Saunders, P.D. Kempton, M.S. Pringle, and G.T. Klaver, 1999. Modification of an oceanic plateau, Aruba, Dutch Caribbean: implications for the generation of continental crust. *Lithos*, *46*, 43-68.

Wiedmann, J., 1978. Ammonites from the Curaçao Lava Formation, Curaçao, Caribbean, *Geol. Mijnbouw*, *57*, 361–364.

Wood, D.A., 1979. A variably veined suboceanic upper mantle—genetic significance for mid-ocean ridge basalts from geochemical evidence. Geology, *7*, 499-503.

Wright, J. E. and S. J. Wyld, 2011. Late Cretaceous subduction initiation on the eastern margin of the Caribbean-Colombian Oceanic Plateau: One great arc of the Caribbean (?), *Geosphere*, *7* 468–493

APPENDIX

Table 8.1. Major and trace element composition of olivine standard (Fo83) analyzed using EMPA prior to analysis of DF samples.

Element	1	2	3	4	Average	σ
Si	18.294	18.481	18.164	18.159	18.274	0.151
Al	0.008	0.007	0.005	0.009	0.007	0.002
K	0.008	0.006	0.000	0.000	0.003	0.004
Mn	0.249	0.229	0.216	0.271	0.241	0.024
Fe	13.004	12.806	12.906	13.160	12.969	0.151
Ni	0.021	0.000	0.021	0.000	0.010	0.012
Na	0.001	0.005	0.004	0.005	0.004	0.002
Mg	26.295	26.220	26.195	26.236	26.237	0.043
Ca	0.005	0.010	0.001	0.009	0.006	0.004
Cr	0.010	0.016	0.006	0.018	0.013	0.005
Ti	0.000	0.006	0.012	0.000	0.004	0.006
O	41.970	42.072	41.722	41.829	41.898	0.154
Total	99.865	99.857	99.251	99.695	99.667	0.288

Table 8.2. Major and trace element composition of clinopyroxene standard (KAUG) analyzed using EMPA prior to analysis of CLF samples. Columns 1 through 6 are analyses of separate spots.

Element	1	2	3	4	5	6	Average	σ
Si	18.332	18.242	18.269	18.383	18.306	18.201	18.289	0.065
Al	0.001	-0.002	-0.001	0.010	-0.003	0.017	0.004	0.008
K	-0.057	0.009	0.010	0.006	-0.016	-0.016	-0.011	0.026
Mn	0.212	0.219	0.220	0.208	0.216	0.248	0.220	0.014
Fe	13.193	12.840	12.894	13.006	12.799	12.736	12.911	0.166
Ni	0.034	-0.038	-0.010	0.007	0.041	-0.048	-0.002	0.037
Na	-0.003	-0.003	-0.010	0.000	0.008	-0.006	-0.002	0.006
Mg	26.384	26.425	26.253	26.336	26.376	26.366	26.357	0.058
Ca	0.008	0.005	0.004	0.003	0.000	-0.002	0.003	0.003
Ti	0.008	0.005	0.000	0.010	-0.005	-0.007	0.002	0.007
Cr	0.029	0.010	0.025	0.010	0.002	0.005	0.013	0.011
O	42.116	41.920	41.864	42.093	41.956	41.809	41.960	0.123
Total	100.315	99.674	99.539	100.072	99.704	99.382	99.781	0.348

Table 8.3. Major and trace element composition of olivine standard (Fo83) analyzed using EMPA prior to analysis of DF samples. Columns 1 through 5 are analyses of separate spots.

Element	1	2	3	4	5	Average	σ
Si	23.663	23.386	23.648	23.472	23.753	23.584	0.151
Al	4.601	4.644	4.621	4.609	4.639	4.623	0.019
K	0.012	0.004	-0.015	0.014	-0.001	0.003	0.012
Fe	5.394	5.598	5.416	5.400	5.531	5.468	0.092
Na	0.936	0.961	0.973	0.975	0.998	0.969	0.022
Mg	10.037	10.105	9.979	10.074	10.178	10.075	0.074
Ti	0.480	0.451	0.447	0.445	0.461	0.457	0.014
Ca	10.588	10.424	10.547	10.516	10.539	10.523	0.061
Ni	0.023	-0.068	0.016	0.082	-0.057	-0.001	0.062
Mn	0.049	0.177	0.112	0.141	0.098	0.115	0.048
Cr	0.131	0.098	0.120	0.095	0.102	0.109	0.016
O	44.163	43.908	44.112	43.967	44.397	44.109	0.191
Total	100.078	99.755	99.990	99.789	100.695	100.061	0.379

Table 8.4. Major and trace element compositions of olivine phenocrysts in DF samples expressed as wt% oxides. Fo = percent forsterite, Fa = percent fayalite.

Point	HA-76-28-ol1-1	HA-76-28-ol1-2	HA-76-28-ol1-3	HA-77-244-ol1-1	HA-77-244-ol1-2	HA-77-244-ol1-3	HA-77-244-ol1-4	HA-77-244-ol1-5	HA-77-244-ol1-6
Position	core	core	rim	rim	core	rim	core	core	rim
Fo	71.7	71.4	71.2	72.7	72.9	72.5	72.5	72.7	72.5
Fa	28.3	28.6	28.8	27.3	27.1	27.5	27.5	27.3	27.5
SiO_2	37.29	37.08	37.06	37.32	37.51	37.25	37.03	37.44	37.09
Al_2O_3	0.03	0.02	0.02	0.05	0.03	0.04	0.02	0.03	0.02
K_2O	0.01	b.d.l.	b.d.l.	0.01	0.02	b.d.l.	b.d.l.	0.01	b.d.l.
MnO	0.33	0.36	0.34	0.30	0.33	0.34	0.31	0.36	0.32
FeO	25.51	25.88	25.88	24.67	24.52	24.90	24.86	24.63	24.83
NiO	0.12	0.17	0.18	0.15	0.19	0.12	0.16	0.13	0.18
Na_2O	b.d.l.	0.01	b.d.l.	0.01	b.d.l.	0.01	0.01	0.02	0.01
MgO	36.20	36.26	35.97	36.87	36.95	36.90	36.75	36.77	36.80
CaO	0.28	0.28	0.27	0.27	0.28	0.29	0.28	0.28	0.27
TiO_2	0.03	0.02	0.04	0.01	0.02	0.02	0.03	0.03	0.02
Cr_2O_3	b.d.l.	0.01	0.02	0.01	0.01	0.01	0.03	b.d.l.	0.02
Total	99.81	100.09	99.78	99.66	99.84	99.88	99.48	99.71	99.57

Table 8.4 (Continued)

Point	HA-77-244-ol2-1	HA-77-244-ol2-2	HA-77-244-ol2-3	HA-77-244-ol2-4	HA-77-244-ol3-1	HA-77-244-ol3-2	HA-77-244-ol3-3	HA-77-244-ol4-1	HA-77-244-ol4-2
Position	rim	core	core	rim	rim	core	core	rim	rim
Fo	72.9	76.1	75.9	74.4	70.8	73.9	74.6	71.6	70.4
Fa	27.1	23.9	24.1	25.6	29.2	26.1	25.4	28.4	29.6
SiO_2	37.38	37.89	37.85	37.81	37.11	37.41	37.90	36.88	36.81
Al_2O_3	0.04	0.03	0.02	0.03	0.01	0.04	0.02	0.03	0.03
K_2O	b.d.l.	b.d.l.	0.01	0.00	0.01	0.01	0.01	b.d.l.	0.02
MnO	0.33	0.25	0.29	0.28	0.36	0.37	0.32	0.35	0.35
FeO	24.38	21.98	22.06	23.06	26.33	23.68	22.83	25.55	26.42
NiO	0.17	0.14	0.19	0.17	0.19	0.22	0.17	0.10	0.15
Na_2O	b.d.l.	0.01	b.d.l.	b.d.l.	b.d.l.	b.d.l.	0.07	0.01	0.08
MgO	36.77	39.25	39.01	37.69	35.73	37.52	37.70	36.08	35.16
CaO	0.26	0.27	0.28	0.28	0.28	0.28	0.29	0.29	0.32
TiO_2	0.02	0.02	0.03	0.02	0.02	0.03	0.02	0.02	0.02
Cr_2O_3	0.01	0.02	0.02	0.02	0.02	0.01	0.02	0.01	0.02
Total	99.36	99.87	99.74	99.37	100.06	99.57	99.35	99.30	99.38

Table 8.4 (Continued)

Point	HA-77-244-ol4-3	HA-77-244-ol4-1	HA-77-244-ol4-2	HA-77-244-ol4-3	HA-77-244-ol4-4	HA-77-244-ol5-1	HA-77-244-ol5-2	HA-77-244-ol5-3	HA-77-244-ol5-4
Position	core	rim	core	core	core	rim	core	core	core
Fo	72.0	71.8	72.0	72.3	72.1	72.0	71.7	71.5	71.9
Fa	28.0	28.2	28.0	27.7	27.9	28.0	28.3	28.5	28.1
SiO_2	37.12	37.30	36.95	37.12	36.96	37.15	37.51	37.26	36.83
Al_2O_3	0.03	0.03	0.03	0.04	0.02	0.02	0.02	0.03	0.03
K_2O	b.d.l.	b.d.l.	0.01	b.d.l.	0.01	b.d.l.	b.d.l.	b.d.l.	b.d.l.
MnO	0.36	0.33	0.34	0.36	0.32	0.36	0.33	0.36	0.37
FeO	24.87	25.42	25.00	24.84	25.11	25.27	25.37	25.80	25.31
NiO	0.14	0.14	0.14	0.16	0.17	0.12	0.19	0.16	0.13
Na_2O	b.d.l.	b.d.l.	b.d.l.	b.d.l.	b.d.l.	b.d.l.	0.02	0.02	0.01
MgO	35.93	36.25	36.06	36.35	36.32	36.45	36.07	36.37	36.26
CaO	0.27	0.29	0.29	0.30	0.28	0.30	0.28	0.28	0.28
TiO_2	0.02	0.03	0.03	0.02	0.01	0.02	0.04	0.03	0.02
Cr_2O_3	0.01	0.01	0.01	0.03	0.02	0.02	0.01	b.d.l.	b.d.l.
Total	98.75	99.79	98.86	99.20	99.21	99.72	99.84	100.31	99.25

Table 8.4 (Continued)

Point	HA-77-244-ol5-5	HA-77-244-ol5-6	HA-77-29-ol1-1	HA-77-29-ol1-2	HA-77-29-ol2-1	HA-77-29-ol2-2	HA-77-29-ol2-3	HA-77-29-ol3-1	HA-77-29-ol3-2
Position	rim	rim	core	rim	rim	core	core	rim	core
Fo	70.2	70.8	70.4	69.9	70.1	70.4	70.1	70.0	70.3
Fa	29.8	29.2	29.6	30.1	29.9	29.6	29.9	30.0	29.7
SiO_2	36.86	37.20	37.02	36.98	36.84	36.82	36.37	36.60	36.30
Al_2O_3	0.03	0.03	0.02	0.02	0.03	0.03	0.03	0.04	0.03
K_2O	0.01	b.d.l.	b.d.l.	b.d.l.	b.d.l.	b.d.l.	b.d.l.	b.d.l.	b.d.l.
MnO	0.33	0.30	0.31	0.32	0.32	0.36	0.35	0.35	0.35
FeO	26.77	26.24	26.42	26.88	26.87	26.44	26.84	26.97	26.49
NiO	0.13	0.12	0.18	0.17	0.17	0.18	0.11	0.14	0.18
Na_2O	b.d.l.	0.01	0.01	b.d.l.	0.02	0.01	0.01	0.01	0.02
MgO	35.32	35.63	35.19	35.04	35.26	35.28	35.23	35.34	35.18
CaO	0.29	0.29	0.28	0.27	0.28	0.27	0.27	0.27	0.27
TiO_2	0.03	0.04	0.03	0.02	0.01	0.02	0.02	0.02	0.03
Cr_2O_3	0.01	b.d.l.	b.d.l.	0.01	0.01	b.d.l.	0.01	b.d.l.	0.01
Total	99.78	99.85	99.47	99.73	99.82	99.40	99.24	99.74	98.87

Table 8.4 (Continued)

Point	HA-77-29-ol3-3	HA-77-29-ol4-1	HA-77-29-ol4-2	HA-77-29-ol4-3	HA-77-29-ol4-4	HA-77-29-ol4-5	HA-77-29-ol4-6	HA-77-29-ol4-7
Position	core	core	core	core	core	core	core	rim
Fo	70.2	70.5	69.8	70.5	70.6	70.7	70.1	67.3
Fa	29.8	29.5	30.2	29.5	29.4	29.3	29.9	32.7
SiO_2	36.98	36.73	37.34	36.84	36.94	36.74	36.77	36.19
Al_2O_3	0.03	0.02	0.03	0.03	0.03	0.02	0.02	0.00
K_2O	b.d.l.	b.d.l.	0.01	b.d.l.	0.01	b.d.l.	0.01	0.01
MnO	0.34	0.29	0.37	0.34	0.31	0.37	0.36	0.35
FeO	26.56	26.42	27.02	26.34	26.18	26.34	26.69	29.00
NiO	0.21	0.13	0.13	0.15	0.16	0.20	0.16	0.15
Na_2O	0.01	0.01	b.d.l.	0.01	b.d.l.	0.02	0.01	b.d.l.
MgO	35.17	35.39	34.98	35.29	35.24	35.61	35.16	33.56
CaO	0.27	0.28	0.27	0.28	0.27	0.28	0.28	0.29
TiO_2	0.03	0.02	0.04	0.02	0.03	0.04	0.02	0.03
Cr_2O_3	0.02	0.01	0.01	0.01	0.01	0.02	0.03	0.01
Total	99.62	99.31	100.19	99.32	99.18	99.64	99.52	99.58

Table 8.5. Major and trace element compositions of clinopyroxene phenocrysts and glomerocrysts in DF samples expressed as wt% oxides. En = percent enstatite, Fs = percent ferrosilate, Wo = percent wollastonite, p = phenocryst. g = crystal in glomerocryst.

Point	HA-76-28-px1-1	HA-76-28-px1-2	HA-76-28-px2-1	HA-76-28-px3-1	HA-76-28-px3-2	HA-76-28-px4-1	HA-76-28-px4-2	HA-76-28-px5-1	HA-76-28-px6-1
Type	p	p	p	g	g	g	g	g	g
Position	core	core	rim	core	core	rim	core	core	core
En	48.7	46.9	40.0	47.8	48.1	48.4	49.1	47.7	47.2
Fs	14.9	16.5	26.9	16.8	14.4	14.4	17.2	16.5	15.8
Wo	36.4	36.6	33.1	35.4	37.5	37.3	33.7	35.8	37.0
SiO_2	52.20	51.68	49.87	52.71	52.60	52.42	51.75	51.76	51.58
Al_2O_3	2.55	2.56	2.71	1.66	2.69	2.71	2.83	2.86	2.59
K_2O	b.d.l.	0.02	b.d.l.	0.01	b.d.l.	0.01	0.01	0.01	b.d.l.
FeO	8.96	9.88	16.10	10.13	8.65	8.56	10.26	9.81	9.42
Na_2O	0.22	0.25	0.29	0.21	0.23	0.24	0.26	0.25	0.22
MgO	16.78	16.16	13.64	16.49	16.50	16.51	16.78	16.26	16.14
TiO_2	0.76	1.01	1.74	0.82	0.83	0.84	0.96	0.99	0.96
CaO	17.42	17.52	15.74	16.99	17.89	17.71	16.05	16.99	17.58
NiO	0.01	0.02	0.06	0.06	0.02	0.04	0.04	0.07	0.04
MnO	0.18	0.22	0.28	0.21	0.16	0.18	0.22	0.19	0.20
Cr_2O_3	0.32	0.33	0.02	0.18	0.52	0.52	0.39	0.41	0.43
Total	99.41	99.66	100.45	99.46	100.08	99.73	99.55	99.60	99.16

Table 8.5 (Continued)

Point	HA-76-28-px7-1	HA-76-28-px7-2	HA-76-28-px7-3	HA-76-28-px7-4	HA-76-28-px8-1	HA-76-28-px8-2	HA-76-28-px8-3	HA-76-28-px9-1	HA-76-28-px9-2
Type	g	g	g	g	g	g	g	p	p
Position	rim	core	core	rim	rim	core	rim	core	core
En	49.0	48.9	49.3	48.4	48.7	49.1	34.9	48.2	47.1
Fs	14.9	15.4	17.0	16.5	15.6	16.4	31.3	17.7	20.9
Wo	36.0	35.8	33.8	35.1	35.8	34.5	33.9	34.0	32.0
SiO_2	51.84	52.87	52.47	52.67	51.41	52.48	52.43	51.93	51.16
Al_2O_3	2.71	2.62	2.22	2.57	2.54	1.94	2.29	2.62	2.74
K_2O	0.02	b.d.l.	0.01	b.d.l.	b.d.l.	0.02	b.d.l.	b.d.l.	b.d.l.
FeO	8.87	9.19	10.22	9.93	9.34	9.96	9.35	10.63	12.63
Na_2O	0.27	0.26	0.22	0.25	0.25	0.25	0.23	0.26	0.26
MgO	16.75	16.73	16.97	16.64	16.72	17.04	16.97	16.59	16.27
TiO_2	0.79	0.79	0.75	0.85	0.77	0.75	0.81	0.94	1.22
CaO	17.13	17.03	16.19	16.78	17.10	16.66	16.72	16.28	15.42
NiO	0.03	0.04	0.04	0.02	0.04	0.03	0.02	0.00	0.08
MnO	0.21	0.18	0.19	0.21	0.21	0.19	0.21	0.25	0.25
Cr_2O_3	0.39	0.37	0.35	0.37	0.35	0.31	0.38	0.34	0.19
Total	98.99	100.08	99.61	100.28	98.75	99.63	99.42	99.83	100.22

Table 8.5 (Continued)

Point	HA-76-28-px9-3	HA-76-28-px9-4	HA-76-28-px9-5	HA-76-28-px9-6	HA-77-244-px1-1	HA-77-244-px1-2	HA-77-244-px2-1	HA-77-244-px2-2	HA-77-244-px2-3
Type	p	p	p	p	p	p	p	p	p
Position	core	core	rim	core	core	core	core	core	core
En	48.0	48.8	48.3	47.6	47.3	47.4	47.6	48.1	46.7
Fs	17.3	15.6	17.2	16.2	17.2	20.5	17.7	17.2	16.3
Wo	34.7	35.6	34.5	36.2	35.6	32.1	34.7	34.6	36.9
SiO_2	52.61	51.72	52.14	51.47	52.60	51.46	52.47	51.57	51.50
Al_2O_3	2.45	2.59	2.49	2.70	2.12	2.80	1.58	2.66	2.75
K_2O	b.d.l.	b.d.l.	b.d.l.	0.02	0.01	b.d.l.	b.d.l.	b.d.l.	0.02
FeO	10.40	9.34	10.37	9.70	10.39	12.29	10.82	10.38	9.82
Na_2O	0.26	0.27	0.23	0.26	0.23	0.24	0.23	0.23	0.29
MgO	16.52	16.70	16.69	16.31	16.43	16.32	16.67	16.55	16.07
TiO_2	0.86	0.85	0.85	1.00	0.90	1.21	0.85	1.03	1.07
CaO	16.65	16.99	16.61	17.24	17.19	15.37	16.90	16.58	17.67
NiO	0.05	0.04	b.d.l.	0.05	0.03	b.d.l.	b.d.l.	0.03	0.02
MnO	0.21	0.18	0.21	0.17	0.23	0.28	0.23	0.18	0.18
Cr_2O_3	0.29	0.37	0.29	0.42	0.28	0.19	0.15	0.31	0.46
Total	100.32	99.04	99.90	99.34	100.42	100.16	99.90	99.52	99.83

Table 8.5 (Continued)

Point	HA-77-244-px2-4	HA-77-29-px1-1	HA-77-29-px1-2	HA-77-29-px1-3	HA-77-29-px2-1	HA-77-29-px2-2	HA-77-29-px2-3	HA-77-29-px3-1	HA-77-29-px4-1
Type	p	g	g	g	g	g	g	g	g
Position	core	rim	core	rim	rim	rim	core	core	core
En	48.4	48.4	46.9	47.5	45.7	47.7	47.1	47.3	47.5
Fs	16.1	16.6	18.0	18.4	18.4	18.1	17.3	18.0	17.3
Wo	35.5	35.0	35.0	34.2	35.9	34.2	35.6	34.7	35.2
SiO_2	52.15	51.39	51.10	51.49	51.58	52.01	51.50	51.98	51.64
Al_2O_3	2.39	2.85	2.62	2.56	2.00	2.55	2.52	2.46	2.47
K_2O	b.d.l.	0.01	b.d.l.	b.d.l.	b.d.l.	b.d.l.	b.d.l.	b.d.l.	0.01
FeO	9.70	9.85	10.90	11.08	11.04	10.95	10.37	10.85	10.34
Na_2O	0.28	0.25	0.29	0.26	0.23	0.25	0.26	0.26	0.24
MgO	16.61	16.42	16.21	16.37	15.66	16.46	16.13	16.29	16.22
TiO_2	0.78	1.01	1.05	0.96	1.10	0.98	1.00	1.00	0.95
CaO	16.97	16.50	16.84	16.40	17.10	16.45	17.00	16.64	16.75
NiO	0.03	0.04	0.05	0.04	0.01	0.01	0.02	b.d.l.	0.02
MnO	0.18	0.20	0.20	0.23	0.20	0.17	0.19	0.24	0.22
Cr_2O_3	0.24	0.45	0.38	0.34	0.19	0.33	0.33	0.37	0.33
Total	99.34	98.96	99.63	99.73	99.13	100.15	99.30	100.09	99.19

Table 8.5 (Continued)

Point	HA-77-29-px5-1	HA-77-29-px5-2	HA-77-29-px5-3	HA-77-29-px6-1	HA-77-29-px6-2	HA-77-29-px6-3	HA-77-29-px7-1	HA-77-29-px7-2	HA-77-29-px8-1
Type	g	g	g	g	g	g	g	g	g
Position	core	core	rim	rim	rim	core	rim	core	core
En	46.8	47.2	47.5	47.1	47.0	47.1	45.9	49.2	47.3
Fs	17.5	18.0	18.0	17.6	17.5	17.6	18.5	15.2	17.5
Wo	35.6	34.8	34.5	35.4	35.4	35.3	35.6	35.5	35.1
SiO_2	52.13	50.91	51.11	51.91	51.26	51.45	51.12	52.35	51.43
Al_2O_3	2.11	2.71	3.02	2.53	2.63	2.66	2.68	2.61	2.62
K_2O	0.01	b.d.l.	0.01	b.d.l.	0.01	b.d.l.	b.d.l.	0.01	b.d.l.
FeO	10.61	10.81	10.72	10.47	10.58	10.55	11.16	9.13	10.57
Na_2O	0.25	0.26	0.27	0.24	0.24	0.26	0.24	0.26	0.27
MgO	16.18	16.20	16.13	16.08	16.24	16.17	15.79	16.90	16.30
TiO_2	1.00	1.14	0.95	1.04	1.03	1.08	1.27	0.83	1.00
CaO	17.12	16.64	16.33	16.81	17.03	16.88	17.07	16.98	16.83
NiO	0.02	0.01	0.02	0.09	0.04	0.05	0.04	0.02	0.01
MnO	0.19	0.20	0.17	0.23	0.22	0.23	0.22	0.19	0.19
Cr_2O_3	0.31	0.45	0.45	0.39	0.37	0.41	0.38	0.43	0.37
Total	99.93	99.33	99.16	99.79	99.66	99.76	99.98	99.72	99.58

Table 8.5 (Continued)

Point	HA-77-29-px8-2	HA-77-29-px8-3	HA-77-29-px9-1	HA-77-29-px9-2	HA-77-29-px10-1	HA-77-29-px10-2	HA-77-29-px11-1	HA-77-29-px11-2	HA-77-109-px1-1
Type	g	g	g	g	g	g	g	g	g
Position	core	rim	rim	core	rim	core	rim	core	core
En	49.3	47.7	45.1	48.0	47.1	48.1	48.6	45.4	49.5
Fs	15.1	18.6	18.8	16.9	18.1	17.3	15.9	18.8	11.2
Wo	35.7	33.7	36.0	35.1	34.7	34.6	35.4	35.8	39.3
SiO_2	52.14	51.94	51.17	51.73	51.69	52.01	52.47	50.64	52.42
Al_2O_3	2.57	1.73	2.21	2.64	3.01	2.41	2.70	2.40	2.85
K_2O	0.02	0.01	b.d.l.	0.01	b.d.l.	b.d.l.	b.d.l.	0.01	b.d.l.
FeO	9.11	11.31	11.38	10.17	10.86	10.39	9.59	11.28	6.68
Na_2O	0.30	0.23	0.23	0.27	0.28	0.26	0.26	0.24	0.21
MgO	17.02	16.61	15.51	16.52	16.14	16.53	16.68	15.58	16.82
TiO_2	0.80	0.89	1.16	1.02	1.13	0.91	0.87	1.26	0.61
CaO	17.17	16.35	17.25	16.81	16.55	16.52	16.91	17.12	18.57
NiO	b.d.l.	0.02	0.02	b.d.l.	0.07	0.04	0.05	0.02	0.06
MnO	0.17	0.23	0.18	0.21	0.20	0.22	0.16	0.21	0.11
Cr_2O_3	0.48	0.26	0.23	0.37	0.41	0.33	0.47	0.24	1.00
Total	99.77	99.58	99.35	99.73	100.33	99.62	100.17	98.98	99.32

Table 8.5 (Continued)

Point	HA-77-109-px2-1	HA-77-109-px2-2	HA-77-109-px3-1	HA-77-109-px3-2	HA-77-109-px4-1	HA-77-109-px4-2	HA-77-109-px5-1	HA-77-109-px5-2	HA-77-109-px6-1
Type	g	g	g	g	g	g	g	g	g
Position	core	rim	core	core	rim	core	rim	core	core
En	49.6	49.7	48.9	49.3	49.6	49.7	49.4	49.1	49.8
Fs	11.4	11.3	11.7	11.5	11.2	11.4	11.4	12.1	11.0
Wo	39.1	39.0	39.4	39.3	39.1	38.8	39.1	38.8	39.2
SiO_2	52.92	53.33	52.13	52.87	52.18	52.79	51.48	51.40	52.74
Al_2O_3	2.72	2.47	3.41	2.91	2.82	2.75	3.00	3.41	2.65
K_2O	0.01	0.01	b.d.l.	0.01	0.01	b.d.l.	0.02	b.d.l.	b.d.l.
FeO	6.81	6.79	6.93	6.88	6.74	6.83	6.75	7.11	6.51
Na_2O	0.22	0.24	0.25	0.23	0.21	0.23	0.25	0.22	0.22
MgO	16.98	17.07	16.51	16.83	16.90	17.04	16.73	16.50	16.91
TiO_2	0.61	0.59	0.83	0.66	0.63	0.60	0.68	0.80	0.59
CaO	18.62	18.67	18.52	18.67	18.56	18.51	18.43	18.15	18.51
NiO	0.05	0.05	0.01	0.06	0.04	0.02	0.04	0.00	0.03
MnO	0.13	0.12	0.13	0.11	0.08	0.14	0.15	0.12	0.13
Cr_2O_3	0.97	0.89	1.04	0.95	0.94	0.97	1.01	1.23	0.92
Total	100.04	100.22	99.76	100.18	99.12	99.89	98.54	98.95	99.21

Table 8.5 (Continued)

Point	HA-77-109-px6-2	HA-77-109-px7-1	HA-77-109-px7-2
Type	g	g	g
Position	rim	rim	core
En	49.4	49.3	49.2
Fs	12.5	11.6	11.1
Wo	38.1	39.2	39.8
SiO_2	52.25	52.16	51.81
Al_2O_3	2.80	3.07	2.88
K_2O	b.d.l.	0.02	0.02
FeO	7.46	6.92	6.57
Na_2O	0.23	0.22	0.24
MgO	16.84	16.75	16.64
TiO_2	0.71	0.69	0.64
CaO	18.11	18.52	18.72
NiO	0.03	0.02	b.d.l.
MnO	0.14	0.09	0.10
Cr_2O_3	0.78	1.06	1.07
Total	99.36	99.52	98.69

Table 8.6. Major and trace element compositions of olivine phenocrysts in CLF samples expressed as wt% oxides. Fo = percent forsterite, Fa = percent fayalite.

Point	CAO-15a-ol1-1	CAO-15a-ol2-1	CAO-15a-ol2-2	CAO-15a-ol3-1	CAO-15a-ol4-1	CAO-15a-ol4-2	CAO-15a-ol5-1	CAO-15a-ol5-2	CAO-15a-ol6-1
Position	core	rim	core	core	core	rim	rim	core	core
Fo	82.6	87.6	84.0	88.3	86.5	83.8	82.9	88.0	87.5
Fa	17.4	12.4	16.0	11.7	13.5	16.2	17.1	12.0	12.5
SiO_2	38.81	39.48	39.27	39.58	39.93	39.22	39.22	40.19	39.85
Al_2O_3	0.03	0.08	0.05	0.08	0.07	0.05	0.06	0.06	0.07
K_2O	0.01	0.04	0.02	0.02	b.d.l.	b.d.l.	0.05	0.02	0.03
MnO	0.20	0.19	0.21	0.20	0.17	0.19	0.22	0.15	0.15
FeO	16.25	11.75	14.95	11.16	12.85	15.29	16.00	11.49	11.95
NiO	0.35	0.30	0.34	0.33	0.34	0.27	0.37	0.38	0.37
Na_2O	0.02	0.02	b.d.l.	0.03	b.d.l.	b.d.l.	b.d.l.	0.01	0.02
MgO	43.39	46.54	44.18	47.12	46.23	44.23	43.53	47.26	46.76
CaO	0.28	0.28	0.28	0.22	0.28	0.26	0.26	0.28	0.29
TiO_2	b.d.l.	b.d.l.	0.01	b.d.l.	b.d.l.	b.d.l.	0.01	b.d.l.	b.d.l.
Cr_2O_3	0.04	0.10	0.08	0.10	0.06	0.03	0.04	0.07	0.05
Total	99.38	98.79	99.39	98.83	99.93	99.54	99.75	99.92	99.51

Table 8.6 (Continued)

Point	CAO-15a-ol7-1	CAO-15a-ol7-2	CAO-15a-ol8-1	CAO-15a-ol8-2	CAO-15a-ol9-1	CAO-15a-ol9-2	CAO-15a-ol10-1	CAO-15a-ol10-2	CAO-15a-ol11-1
Position	rim	core	rim	core	rim	core	rim	core	rim
Fo	89.0	89.2	82.9	88.6	81.3	85.5	86.2	88.1	84.6
Fa	11.0	10.8	17.1	11.4	18.7	14.5	13.8	11.9	15.4
SiO_2	40.15	39.68	38.98	40.26	39.10	39.84	40.08	40.26	39.47
Al_2O_3	0.03	0.04	0.06	0.06	0.05	0.06	0.06	0.03	0.06
K_2O	b.d.l.	b.d.l.	b.d.l.	b.d.l.	0.02	b.d.l.	b.d.l.	0.02	0.02
MnO	0.14	0.16	0.21	0.18	0.27	0.21	0.16	0.21	0.20
FeO	10.57	10.30	15.96	10.91	17.43	13.69	13.14	11.42	14.60
NiO	0.35	0.42	0.29	0.34	0.33	0.26	0.36	0.35	0.33
Na_2O	0.01	0.01	0.02	0.01	b.d.l.	0.02	b.d.l.	b.d.l.	0.01
MgO	47.85	47.81	43.35	47.62	42.40	45.43	46.12	47.34	44.89
CaO	0.31	0.30	0.25	0.30	0.21	0.29	0.29	0.30	0.29
TiO_2	b.d.l.	0.01	0.00	0.01	0.04	0.02	0.01	0.01	0.01
Cr_2O_3	0.06	0.08	0.07	0.07	0.04	0.05	0.05	0.06	0.05
Total	99.46	98.81	99.19	99.76	99.89	99.88	100.25	100.02	99.92

Table 8.6 (Continued)

Point	CAO-15a-ol11-2	CAO-15a-ol12-1	CAO-15a-ol12-2	CAO-15a-ol13-1	CAO-15a-ol13-2	CAO-15a-ol14-1	CAO-15a-ol14-2	CAO-15d-ol1-1	CAO-15d-ol1-2
Position	core	rim	core	rim	core	rim	core	rim	core
Fo	87.8	84.9	88.3	84.2	87.7	84.7	87.2	88.6	88.7
Fa	12.2	15.1	11.7	15.8	12.3	15.3	12.8	11.4	11.3
SiO_2	39.98	39.47	40.24	39.49	40.10	39.62	41.03	40.14	40.22
Al_2O_3	0.07	0.05	0.05	0.07	0.05	0.09	0.06	0.07	0.06
K_2O	0.01	0.02	0.01	0.02	b.d.l.	b.d.l.	0.03	0.02	0.01
MnO	0.17	0.18	0.18	0.22	0.17	0.20	0.21	0.19	0.16
FeO	11.69	14.23	11.09	14.79	11.64	14.40	11.84	10.94	10.87
NiO	0.33	0.33	0.36	0.26	0.34	0.31	0.31	0.33	0.33
Na_2O	b.d.l.	b.d.l.	0.02	0.02	0.01	0.01	0.03	0.02	0.01
MgO	47.09	44.99	47.17	44.15	46.70	44.75	45.37	47.51	47.79
CaO	0.29	0.25	0.30	0.27	0.29	0.29	0.72	0.30	0.31
TiO_2	0.01	0.01	b.d.l.	0.01	b.d.l.	0.01	b.d.l.	b.d.l.	0.01
Cr_2O_3	0.06	0.08	0.09	0.05	0.08	0.07	0.07	0.09	0.08
Total	99.70	99.60	99.52	99.36	99.38	99.74	99.67	99.61	99.86

Table 8.6 (Continued)

Point	CAO-15d-ol2-1	CAO-15d-ol3-1	CAO-15d-ol3-2	CAO-15d-ol3-3	CAO-15d-ol4-1	CAO-15d-ol5-1	CAO-15d-ol6-1	CAO-15d-ol7-1	CAO-15d-ol8-1
Position	core	core	rim	core	core	core	core	core	core
Fo	87.9	88.8	87.5	88.9	87.8	87.9	88.0	88.1	88.0
Fa	12.1	11.2	12.5	11.1	12.2	12.1	12.0	11.9	12.0
SiO_2	39.94	39.94	39.79	40.20	40.34	39.94	40.40	40.01	39.92
Al_2O_3	0.09	0.10	0.05	0.07	0.06	0.08	0.07	0.11	0.11
K_2O	0.01	b.d.l.	0.03	0.01	b.d.l.	0.01	b.d.l.	b.d.l.	0.01
MnO	0.17	0.16	0.12	0.13	0.18	0.16	0.13	0.16	0.16
FeO	11.56	10.70	11.96	10.62	11.66	11.58	11.52	11.32	11.39
NiO	0.32	0.41	0.30	0.38	0.34	0.32	0.32	0.34	0.31
Na_2O	0.01	0.04	0.01	0.01	0.01	0.02	0.02	0.01	b.d.l.
MgO	47.23	47.75	46.76	47.75	47.03	47.05	47.29	47.13	46.90
CaO	0.31	0.29	0.31	0.30	0.29	0.32	0.30	0.30	0.30
TiO_2	0.01	b.d.l.	0.02	b.d.l.	b.d.l.	0.01	0.01	0.02	0.01
Cr_2O_3	0.09	0.10	0.09	0.10	0.09	0.07	0.11	0.09	0.10
Total	99.75	99.50	99.42	99.56	99.99	99.57	100.16	99.48	99.22

Table 8.6 (Continued)

Point	CAO-15d-ol9-1	CAO-15d-ol10-1	CAO-15d-ol11-1	CAO-15d-ol12-1	CAO-15d-ol13-1	CAO-15d-ol14-1	CAO-15d-ol15-1	CAO-15d-ol16-1	CAO-15d-ol17-1
Position	core	core	rim	core	rim	core	core	rim	rim
Fo	88.2	88.0	87.9	87.8	88.0	87.9	87.9	88.0	87.9
Fa	11.8	12.0	12.1	12.2	12.0	12.1	12.1	12.0	12.1
SiO_2	40.30	40.02	40.03	40.02	39.80	39.95	39.43	40.16	39.69
Al_2O_3	0.06	0.08	0.08	0.10	0.10	0.06	0.08	0.10	0.06
K_2O	0.01	b.d.l.	0.01	b.d.l.	0.03	0.01	0.01	0.03	0.02
MnO	0.17	0.14	0.13	0.17	0.15	0.16	0.16	0.15	0.14
FeO	11.27	11.45	11.57	11.67	11.57	11.48	11.47	11.32	11.53
NiO	0.32	0.28	0.37	0.32	0.41	0.39	0.33	0.32	0.32
Na_2O	0.02	b.d.l.	0.01	0.02	0.01	0.02	b.d.l.	0.05	b.d.l.
MgO	47.22	47.20	47.21	47.17	47.51	46.93	46.85	46.64	46.90
CaO	0.27	0.30	0.30	0.30	0.31	0.31	0.30	0.30	0.31
TiO_2	b.d.l.	0.01	0.01	0.01	0.01	b.d.l.	b.d.l.	0.01	b.d.l.
Cr_2O_3	0.08	0.07	0.07	0.06	0.10	0.08	0.08	0.09	0.08
Total	99.70	99.55	99.79	99.83	99.98	99.38	98.73	99.18	99.04

Table 8.6 (Continued)

Point	CAO-15d-ol18-1	CAO-15d-ol19-1	CAO-15d-ol20-1	CAO-15d-ol20-2	CAO-15d-ol21-1	CAO-15d-ol21-2	CAO-15d-ol22-1	CAO-15d-ol23-1	CAO-15d-ol23-2
Position	core	core	core	core	core	core	core	core	core
Fo	87.9	87.0	88.0	88.0	88.3	88.2	88.0	88.0	88.0
Fa	12.1	13.0	12.0	12.0	11.7	11.8	12.0	12.0	12.0
SiO_2	40.05	39.56	39.95	39.58	40.17	40.08	40.17	40.22	40.22
Al_2O_3	0.09	0.07	0.08	0.08	0.06	0.09	0.09	0.07	0.08
K_2O	0.01	0.02	0.01	0.01	0.01	0.01	b.d.l.	b.d.l.	0.01
MnO	0.14	0.17	0.18	0.17	0.18	0.19	0.20	0.16	0.15
FeO	11.39	12.22	11.48	11.47	11.28	11.27	11.47	11.42	11.44
NiO	0.33	0.28	0.38	0.32	0.41	0.37	0.34	0.39	0.34
Na_2O	0.03	0.02	0.02	0.02	b.d.l.	0.01	0.02	b.d.l.	b.d.l.
MgO	46.56	45.93	47.27	47.18	47.54	47.41	47.18	47.10	46.97
CaO	0.31	0.33	0.28	0.30	0.29	0.29	0.29	0.29	0.30
TiO_2	0.01	0.01	0.02	b.d.l.	0.01	0.01	0.01	b.d.l.	0.01
Cr_2O_3	0.06	0.04	0.09	0.08	0.13	0.11	0.09	0.07	0.08
Total	98.97	98.65	99.77	99.22	100.08	99.84	99.87	99.72	99.61

Table 8.6 (Continued)

Point	CAO-15d-ol24-1	CAO-15d-ol25-1	CAO-15d-ol26-1	CAO-15d-ol26-2	CAO-15d-ol27-1	CAO-15d-ol28-1	CAO-15d-ol28-2	CAO-15d-ol29-1	CAO-15d-ol30-1
Position	core	core	rim	core	core	core	core	core	rim
Fo	88.3	87.9	87.9	88.1	88.1	88.0	88.0	87.8	87.9
Fa	11.7	12.1	12.1	11.9	11.9	12.0	12.0	12.2	12.1
SiO_2	40.13	40.17	39.75	39.93	40.27	40.35	40.34	40.47	40.33
Al_2O_3	0.05	0.08	0.06	0.06	0.08	0.07	0.10	0.08	0.07
K_2O	0.01	0.02	b.d.l.	0.01	0.02	0.03	0.01	0.02	0.03
MnO	0.14	0.17	0.16	0.13	0.18	0.16	0.18	0.18	0.14
FeO	11.19	11.52	11.55	11.40	11.38	11.50	11.52	11.69	11.59
NiO	0.38	0.33	0.30	0.36	0.33	0.37	0.33	0.36	0.34
Na_2O	0.03	0.02	b.d.l.	b.d.l.	b.d.l.	b.d.l.	0.03	0.02	0.01
MgO	47.51	47.13	47.16	47.17	47.23	47.13	47.31	47.16	47.18
CaO	0.30	0.29	0.30	0.30	0.29	0.31	0.30	0.30	0.31
TiO_2	0.01	b.d.l.	b.d.l.	0.01	0.01	0.01	b.d.l.	0.01	b.d.l.
Cr_2O_3	0.12	0.08	0.09	0.05	0.08	0.10	0.09	0.08	0.08
Total	99.87	99.80	99.37	99.42	99.87	100.02	100.21	100.35	100.09

Table 8.6 (Continued)

Point	CAO-15d-ol30-2	CAO-15d-ol31-1	CAO-15d-ol31-2
Position	core	core	core
Fo	88.0	87.8	87.7
Fa	12.0	12.2	12.3
SiO_2	40.17	40.39	40.35
Al_2O_3	0.08	0.06	0.08
K_2O	0.02	b.d.l.	0.02
MnO	0.14	0.17	0.16
FeO	11.53	11.72	11.73
NiO	0.34	0.32	0.41
Na_2O	0.02	0.01	b.d.l.
MgO	47.34	47.29	47.09
CaO	0.29	0.29	0.30
TiO_2	0.01	b.d.l.	0.02
Cr_2O_3	0.06	0.07	0.09
Total	100.01	100.32	100.24

Table 8.7. Major and trace element compositions of plagioclase phenocrysts in CLF samples expressed as wt% oxides. An = percent anorthite, Ab = percent albite.

Point	CAO-18-plag1-1	CAO-18-plag2-1	CAO-18-plag3-1	CAO-18-plag4-1	CAO-18-plag5-1	CAO-18-plag5-2	CAO-18-plag6-1	CAO-18-plag7-1	CAO-18-plag7-2
Position	core	rim	core	rim	rim	rim	rim	rim	rim
An	69.4	63.6	59.7	60.3	74.6	69.7	73.1	72.0	62.8
Ab	30.6	36.4	40.3	39.7	25.4	30.3	26.9	28.0	37.2
Na_2O	3.41	4.01	4.39	4.36	2.83	3.40	2.94	3.06	4.02
MgO	0.20	0.12	0.12	0.13	0.28	0.22	0.25	0.23	0.25
SiO_2	51.13	52.73	53.48	52.81	50.02	51.18	49.46	49.96	52.72
Al_2O_3	30.12	29.62	28.81	29.04	31.04	30.54	31.01	30.79	28.84
FeO	0.87	0.94	0.87	0.95	0.70	0.85	0.71	0.72	1.13
CaO	13.98	12.66	11.78	11.98	15.06	14.15	14.45	14.27	12.26
K_2O	0.02	0.04	0.04	0.02	0.02	0.02	0.03	0.03	0.06
TiO_2	0.05	0.05	0.06	0.06	0.03	0.05	0.04	0.03	0.06
Total	99.78	100.17	99.53	99.33	99.97	100.41	98.88	99.09	99.34

Table 8.7 (Continued)

Point	CAO-18-plag8-1	CAO-18-plag9-1	CAO-18-plag9-2	CAO-18-plag10-1	CAO-18-plag11-1	CAO-18-plag12-1	CAO-18-plag13-1	CAO-18-plag14-1	CAO-18-plag15-1
Position	rim	rim	rim	rim	rim	rim	core	core	core
An	73.9	63.3	67.9	75.5	73.2	59.5	71.9	72.8	66.0
Ab	26.1	36.7	32.1	24.5	26.8	40.5	28.1	27.2	34.0
Na_2O	2.90	3.94	3.52	2.66	2.93	4.49	3.09	3.02	3.75
MgO	0.18	0.13	0.19	0.26	0.25	0.11	0.27	0.27	0.17
SiO_2	49.78	51.96	50.65	48.66	49.17	53.85	51.06	50.42	52.40
Al_2O_3	31.27	28.67	29.47	31.37	31.31	28.51	30.80	31.26	30.04
FeO	0.89	0.96	0.90	0.66	0.71	0.96	0.66	0.76	0.80
CaO	14.84	12.31	13.48	14.89	14.50	11.94	14.30	14.58	13.20
K_2O	0.04	0.05	0.02	0.02	0.02	0.05	0.02	0.03	0.03
TiO_2	0.04	0.05	0.04	0.05	0.04	0.06	0.04	0.04	0.06
Total	99.94	98.07	98.26	98.58	98.93	99.98	100.25	100.39	100.46

Table 8.7 (Continued)

Point	CAO-18-plag15-2	CAO-18-plag16-1	CAO-18-plag16-2	CAO-18-plag17-1	CAO-18-plag18-1	CAO-18-plag19-1	CAO-18-plag19-2	CAO-18-plag20-1	CAO-13-plag1-1
Position	core	rim	core	rim	core	core	rim	rim	rim
An	62.4	74.9	73.5	72.1	74.8	76.0	73.1	68.4	67.0
Ab	37.6	25.1	26.5	27.9	25.2	24.0	26.9	31.6	33.0
Na_2O	4.11	2.75	2.84	2.95	2.81	2.63	2.93	3.57	3.63
MgO	0.13	0.27	0.29	0.72	0.26	0.26	0.23	0.21	0.10
SiO_2	53.30	49.97	50.44	49.32	49.76	49.32	49.97	51.23	51.77
Al_2O_3	28.92	31.06	30.99	30.26	31.25	31.54	30.84	29.99	30.61
FeO	0.84	0.75	0.59	2.13	0.70	0.70	0.69	0.90	0.69
CaO	12.33	14.91	14.31	13.80	15.15	15.06	14.41	14.01	13.30
K_2O	0.04	0.02	0.03	0.03	0.06	0.04	0.16	0.03	0.09
TiO_2	0.05	0.03	0.04	0.04	0.04	0.03	0.03	0.04	0.05
Total	99.71	99.76	99.53	99.26	100.02	99.58	99.26	99.97	100.23

Table 8.7 (Continued)

Point	CAO-13-plag2-1	CAO-13-plag2-2	CAO-13-plag3-1	CAO-13-plag3-2	CAO-13-plag4-1	CAO-13-plag5-1	CAO-13-plag5-2	CAO-13-plag6-1	CAO-13-plag6-2
Position	core	core	core	rim	rim	core	core	rim	rim
An	85.2	81.1	84.4	65.8	66.4	86.9	81.8	63.1	83.4
Ab	14.8	18.9	15.6	34.2	33.6	13.1	18.2	36.9	16.6
Na_2O	1.65	2.11	1.73	3.77	3.67	1.46	2.00	4.04	1.86
MgO	0.06	0.07	0.06	0.11	0.11	0.06	0.08	0.08	0.05
SiO_2	46.91	47.77	46.72	51.70	51.77	46.49	47.48	52.67	47.25
Al_2O_3	33.94	33.00	33.82	30.46	30.12	34.20	33.66	29.82	33.49
FeO	0.58	0.63	0.64	0.82	0.70	0.60	0.66	0.70	0.76
CaO	17.18	16.34	16.97	13.09	13.13	17.42	16.28	12.50	16.94
K_2O	0.02	0.04	0.05	0.09	0.09	0.02	0.02	0.15	0.03
TiO_2	0.02	0.03	0.02	0.07	0.07	0.02	0.03	0.08	0.04
Total	100.35	99.98	100.00	100.10	99.66	100.27	100.21	100.03	100.42

Table 8.7 (Continued)

Point	CAO-13-plag7-1	CAO-13-plag7-2	CAO-13-plag8-1	CAO-13-plag8-2	CAO-13-plag9-1	CAO-13-plag9-2	CAO-13-plag10-1	CAO-13-plag10-2	CAO-13-plag11-1
Position	rim	core	core	core	rim	core	core	core	core
An	87.3	77.6	85.4	68.8	67.7	76.0	67.1	83.8	70.0
Ab	12.7	22.4	14.6	31.2	32.3	24.0	32.9	16.2	30.0
Na_2O	1.40	2.44	1.65	3.48	3.54	2.68	3.61	1.81	3.30
MgO	0.04	0.08	0.07	0.10	0.10	0.07	0.09	0.06	0.07
SiO_2	45.86	48.79	46.70	51.23	51.48	48.78	51.45	46.89	50.92
Al_2O_3	34.00	32.77	33.69	30.54	30.46	32.58	30.81	33.29	31.33
FeO	0.70	0.67	0.73	0.70	0.92	0.63	0.79	0.83	0.67
CaO	17.42	15.32	17.47	13.89	13.46	15.36	13.35	16.98	13.89
K_2O	0.05	0.04	0.02	0.09	0.10	0.06	0.10	0.03	0.09
TiO_2	0.02	0.02	0.04	0.06	0.04	0.04	0.07	0.03	0.07
Total	99.50	100.13	100.37	100.09	100.10	100.21	100.27	99.93	100.34

Table 8.7 (Continued)

Point	CAO-13-plag12-1	CAO-10-plag1-1	CAO-10-plag1-2	CAO-10-plag2-1	CAO-10-plag3-1	CAO-35d-plag1-1	CAO-35d-plag2-1	CAO-35d-plag3-1	CAO-35d-plag4-1
Position	rim	rim	core	core	rim	rim	core	core	core
An	74.6	62.4	70.4	67.2	63.7	78.6	78.7	78.5	82.7
Ab	25.4	37.6	29.6	32.8	36.3	21.4	21.3	21.5	17.3
Na_2O	2.80	4.11	3.25	3.61	3.97	2.37	2.34	2.34	1.92
MgO	0.07	0.16	0.29	0.25	0.21	0.17	0.16	0.17	0.14
SiO_2	49.19	53.13	51.35	52.05	52.96	49.01	48.42	48.87	47.61
Al_2O_3	31.97	28.66	30.01	29.70	28.87	32.25	32.94	32.29	33.17
FeO	0.74	1.14	0.89	1.07	1.01	0.82	0.73	0.78	0.77
CaO	14.87	12.33	13.99	13.35	12.61	15.73	15.68	15.53	16.61
K_2O	0.07	0.06	0.02	0.04	0.05	0.04	0.03	0.03	0.02
TiO_2	0.06	0.08	0.04	0.08	0.07	0.03	0.03	0.03	0.02
Total	99.76	99.66	99.82	100.13	99.76	100.43	100.34	100.05	100.26

Table 8.7 (Continued)

Point	CAO-35d-plag5-1	CAO-35d-plag6-1	CAO-35d-plag7-1	CAO-35d-plag8-1	CAO-35d-plag8-2	CAO-35d-plag9-1	CAO-35d-plag10-1	CAO-35d-plag11-1	CAO-35d-plag12-1
Position	core	rim	core	core	core	core	core	core	rim
An	75.0	76.9	76.9	79.1	79.4	72.6	79.7	68.4	80.2
Ab	25.0	23.1	23.1	20.9	20.6	27.4	20.3	31.6	19.8
Na_2O	2.76	2.51	2.51	2.30	2.26	3.04	2.25	3.50	2.18
MgO	0.26	0.31	0.20	0.17	0.16	0.19	0.17	0.20	0.16
SiO_2	49.70	48.93	49.48	48.35	48.07	50.37	48.54	51.56	48.50
Al_2O_3	31.67	31.62	31.54	32.55	32.55	31.27	32.62	30.45	32.24
FeO	0.87	1.61	0.93	0.78	0.84	0.79	0.81	0.80	0.76
CaO	15.03	15.12	15.11	15.77	15.81	14.59	16.00	13.69	16.04
K_2O	0.05	0.04	0.03	0.02	0.03	0.05	0.03	0.04	0.03
TiO_2	0.02	0.09	0.04	0.03	0.02	0.04	0.02	0.07	0.03
Total	100.35	100.23	99.83	99.96	99.74	100.33	100.44	100.32	99.94

Table 8.7 (Continued)

Point	CAO-35d-plag13-1	CAO-35d-plag14-1	CAO-35d-plag15-1	CAO-35d-plag16-1
Position	core	core	rim	core
An	78.9	75.3	78.0	78.9
Ab	21.1	24.7	22.0	21.1
Na_2O	2.28	2.69	2.43	2.34
MgO	0.36	0.25	0.17	0.17
SiO_2	48.57	49.95	49.23	48.34
Al_2O_3	32.10	31.26	32.12	32.59
FeO	1.06	1.04	0.80	0.77
CaO	15.43	14.86	15.54	15.78
K_2O	0.03	0.05	0.02	0.04
TiO_2	0.03	0.04	0.03	0.03
Total	99.86	100.14	100.35	100.05

Table 8.8. Major and trace element compositions of clinopyroxene phenocrysts and glomerocrysts in CLF samples expressed as wt% oxides. En = percent enstatite, Fs = percent ferrosilate, Wo = percent wollastonite.

Point	CAO-15a-px1-1	CAO-15a-px1-2	CAO-15a-px2-1	CAO-15a-px2-2	CAO-15a-px3-1	CAO-15d-px1-1	CAO-15d-px2-1	CAO-15d-px3-1	CAO-15d-px4-1
Position	core	core	core	rim	core	core	core	core	core
En	54.2	51.0	52.1	54.0	51.4	43.8	39.8	42.0	41.4
Fs	8.5	9.0	9.8	8.5	8.5	13.3	15.4	13.9	13.0
Wo	37.3	40.0	38.0	37.5	40.0	42.8	44.8	44.0	45.6
SiO_2	53.36	51.65	53.02	53.09	52.41	48.13	46.63	47.59	47.53
Al_2O_3	2.60	4.35	3.05	2.65	3.89	9.03	10.64	9.56	9.99
K_2O	0.01	0.02	0.01	0.01	0.01	0.04	0.01	0.02	0.02
FeO	5.20	5.25	5.99	5.09	5.12	7.47	8.43	7.73	7.33
Na_2O	0.14	0.15	0.20	0.14	0.15	0.23	0.22	0.16	0.24
MgO	18.92	17.41	18.24	18.97	17.59	14.14	12.56	13.36	13.18
TiO_2	0.24	0.39	0.40	0.28	0.35	1.27	1.31	1.28	1.00
CaO	18.12	18.96	18.51	18.33	19.05	19.21	19.65	19.47	20.23
NiO	b.d.l.	b.d.l.	0.06	0.15	0.07	0.08	b.d.l.	b.d.l.	0.01
MnO	0.09	0.22	0.13	0.25	0.08	0.20	0.20	0.17	0.07
Cr_2O_3	0.66	0.86	0.76	0.58	0.89	0.65	0.17	0.32	0.11
Total	99.36	99.27	100.38	99.53	99.61	100.44	99.82	99.65	99.71

Table 8.8 (Continued)

Point	CAO-15d-px5-1	CAO-15d-px6-1	CAO-15d-px7-1	CAO-15d-px8-1	CAO-15d-px9-1	CAO-15d-px10-1	CAO-15d-px11-1	CAO-15d-px12-1	CAO-15d-px12-2
Position	core	core	core	core	core	rim	rim	core	core
En	42.1	40.7	41.7	39.4	43.6	41.3	43.0	45.3	43.0
Fs	13.1	14.9	13.2	14.5	12.6	14.0	13.9	12.4	14.6
Wo	44.8	44.4	45.1	46.1	43.8	44.7	43.1	42.3	42.5
SiO_2	48.06	46.98	47.39	47.07	47.88	47.45	47.89	48.51	47.35
Al_2O_3	9.79	10.51	10.38	11.11	9.22	9.75	9.77	8.11	9.71
K_2O	0.02	0.01	0.03	0.02	0.02	0.01	0.04	0.04	0.03
FeO	7.39	8.29	7.35	8.01	7.12	7.74	7.91	7.05	8.09
Na_2O	0.23	0.24	0.21	0.26	0.22	0.25	0.22	0.33	0.24
MgO	13.46	12.89	13.22	12.40	14.06	13.19	13.79	14.63	13.65
TiO_2	1.05	1.20	1.14	1.03	1.08	1.19	1.25	0.97	1.00
CaO	19.96	19.55	19.90	20.21	19.65	19.86	19.25	18.99	18.76
NiO	0.07	b.d.l.	0.08	0.03	b.d.l.	0.03	0.05	0.07	0.09
MnO	0.09	0.10	0.13	0.14	0.13	0.23	0.07	0.09	0.16
Cr_2O_3	0.14	0.15	0.12	0.11	0.15	0.24	0.10	0.31	0.08
Total	100.26	99.91	99.93	100.38	99.53	99.94	100.34	99.10	99.16

Table 8.8 (Continued)

Point	CAO-15d-px13-1	CAO-15d-px14-1	CAO-15d-px15-1	CAO-15d-px16-1	CAO-22-px1-1	CAO-22-px1-2	CAO-22-px1-3	CAO-22-px2-1	CAO-22-px2-2
Position	core	core	rim	rim	rim	core	core	rim	core
En	46.2	40.6	39.5	40.2	45.1	49.8	48.9	45.7	49.2
Fs	11.8	13.4	15.0	16.1	14.3	7.8	8.7	13.3	8.4
Wo	41.9	45.9	45.5	43.7	40.6	42.3	42.4	41.0	42.4
SiO_2	49.08	46.96	46.81	46.54	51.63	53.67	53.42	51.23	53.31
Al_2O_3	7.87	10.56	10.80	9.80	3.12	1.90	2.34	3.25	2.18
K_2O	0.01	b.d.l.	0.02	0.05	0.03	0.01	0.01	0.01	b.d.l.
FeO	6.69	7.37	8.20	8.84	8.77	4.75	5.35	8.13	5.09
Na_2O	0.21	0.27	0.22	0.34	0.19	0.17	0.19	0.17	0.19
MgO	14.98	12.78	12.32	12.59	15.78	17.50	17.21	15.99	17.14
TiO_2	1.02	1.03	1.12	1.30	0.44	0.20	0.26	0.45	0.23
CaO	18.92	20.11	19.75	19.04	19.76	20.70	20.78	19.97	20.55
NiO	b.d.l.	b.d.l.	0.17	b.d.l.	b.d.l.	b.d.l.	0.04	0.00	0.01
MnO	0.15	0.16	0.13	0.11	0.17	0.16	0.15	0.14	0.12
Cr_2O_3	0.41	0.14	0.11	0.35	0.01	0.54	0.48	0.03	0.38
Total	99.36	99.39	99.65	98.96	99.88	99.59	100.23	99.38	99.21

Table 8.8 (Continued)

Point	CAO-22-px3-1	CAO-22-px3-2	CAO-22-px3-3	CAO-22-px3-4	CAO-22-px3-5	CAO-22-px4-1	CAO-22-px4-2	CAO-22-px5-1	CAO-22-px5-2
Position	rim	rim	core	core	core	rim	core	rim	core
En	42.3	47.7	45.4	40.9	48.4	48.2	45.5	41.8	48.1
Fs	15.6	9.6	14.0	15.8	9.4	9.3	13.1	16.8	9.2
Wo	42.1	42.8	40.6	43.3	42.2	42.5	41.4	41.5	42.6
SiO_2	50.06	52.15	51.32	48.82	52.47	52.94	51.46	49.60	53.22
Al_2O_3	5.20	3.15	3.34	6.70	2.49	2.66	3.67	4.94	2.64
K_2O	0.01	0.02	b.d.l.	0.01	b.d.l.	0.01	0.01	0.02	0.02
FeO	9.29	5.79	8.51	9.22	5.78	5.69	7.97	9.98	5.66
Na_2O	0.23	0.18	0.19	0.26	0.20	0.16	0.20	0.25	0.18
MgO	14.41	16.45	15.85	13.69	17.07	16.93	15.89	14.27	16.83
TiO_2	0.72	0.34	0.41	0.73	0.28	0.28	0.44	0.77	0.29
CaO	19.91	20.53	19.74	20.18	20.71	20.75	20.14	19.71	20.75
NiO	0.04	0.04	b.d.l.	b.d.l.	0.05	0.02	b.d.l.	b.d.l.	0.06
MnO	0.17	0.09	0.19	0.20	0.12	0.12	0.17	0.23	0.09
Cr_2O_3	b.d.l.	0.48	b.d.l.	0.02	0.41	0.44	0.03	b.d.l.	0.46
Total	100.04	99.21	99.54	99.84	99.57	100.00	99.99	99.76	100.20

Table 8.8 (Continued)

Point	CAO-22-px6-1	CAO-22-px7-1	CAO-22-px7-2	CAO-32-px1-1	CAO-32-px1-2	CAO-32-px2-1	CAO-32-px3-1	CAO-32-px4-1	CAO-32-px4-2
Position	rim	rim	core	rim	core	core	core	core	core
En	46.7	44.2	48.6	37.9	52.0	54.3	51.5	37.6	42.2
Fs	12.9	15.5	9.1	34.7	16.3	16.1	20.4	30.5	27.2
Wo	40.4	40.3	42.3	27.4	31.7	29.6	28.1	31.9	30.6
SiO_2	52.65	50.44	53.32	51.11	51.80	52.36	52.14	50.03	49.93
Al_2O_3	2.85	4.05	2.37	2.07	3.55	3.47	2.50	1.98	2.66
K_2O	0.01	b.d.l.	0.01	0.01	b.d.l.	0.01	0.03	b.d.l.	b.d.l.
FeO	7.86	9.35	5.66	20.23	9.98	9.96	12.46	18.35	16.55
Na_2O	0.20	0.19	0.16	0.18	0.19	0.16	0.16	0.23	0.22
MgO	16.31	15.29	17.07	12.72	18.31	19.09	18.02	12.94	14.64
TiO_2	0.36	0.55	0.25	0.53	0.43	0.51	0.47	0.67	0.74
CaO	19.67	19.40	20.67	12.80	15.50	14.47	13.69	15.31	14.80
NiO	0.09	b.d.l.	0.08	0.02	0.03	0.04	b.d.l.	b.d.l.	b.d.l.
MnO	0.17	0.20	0.06	0.51	0.25	0.16	0.27	0.35	0.28
Cr_2O_3	0.09	b.d.l.	0.26	b.d.l.	0.12	0.25	0.03	b.d.l.	0.01
Total	100.28	99.46	99.90	100.17	100.15	100.47	99.77	99.86	99.83

Table 8.8 (Continued)

Point	CAO-32-px5-1	CAO-32-px5-2	CAO-32-px5-3	CAO-32-px6-1	CAO-18-px1-1	CAO-18-px2-1	CAO-18-px2-2	CAO-18-px3-1	CAO-18-px3-2
Position	rim	core	core	core	core	rim	core	core	rim
En	36.3	48.2	48.3	50.4	49.4	43.6	52.7	50.6	50.4
Fs	33.2	19.3	17.3	14.4	18.0	28.1	19.7	14.0	14.1
Wo	30.6	32.5	34.4	35.2	32.6	28.3	27.7	35.4	35.5
SiO_2	50.41	51.60	50.83	51.79	51.35	50.95	53.13	52.07	51.61
Al_2O_3	1.71	2.86	3.32	3.84	2.44	1.84	1.49	2.85	2.95
K_2O	b.d.l.	b.d.l.	0.01	b.d.l.	0.01	0.02	0.01	0.01	b.d.l.
FeO	19.85	11.72	10.41	8.67	10.94	17.20	12.20	8.38	8.52
Na_2O	0.18	0.17	0.18	0.19	0.18	0.18	0.17	0.23	0.18
MgO	12.44	16.79	16.60	17.29	17.15	15.31	18.76	17.42	17.46
TiO_2	0.61	0.51	0.54	0.56	0.42	0.54	0.30	0.38	0.42
CaO	14.61	15.73	16.48	16.82	15.73	13.81	13.71	16.94	17.08
NiO	b.d.l.	b.d.l.	0.02	0.03	0.08	0.05	b.d.l.	0.03	b.d.l.
MnO	0.43	0.26	0.21	0.17	0.19	0.36	0.31	0.24	0.18
Cr_2O_3	b.d.l.	0.02	0.06	0.19	0.02	0.00	0.01	0.13	0.17
Total	100.22	99.65	98.65	99.54	98.53	100.28	100.08	98.66	98.56

Table 8.8 (Continued)

Point	CAO-18-px4-1	CAO-18-px5-1	CAO-18-px5-2	CAO-18-px5-3	CAO-18-px5-4	CAO-18-px6-1	CAO-18-px6-2	CAO-13-px1-1	CAO-13-px1-2
Position	core	core	core	core	core	rim	core	core	rim
En	51.0	52.4	52.7	53.6	53.7	41.6	57.9	44.9	48.8
Fs	13.1	11.5	11.1	13.9	12.3	27.2	16.1	18.9	14.6
Wo	35.9	36.2	36.2	32.5	34.0	31.1	26.0	36.2	36.6
SiO_2	52.84	53.16	53.02	52.22	53.74	51.11	54.13	51.31	52.77
Al_2O_3	2.73	2.10	2.03	3.14	1.86	1.98	1.43	1.65	2.11
K_2O	0.02	0.01	0.02	0.01	b.d.l.	b.d.l.	0.01	b.d.l.	b.d.l.
FeO	8.01	7.04	6.76	8.56	7.55	16.37	10.24	11.51	8.84
Na_2O	0.21	0.19	0.17	0.17	0.14	0.23	0.12	0.23	0.16
MgO	17.93	18.40	18.39	18.86	19.17	14.33	20.95	15.63	16.96
TiO_2	0.39	0.25	0.24	0.38	0.26	0.59	0.22	0.68	0.30
CaO	17.57	17.69	17.59	15.92	16.87	14.91	13.12	17.56	17.73
NiO	0.04	0.06	0.07	b.d.l.	b.d.l.	0.01	b.d.l.	b.d.l.	b.d.l.
MnO	0.18	0.14	0.17	0.13	0.28	0.33	0.16	0.19	0.21
Cr_2O_3	0.16	0.36	0.37	0.36	0.31	0.01	0.06	0.07	0.26
Total	100.06	99.39	98.83	99.74	100.17	99.86	100.45	98.84	99.33

Table 8.8 (Continued)

Point	CAO-13-px1-3	CAO-13-px1-4	CAO-13-px2-1	CAO-13-px2-2	CAO-13-px2-3	CAO-13-px3-1	CAO-13-px3-2	CAO-13-px4-1	CAO-13-px5-1
Position	core	core	core	core	core	rim	core	rim	rim
En	47.5	45.2	51.2	44.0	45.1	45.9	45.5	45.7	45.1
Fs	16.6	19.2	12.1	19.3	19.5	19.3	19.4	19.1	19.2
Wo	36.0	35.5	36.7	36.6	35.4	34.8	35.1	35.2	35.7
SiO_2	52.03	51.27	52.55	51.55	51.33	51.73	51.75	51.96	50.99
Al_2O_3	2.13	1.89	2.12	2.05	1.91	1.87	1.97	1.92	1.79
K_2O	b.d.l.	b.d.l.	b.d.l.	0.01	b.d.l.	b.d.l.	b.d.l.	0.01	b.d.l.
FeO	10.15	11.67	7.45	11.57	11.82	11.82	11.90	11.70	11.76
Na_2O	0.20	0.24	0.18	0.32	0.27	0.23	0.28	0.25	0.30
MgO	16.60	15.69	17.99	15.05	15.66	16.10	15.98	16.00	15.77
TiO_2	0.32	0.76	0.27	0.63	0.80	0.79	0.81	0.84	0.66
CaO	17.50	17.15	17.92	17.43	17.14	17.00	17.12	17.16	17.40
NiO	0.05	b.d.l.	b.d.l.	0.08	0.05	0.08	0.07	0.07	b.d.l.
MnO	0.18	0.23	0.14	0.19	0.25	0.25	0.24	0.23	0.22
Cr_2O_3	0.34	0.14	0.31	0.52	0.18	0.07	0.06	0.08	0.20
Total	99.50	99.05	98.94	99.42	99.41	99.94	100.17	100.23	99.10

Table 8.8 (Continued)

Point	CAO-13-px5-2	CAO-13-px6-1	CAO-13-px6-2	CAO-13-px7-1	CAO-10-px1-1	CAO-10-px1-2	CAO-10-px1-3	CAO-10-px2-1	CAO-10-px3-1
Position	core	rim	core	rim	core	core	core	core	core
En	44.2	44.3	44.7	45.1	55.5	52.9	53.9	52.0	56.1
Fs	19.6	20.4	19.1	19.2	11.3	9.7	10.0	12.8	11.3
Wo	36.2	35.3	36.3	35.7	33.2	37.4	36.1	35.2	32.6
SiO_2	51.74	51.12	51.91	51.39	53.64	53.47	54.20	52.66	54.11
Al_2O_3	1.93	2.13	1.79	1.89	1.77	2.13	1.81	3.36	1.50
K_2O	b.d.l.	b.d.l.	b.d.l.	b.d.l.	b.d.l.	b.d.l.	b.d.l.	b.d.l.	0.03
FeO	11.99	12.43	11.69	11.62	6.94	5.97	6.10	7.79	7.01
Na_2O	0.31	0.23	0.25	0.26	0.14	0.20	0.11	0.16	0.13
MgO	15.49	15.40	15.68	15.57	19.72	18.52	19.02	18.23	20.04
TiO_2	0.74	0.72	0.72	0.75	0.21	0.22	0.23	0.41	0.22
CaO	17.66	17.10	17.69	17.15	16.42	18.21	17.71	17.16	16.17
NiO	0.06	0.09	b.d.l.	b.d.l.	0.13	b.d.l.	0.11	0.08	b.d.l.
MnO	0.27	0.21	0.22	0.19	0.18	0.11	0.19	0.17	0.18
Cr_2O_3	0.15	0.11	0.11	0.09	0.48	0.85	0.49	0.43	0.33
Total	100.33	99.56	100.06	98.91	99.63	99.68	100.00	100.43	99.73

Table 8.8 (Continued)

Point	CAO-10-px4-1	CAO-10-px4-2	CAO-10-px5-1	CAO-10-px6-1	CAO-10-px6-2	CAO-10-px7-1	CAO-10-px8-1	CAO-10-px9-1	CAO-10-px10-1
Position	rim	core	core	core	core	rim	core	core	core
En	51.8	52.5	53.0	52.5	54.1	54.9	52.2	53.3	54.5
Fs	10.4	9.6	10.0	10.2	10.4	12.8	10.7	17.8	13.0
Wo	37.8	37.9	37.0	37.3	35.5	32.3	37.2	28.9	32.6
SiO_2	52.25	53.07	53.58	52.99	54.03	52.95	53.67	52.43	53.58
Al_2O_3	2.76	2.27	2.18	2.62	1.75	3.11	2.21	2.91	1.52
K_2O	0.02	b.d.l.	0.01	0.02	0.01	b.d.l.	0.01	b.d.l.	0.01
FeO	6.30	5.83	6.12	6.27	6.39	7.79	6.60	11.05	8.10
Na_2O	0.21	0.17	0.15	0.15	0.16	0.13	0.17	0.14	0.12
MgO	18.05	18.37	18.48	18.27	19.14	19.27	18.46	18.77	19.58
TiO_2	0.28	0.24	0.22	0.26	0.22	0.37	0.23	0.48	0.27
CaO	18.33	18.43	17.93	18.09	17.46	15.80	18.29	14.16	16.28
NiO	0.11	b.d.l.	b.d.l.	b.d.l.	b.d.l.	0.01	0.05	0.03	0.02
MnO	0.15	0.16	0.11	0.05	0.17	0.20	0.13	0.15	0.21
Cr_2O_3	0.59	0.60	0.56	0.65	0.46	0.31	0.41	0.03	0.12
Total	99.05	99.15	99.34	99.38	99.78	99.93	100.25	100.16	99.82

Table 8.8 (Continued)

Point	CAO-10-px10-2	CAO-35d-px1-1	CAO-35d-px2-1	CAO-35d-px3-1
Position	core	rim	core	core
En	51.6	49.5	48.7	50.0
Fs	11.5	16.5	16.7	16.4
Wo	37.0	34.0	34.6	33.6
SiO_2	52.04	52.70	52.32	52.81
Al_2O_3	3.76	1.96	2.02	1.76
K_2O	b.d.l.	b.d.l.	b.d.l.	0.01
FeO	6.82	10.20	10.31	10.09
Na_2O	0.19	0.17	0.16	0.21
MgO	17.75	17.55	17.26	17.72
TiO_2	0.37	0.35	0.37	0.34
CaO	17.71	16.74	17.08	16.60
NiO	0.03	0.14	b.d.l.	0.02
MnO	0.22	0.22	0.27	0.28
Cr_2O_3	0.63	0.16	0.13	0.10
Total	99.52	100.20	99.92	99.94